DEVELOPMENT OF ZrB_2-SiC-Si_3N_4/Ta CERAMIC COMPOSITES FOR HIGH TEMPERATURE APPLICATIONS

A dissertation work

Submitted in partial fulfilment of the requirements for the award of the degree of

DOCTOR OF PHILOSOPHY

in

METALLURGICAL AND MATERIALS ENGINEERING

By

Thimmappa Sravan Kumar

Roll No. 716153

Supervisors

Dr. Brahma Raju Golla

Assistant professor, NIT Warangal

Dr. V. V. Bhanu Prasad

Scientist 'G', DMRL Hyderabad

Department of Metallurgical and Materials Engineering

National Institute of Technology, Warangal- 506 004

June 2021

DEPARTMENT OF METALLURGICAL AND MATERIALS ENGINEERING

NATIONAL INSTITUTE OF TECHNOLOGY

WARANGAL – 506004 (T.S) INDIA

CERTIFICATE

This is to certify that the work presented in the dissertation entitled "**Development of ZrB_2-SiC-Si_3N_4/Ta Ceramic Composites for High Temperature Applications"** submitted to the National Institute of Technology, Warangal by Mr. Thimmappa Sravan Kumar (Roll. No 716153), for the award of **Doctor of Philosophy** in **Metallurgical and Materials Engineering** is a record of bonafide research work carried out by him under the supervision of Dr. Brahma Raju Golla (Asst. Prof., NIT Warangal) and Dr. V.V. Bhanu Prasad (Scientist 'G', DMRL Hyderabad). The results presented in this dissertation have not been submitted in either part or full elsewhere for any research degree.

Dr. Brahma Raju Golla

Assistant Professor & Thesis Supervisor

Department of Metallurgical and Materials Engineering

National Institute of Technology Warangal

Warangal-506 004 (T.S) India

Dr. V.V. Bhanu Prasad

Scientist 'G' & Thesis Co-supervisor

Ceramic and Composites Group

Defence Metallurgical Research Laboratory

Hyderabad- 500 58 (T.S) India

DECLARATION

I, **Thimmappa Sravan Kumar,** hereby declare that this dissertation work entitled **"Development of ZrB_2-SiC-Si_3N_4/Ta Ceramic Composites for High Temperature Applications"** submitted in partial fulfilment for the award of degree of **Doctor of Philosophy** to the Department of Metallurgical and Materials Engineering, National Institute of Technology, Warangal is a bonafide work which was carried out by me under the supervision of **Dr. Brahma Raju Golla** and **Dr. V.V. Bhanu Prasad**. I also declare that the content of this thesis has not been submitted previously in part or full in any University or Institute for the award of any degree or diploma.

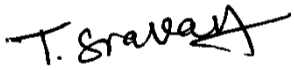

Thimmappa Sravan Kumar

Roll No. 716153

Department of Metallurgical and
Materials Engineering

Thesis Approval for PhD

The thesis entitled "**Development of ZrB_2-SiC-Si_3N_4/Ta Ceramic Composites for High Temperature Applications**" by **Thimmappa Sravan Kumar** is approved for the degree of **Doctor of Philosophy** in Metallurgical and Materials Engineering.

Examiners

Supervisors

Dr. Brahma Raju Golla
Supervisor

Dr. V. V. Bhanu Prasad
Co- Supervisor

Chairman

Date:

ACKNOWLEDGEMENTS

It is my pleasant duty to acknowledge the people who have helped me during the tenure of the research work reported in the present thesis.

I express special gratitude to my research guides **Dr. Brahma Raju Golla**, Department of Metallurgical and Materials Engineering, National Institute of Technology, Warangal and **Dr. V. V. Bhanu Prasad**, Scientist 'G', Ceramic and Composites Group (CCG), Defence Metallurgical Research Laboratory, Hyderabad for their inspiring guidance, keen interest, motivation, involvement and constant supervision throughout the course of this work. Without their patient mentorship, constant inspiration, valuable discussions and suggestions, this thesis wouldn't have been possible.

I thank **Dr. Bhaskar Majumdar**, Magnetic Materials Group (MMG), DMRL, Hyderabad for support and permitting to use the Spark Plasma Sintering facility to carry out my work. I am also thankful to the technicians of MMG for their constant help. I thank **Dr. P. Suresh Babu**, ARCI, Hyderabad, for his help during nano-indentation experiments and his valuable suggestions.

I take this opportunity to thank **Dr. Asit Kumar Khanra**, Associate Professor and Head of the Department and members of Doctoral Scrutiny Committee– **Prof. N. Narasaiah**, **Dr. Uma Maheswara Rao**, Assistant Professor, Department of Metallurgical and Materials Engineering, and **Dr. D. Paul Joseph**, Assistant Professor, Department of Physics, for their useful suggestions and periodical review of my progress during this course of PhD work. I also would like to thank all the faculty members of MMED for their support and help during the course of PhD.

I thankfully acknowledge the financial support received from Science and Engineering Research Board (SERB) of Department of Science and Technology (DST), Govt. of India.

I take this opportunity to acknowledge with sincere gratefulness to my friends and colleagues **Dr. Md. Ali Shaik**, **Mr. C. Ravikanth Reddy**, **Mr. K. V. Ashish** and **Mr. Shiva Bejjugama**.

I also thank technical staff **G. Savvaiah**, Mechanic A grade (Retired), **Md. Fayaz**, Technical Assistant, **Nandu**, Technical Assistant and other technical and office staff of Metallurgical and Materials Engineering Department, NIT Warangal for their help during this research work.

Finally, I express my sincere thankfulness to my family for their love, patience and sacrifices to make this achievement a reality.

Thimmappa Sravan Kumar

ABSTRACT

The research depicted in this dissertation focuses on the processing of ZrB_2-based composites reinforced with Si_3N_4/Ta and understanding its microstructure, mechanical and oxidation properties. The ZrB_2-20vol.% SiC composites were processed with reinforcement of varying amounts (2.5, 5.0 and 10.0) of Si_3N_4 (vol.%)/Ta (wt.%). The ZrB_2 composites were processed by multi stage spark plasma sintering over a range of temperature (1800–1900 °C) for 3 min under 50 MPa. All the ZrB_2-SiC-Si_3N_4/Ta composites could be densified to more than 98% theoretical density (ρ_{th}) after SPS at 1900 °C.

High density (>98%ρ_{th}) of the ZrB_2-20vol.% SiC composites was obtained with 2.5vol.% Si_3N_4 addition. However, the density was slightly lowered when higher amount (≥5vol.%) of Si_3N_4 was added to the ZrB_2-20vol.% SiC. The XRD and SEM-EDS analysis of the ZrB_2-SiC-Si_3N_4 composites revealed the presence of reaction product phases (ZrO_2, BN, ZrN) along with SiC and ZrB_2 major phases. Sintering reactions were proposed to explain the existence of such new phases and extinction of Si_3N_4. Thermo-Calc software was also used to further confirm the formation of these new phases in the ZrB_2-SiC-Si_3N_4 samples. The hardness of the composites varied between 25.50 and 30.56 GPa, in particular, ZrB_2-20vol.% SiC-5vol.% Si_3N_4 measured with the maximum hardness. The cross-sectional microstructure of oxidized ZrB_2-SiC-Si_3N_4 composites consists of thick dense outer layer of SiO_2, intermediate (ZrO_2-SiO_2) layer and unreacted bulk after oxidation at 1500 and 1600 °C for 10 h. The formation of dense SiO_2 layer and absence of SiC depleted layer from the oxidized samples are signatures of improved oxidation resistance of Si_3N_4 reinforced ZrB_2-20vol.% SiC.

In case of ZrB_2-20vol.% SiC-Ta composites, almost full density (>99% theoretical density) was achieved after MS-SPS at 1900 °C for 3 min. Interestingly, the microstructure of ZrB_2-based composites exhibited core-rim structure and it consists of major crystalline phases of ZrB_2 core, (Zr, Ta)B_2 rim, SiC along with minor amounts of ZrO_2 and (Zr, Ta)C solid

solution phases. Both the nanoindentation and Vickers hardness of ZrB_2 composites exhibited similar trend and almost same hardness values. However, maximum nanoindentation hardness (18.62 GPa) and elastic modulus (451.60 GPa) were measured for ZrB_2-20vol.% SiC with 10wt.% Ta. The increase in amount of tantalum addition reduced the specific weight gain and oxide layer thickness of ZrB_2-20vol.% SiC. In particular, ZrB_2-20vol.% SiC with 10wt.% Ta exhibited better oxidation resistance compared to other compositions after oxidation at 1500 and 1600 °C for 10 h. In all the compositions, the cross-sectional microstructure of oxidation tested samples consists of three different layers such as top passive silica layer, intermediate SiC-depleted layer and unreacted bulk.

Overall, it was clear that the Si_3N_4 and Ta addition resulted different microstructures, aided in the densification and improved mechanical and oxidation properties of ZrB_2-20SiC. However, ZrB_2-SiC-Si_3N_4 exhibited much better oxidation resistance than ZrB_2-SiC-Ta ceramics. The ZrB_2-SiC-Si_3N_4 ceramics characterised with no SiC depleted layer and exhibits relatively better oxidation resistance than ZrB_2-SiC-Ta composites.

Keywords: ZrB_2-SiC composite; Si_3N_4; Ta; Spark plasma sintering; Densification; Microstructure; Mechanical properties; Oxidation

NOMENCLATURE

SYMBOLS

ρ	Density
ρ_{th}	Theoretical density
A	Area
E	Elastic modulus
E_r	Reduced modulus
E_s	Sample modulus
FS	Flexural strength
FT	Fracture toughness
G	Average grain size
G_o	Initial grain size
GS	Grain size
H	Hardness
H_v	Vickers hardness
h	Displacement
K	Thermal conductivity
n	Grain growth coefficient
p	Load
RD	Relative density
t	Sintering time
Z	Atomic number

ABBREVIATIONS

AC	Alternating current
BSE	Back scattered electron
CSPS	Conventional spark plasma sintering
CTE	Coefficient of thermal expansion
DC	Direct current
EBSD	Electron backscatter diffraction
EDM	Electric discharge machining
EDS	Energy dispersive spectroscopy
FESEM	Field emission scanning electron microscopy
FS	Flash sintering
FSPS	Flash spark plasma sintering
hcp	Hexagonal close-packed
HP	Hot-pressing
MP	Melting point temperature
MS-SPS	Multi stage spark plasma sintering
PS	Pressureless sintering
SE	Scanning electron
SEM	Scanning electron microscope
SPS	Spark plasma sintering
Ta	Tantalum
TEM	Transmission electron microscopy
TPS	Thermal protection system
UHTC	Ultra-high temperature ceramics
WLE	Wing leading edge
XRD	X-ray diffraction

LIST OF FIGURES

LIST OF TABLES

Contents

Chapter 1

Introduction

1.1 Background and motivation

In recent times, there has been growing research interest in thermal protection systems (TPS) for hypersonic vehicles and space re-entry vehicles to use them in extreme high temperature conditions [1]–[5]. The vehicle with flight speed (~1.7 km/s) of Mach number from 5 to 10 are considered as hypersonic flight vehicles. At such high speeds aerothermal heating is developed with extreme high temperatures at the leading edges of hypersonic vehicles [1], [2]. The TPS of reusable space vehicles must be able to withstand ultra-high temperature, high heat flux and stress associated with mechanical vibrations during launch and re-entry into earth's atmosphere. Therefore, it is required that TPS materials should provide good thermal shock and oxidation resistance as well as dimensional stability. Hence, the materials used in the application of TPS should have high melting point temperature, high thermal conductivity, low density, chemical stability and good mechanical properties [6], [7]. At extreme high working temperatures (beyond 1500 °C) materials will oxidize rapidly, which directs to the catastrophic failure of the system [8], [9]. So, the selection of suitable material is a major concern for the dream of hypersonic vehicle systems.

Carbon fiber reinforced carbon composites (C/C) have gained good recognition in hypersonic and re-entry applications, due to their high strength to weight ratio and good high temperature strength retention. But, C/C composites are prone to high temperature oxidation at temperature above 500 °C and therefore it can be used for short durations with less structural loading. To control this situation suitable coating including ultra-high temperature ceramics (UHTC) were used on C/C composites [10]–[12]. The SiC coated C/C composites have been used in the leading edge up to temperature of 1650 °C and this material could not sustain even

for small duration of time [13], [14]. There is also a risk of crack formation during thermal heating due to mismatch in coefficient of thermal expansion (CTE) of C/C composite and coating material. But NASA succeeded in flying of hypersonic vehicle made with SiC and HfC coated C/C composites. This success has drawn more attention of the researchers to study about high temperature ceramics [15]–[17].

The structural materials like SiC, Si_3N_4 based ceramics, oxide ceramics and C/C composites were used as thermal protective systems. Silicon based ceramics were used in high temperature oxidation environments due the formation of SiO_2 protective film on the surface of the oxidized composite. Even though silica is an excellent barrier to oxygen diffusion, it is not advisable to use at the temperature above 1600 °C. Because at temperature above 1600 °C, the silica layer softens and vapor pressure increases in the low oxygen atmosphere, which limits the use in high temperature applications [18]–[21]. On the other hand, refractory oxides such as ZrO_2 and HfO_2 can be used as oxidizing environment at temperature above 2000 °C due to its chemically inert behaviour. Even though it has good chemical inertness, it is limited to use in real-time applications due to its poor thermal shock resistance and less creep resistance at higher temperatures [13], [22].

In the past few years, UHTC have received good attention for the production of reusable TPS for the leading edges of hypersonic vehicles [23]. The UHTC materials exhibit melting temperature of more than 3000 °C and it can be used in the temperature regime of 2000 °C in air [24]–[27]. The transition metal borides, nitride and carbides belong to the category of UHTC [28]. **Figure 1** shows the class of different materials with melting point temperature more than 3000 °C. From **Figure 1,** it is observed that the refractory metals such as W, Re and Ta have melting point temperature more than 3000 °C, but during oxidation these metals shows inferior properties. Some of the oxides, borides, carbides and nitrides of IVB and VB group transition metals have been assessed as UHTC [29]–[31]. The oxides, carbides and nitrides have less

thermal conductivity and mechanical properties, so the research is narrowed down to the borides. Diborides show good combination of properties such as high melting point, low to moderate density, hardness, thermal conductivity, good creep resistance and excellent chemical inertness compared to transition metal carbides and nitrides and it is reported in **Table 1.1**.

Table 1.1 Basic physical and mechanical properties possessed by various ultra-high temperature ceramics [24], [26], [31]–[33]

Material	MP (°C)	ρ (g/cc)	CTE (α; 10^{-6} K^{-1})	K(W/m-K)	E (GPa)	H(GPa)	FT ($MPam^{0.5}$)	FS (MPa)	Oxidation (°C)
TiB_2	3225	4.5	8.6	60-120	500-560	25-35	4-5	700 - 1000 (3-point)	< 1200
ZrB_2	3243	6.1	6.8	60-135	340-500	20-25	4	300-400	1200 - 1400
HfB_2	3380	11.2	6.3	104	480	21-28	3.5-5.7	350-450 (4-point)	1200 - 1400
TaB_2	3040	12.5	8.2	86	248-551	20-25	3.5-4.5	555 (4-point)	1200 - 1400
NbB_2	3036	6.9	7.7	16.7	637	21	4	414 (3-point)	-
HfC	3900	12.8	6.6	20	300-340	26		250-350	< 800 > 1800
TaC	3800	14.5	6.3		470-540	14-19	3.4	600 - 700	< 1400
ZrC	3530	6.6	6.7	20.5	480	27	2	400 (3-point)	< 800 > 1800
NbC	3500	7.6	6.7		338	20			< 800 > 1800
TiC	3100	4.9	7.7		451				
TiN	2950	5.4	9.3	19.2		31			
ZrN	2950	7.3	7.2	20.5	380			330	< 800
HfN	3385	13.9	6.9	23	420			290-350	< 800

(MP- Melting point temperature, ρ- Density, CTE- Coefficient of thermal expansion, K- Thermal conductivity, E- Elastic modulus, H- Hardness, FT- Fracture toughness and FS- Flexural strength)

It is observed that ZrB_2 is more promising material among other diborides due to its moderate density, low CTE values and high oxidation resistance. In this dissertation, the material of focus is ZrB_2, which has high melting point temperature (3243 °C), moderate

density (6.1 g/cm^3), high thermal conductivity (60-135 W/m-K), low CTE (6.8×10^{-6} K^{-1}) and high temperature oxidation resistance.

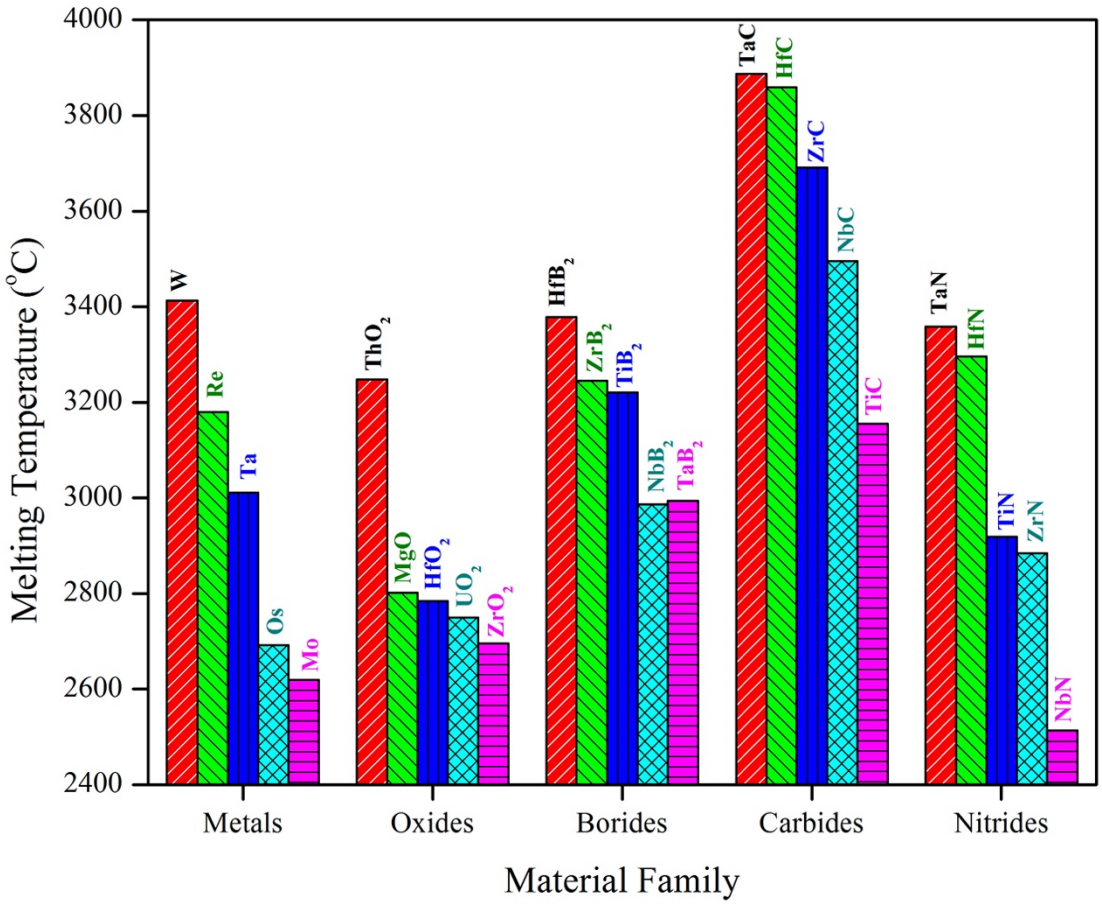

Figure 1.1 The melting temperature of the different family of materials with melting point more than 2000 °C. The family of borides having melting temperature more than 3000 °C.

The combination of different properties gives the opportunity to use ZrB_2 materials in the application of molten metal crucibles, armor materials, neutron irradiation shield in nuclear applications, rocket nozzles, solar absorption and high temperature structural parts [34]–[39]. The ZrB_2 ceramics have superior thermo-physical properties and oxidation resistance compared to other lightweight materials such as C/C, SiC/SiC and C/SiC composites. In the point of good electrical conductivities, the diborides can be machined easily using electric discharge machining (EDM) to make complex shapes [40], [41].

1.2 Novelty of the work

In the literature, the transition metal silicides, carbides, nitrides or borides have been widely studied to improve properties of ZrB_2-based composites [25]. Also, recently the effect of transition metals on thermal properties of ZrB_2 has been explored [24-26], [37-39], [44]. In this work, for the first time an attempt has been made to explore the effect of Si_3N_4 ceramic additive and tantalum (Ta) transition and refractory metal addition on the densification, microstructural phase evolution, mechanical properties and oxidation behavior of ZrB_2-20vol% SiC. A careful literature review revealed that ZrB_2-20vol.% SiC is an ideal composition for high temperature applications of ZrB_2, and hence the ZrB_2-20vol.% SiC composite was selected as a baseline composition.

As far as the novelty of the present work is concerned, multi stage spark plasma sintering (MS-SPS) was employed to densify ZrB_2-20vol.% SiC-(2.5-10) Si_3N_4/Ta composites. Limited research is available on Si_3N_4 reinforced ZrB_2 ceramics and also use of MS-SPS in developing boride ceramics. The combined effect of SiC and Si_3N_4/Ta (ceramic/metallic additive) on ZrB_2 has not been explored much in the reported literature. In fact, Si_3N_4 is one of the important silicon-based ceramics that has potential for high temperature applications. Also, there is no much studies on the use of Ta as a sintering additive on the densification, microstructure and properties of ZrB_2 ceramics. In the light of this, an attempt was made to find whether ZrB_2 ceramics could be densified at low sintering temperatures? Efforts were made to understand underlying sintering mechanisms, microstructure and mechanical properties of ZrB_2-20SiC-Si_3N_4/Ta. The isothermal oxidation tests were performed at 1500 and 1600 °C for a duration of 10 h to assess thermal stability of the ZrB_2 composites.

1.3 Objectives of the present work

The present work aims at meeting the following objectives.

1. Optimize the sintering parameters of spark plasma sintering (SPS) by following multi-stage heating schedule.

2. Processing of ZrB_2-20vol.% SiC with varying amounts (2.5, 5.0 and 10.0) of Si_3N_4 (vol.%)/Ta (wt.%) addition and evaluate its effect on densification, microstructure and mechanical properties.

3. Study the oxidation behaviour of ZrB_2-20SiC-Si_3N_4/ZrB_2-SiC-Ta composites at high temperatures (1500 and 1600 °C)

4. Compare and understand the performance of ZrB_2-20SiC-Si_3N_4 and ZrB_2-20SiC-Ta composites and relating it with other ZrB_2-based composites reported in the literature.

1.4 Organization of thesis

The dissertation contains 9 chapters. The 1st chapter states the highlights of the present work, objectives and novelty of thesis in brief. The 2nd chapter discusses the literature review of ZrB_2 based ceramic and composites. This chapter gives brief idea of different processing routes, mechanical properties and oxidation behavior of ZrB_2-based materials. The 3rd chapter presents the information of materials and experimental methods used in the dissertation. The 4th and 5th chapters discuss the effect of Si_3N_4 addition on densification of ZrB_2-SiC composites and its oxidation behavior at different test conditions. Further, 6th and 7th chapters explain the effect of Ta addition on the densification of ZrB_2-SiC composites and its oxidation behavior at different test conditions. Finally, 8th and 9th chapters discuss the conclusions of this dissertation and future scope of the work. The references used in dissertation has been showed at the end.

Chapter 2

Literature review

2.1 Crystal structure of ZrB_2

ZrB_2 exhibits hexagonal close-packed (hcp) crystal structure (AlB_2 type, P6/mmm space group) as shown in **Figure 2.1**. It is the layered structure settled in a hexagonal close packed system with alternating Zr-atoms and B-atoms layers, which usually form 2-dimensional rings, perpendicular to the c-axis [25], [42]. Alternate stacking sequence of Zr planes with B network along c-direction. Each Zr atoms is surrounded by six equidistant Zr atoms and 12 equidistant B atoms, on the other hand each B atom has six equidistant Zr atoms and three equidistant B atoms [43], [44]. Three types of chemical bonds are present with the ZrB_2 system. These bonds are characterized as B-B, Zr-B and Zr-Zr. B-B bonds are generally covalent nature, Zr-B bonds are mixed bonds of ionic and covalent and Zr-Zr bonds are metallic [45]. The strong covalent bonds are responsible for high melting temperature and high strength, while metallic and covalent bonds are responsible for good conductivity of ZrB_2 ceramics [31].

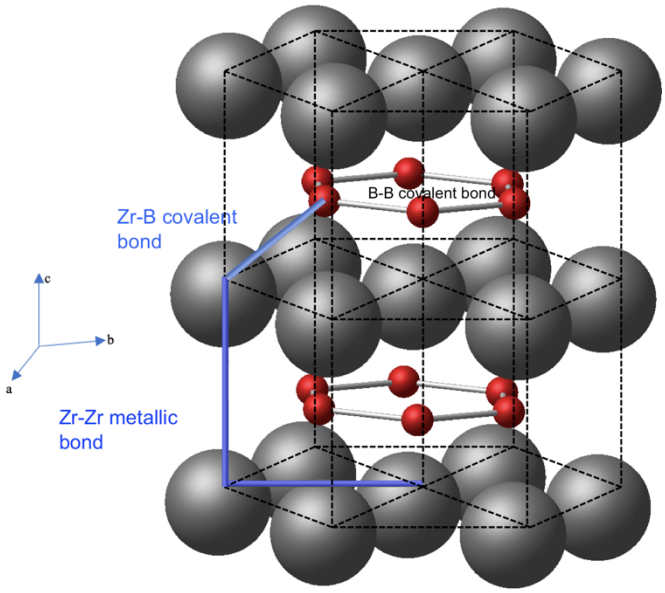

Figure 2.1 Crystal structure of ZrB_2 ceramic [46]

2.2 Synthesis of ZrB_2 powders

The starting ZrB_2 powders characteristics such as purity, morphology, particle size and defect concentration strongly influence the sinterability of ZrB_2. All these characteristics are very much interdependent on the use of different powder synthesis conditions. In general, the ZrB_2 powder were synthesized using chemical routes such as reduction process, reactive technique, sol-gel processing and mechano-chemical routes [38], [43], [47]–[50]. However, the limited factor for the synthesis of ZrB_2 powders are the relatively higher cost for boron in elemental form and low production rates. On the other hand, ZrB_2 powders produced via reaction route in the laboratory consists of high amount of oxygen (~2.4wt.%) impurity as compared to commercially available ZrB_2 powders (~0.9-1.0wt.% oxygen impurity in H.C. Starck Grade B) [51], [52]. Typically, the ZrB_2 powders synthesized by reduction processes using reducing agents such as boron, carbon, silicon, B_4C, aluminium, magnesium or combination of them. The large-scale processing of micron-sized ZrB_2 powders commonly synthesized by high-temperature reduction techniques using electric furnaces. In these powders, some amounts of inevitable impurities such as metals, residual carbon and oxides are present [53].

Generally, ZrB_2 powders obtained from the following reduction processing techniques:

(a) Carbothermic reduction reaction

$$ZrO_2 + B_2O_3 + 5C = ZrB_2 + 5CO \quad (1)$$

(b) Boron carbide reduction reaction

$$2ZrO_2 + B_4C + 3C = 2ZrB_2 + 4CO \quad (2)$$

$$3ZrO_2 + B_4C + B_2O_3 + 8C = 3ZrB_2 + 9CO \quad (3)$$

$$ZrC + ZrO_2 + B_4C = 2ZrB_2 + 2CO \quad (4)$$

(c) Aluminothermic, magnesiothermic and silicothermic reduction reaction

$$ZrO_2 + B_2O_3 + 3.334Al = ZrB_2 + 1.667Al_2O_3 \quad (5)$$

$$ZrO_2 + B_2O_3 + 5Mg = ZrB_2 + 5MgO \quad (6)$$

$$ZrO_2 + B_2O_3 + 2.5Si = ZrB_2 + 2.5SiO_2 \quad (7)$$

(d) Borothermic reduction reaction

$$ZrO_2 + 4B = ZrB_2 + B_2O_2 \quad (8)$$

Generally, these reactions are endothermic and are feasible at the temperature more than 1200 °C. In particular, the carbothermic reduction reactions require the temperature in the range of 1500-2000 °C. These chemical reactions involve the production of high amounts of gases and it is required to remove them from the reaction furnace for further reactions to proceed, even if these synthesized powders have the impurities of oxides, carbides and carbon [50].

The reactive process is one of the simplest methods, which involves the reaction between elemental precursor powders and leads to the production of high quality ZrB_2 powders.

$$Zr + 2B = ZrB_2 \quad (9)$$

This process has to be carried out in inert or reducing environment to control the formation of oxide impurities and these reaction are extremely exothermic and possible at all temperatures [53]–[55]. However, the commercial or laboratory synthesized powders have some impurities, which are originated from the raw powders, during powder processing or contaminated during further handling of powders and or sintering [51].

2.3 Sintering techniques for the consolidation of ZrB_2

The densification of single phase ZrB_2 is difficult due to its low self-diffusion coefficient, strong covalent bonding nature, high melting point and presence of surface oxide impurities (ZrO_2 and B_2O_3) present on the powder particles [25]–[27], [39]. Due to that high sintering temperatures (often more than 2000 °C) required to achieve fairly dense single phase ZrB_2 ceramic (say>95% of theoretical density (ρ_{th})), especially upon using conventional pressureless sintering technique. The densification is a function of sintering temperature and sintering/holding time. At low sintering temperatures, lower sintering densities are achieved with controlled grain size, but mechanical properties are reduced due to high amount of porosity. On the other hand, at high sintering temperatures, grain growth becomes predominant over the densification, which

leads to inferior mechanical properties [56]. For single phase borides, the following equation shows the relation between sintering time and average grain size [57].

$$G = G_o + Kt^n \quad (10)$$

Where, G_o is the initial grain size, G is the average grain size, t is the sintering time and n is grain growth coefficient.

Generally, starting powders have the surface impurities like ZrO_2 and B_2O_3, which inhibits the densification and promotes the rapid grain growth. At high temperatures during sintering boria get evaporated. The left out residual ZrO_2 is stable and chemically inert and they are susceptible of phase transition at higher temperatures and adversely affect the high temperature properties of ZrB_2 [58]–[60]. Hence, to achieve full densification with controlled grain growth is the main challenge in developing ZrB_2 or diboride ceramics. These are the different approaches followed for improving the densification with minimal grain growth.

- Refinement of starting powders particle size and/or improving the defect concentration by high-energy ball milling [61]
- Use of pure and ultra-fine synthesized powders [48]
- High temperature reactive sintering of solid precursors [62]
- The addition of sintering additive [39], [63]

The addition of different sintering additives to ZrB_2 material is the most widely studied approach. The reinforcements can be ceramics or metals, added in different amounts in different forms like crystalline, amorphous and precursors. Generally, when metals added to ceramics, at sintering temperatures they melt and aids in the densification by liquid phase sintering [64], [65]. On the other hand, when non oxide ceramics added to base material, the additives remove the oxide phases present on the surface of ZrB_2 and enhanced the densification by solid state or liquid phase sintering [66]–[68]. The additives and impurities form low temperature eutectics with transition metal diborides, which controls their high temperature properties [69]. Generally, SiC, Si_3N_4, B_4C, BN, WC, AlN, $MoSi_2$, $TaSi_2$, $TiSi_2$ etc. have been added as

sintering additives to ZrB_2 to enhance the densification [70]–[72]. The ZrB_2 ceramic and its composites have been processed by different sintering routes, such as pressureless sintering (PS), hot-pressing (HP), spark plasma sintering (SPS) and flash sintering (FS).

2.3.1 Pressureless sintering

PS is easy and economical technique to develop dense compacts. Initially the green compact is made by uniaxial die compaction with good handling strength. Then, these green pellets are heated in controlled environment at high temperatures for several hours [60], [73]. This technique is economical to develop near net shape products due to less machining costs [33], [74]. The borides required the sintering temperatures in the range of 2000-2300 °C for obtaining full densification using this processing approach. Due to continuous holding at high sintering temperatures, it leads to grain growth of borides. In pressureless sintering of ZrB_2, coarsening is associated with grain and pore growth, and it results in a lower driving force for densification due to decreased surface area of the powder compact [75].

ZrB_2 could be densified to only ~72% ρ_{th} even upon sintering at 2150 °C for 3 h [76]. The relative density of ZrB_2 could be improved to ~98% with increased holding time of 9 h. However, such prolonged holding time at high temperatures resulted in rapid grain growth. The average grain size of ZrB_2 was reported to be ~9 μm along with the occasional presence of coarser grains (~30 μm). The ZrB_2 processed via PS exhibited inferior mechanical properties and is mainly due to coarse grain structure [75], [77]. Overall, near-theoretical sinter-density of ZrB_2 via pressureless sintering is achievable upon using very high sintering temperatures (> 2000 °C) and also by adding sinter additives (relatively at low sintering temperature). But high sintering temperature leads to melting and even vaporization of low melting components; which in turn lead to microstructural coarsening [75]. Ahmadi et al. observed that as the amount of Si_3N_4 increases to ZrB_2-SiC composite, results in lowering of the sinter density due to evaporation and formation of gaseous phases during pressureless sintering at 1900 °C

[78]. However, even with the same constraints, the same compositions were densified to near theoretical density using hot-pressing at similar temperature of 1900 °C.

2.3.2 Hot-pressing

The densification of monolithic diborides is difficult and HP is the popular technique to obtain fully densified compacts at relatively lower temperatures than PS [79], [80]. The powders are filled in graphite die and then heated to required temperature in vacuum, when the die reaches to the required temperature, uniaxial pressure applied hydraulically in the range of 30-40 MPa. The density and microstructure of sintered samples depend on hot pressing temperature, heating rate, holding time and applied pressure during sintering. The method used to process simple geometrical shapes and complex shapes cannot be processed using HP method [72], [81]–[83].

The monolithic ZrB_2 ceramic is reportedly densified to 87%ρ_{th} at hot-pressing conditions of 1900 °C, 30 MPa for 30 min [84]. ZrB_2 achieved near theoretical density with the addition of (5-40vol.%) B_4C after hot pressing at 1900 °C for 30 min under pressure of 32 MPa [85]. Patel et al. obtained 97.5%ρ_{th} at hot-pressing conditions of 2000 °C, 25 MPa for 60 min and as the amount of B_4C increased (from 0-5wt.%) relative density of ZrB_2 increased and grain size reduced. It was proposed that B_4C enhanced densification by removing surface oxides from the starting powders and restricted the grain growth of ZrB_2 [86]. Chamberlin et al. prepared high strength ZrB_2-30vol.% SiC ceramic composite at 1900 °C for 45 min and under uniaxial pressure of 32 MPa. They reported good combination of mechanical properties, such as flexure strength of 1090 MPa, elastic modulus of 480 GPa, hardness of 24 GPa and fracture toughness of 5.3 $MPam^{0.5}$ [87].

The mechanical properties of ZrB_2 ceramics processed via pressure assisted sintering techniques are relatively better when compared to those developed via pressureless sintering. Such differences are partly due to the finer microstructures, along with the slightly superior relative density for ZrB_2 developed via pressure assisted sintering techniques.

2.3.3 Spark plasma sintering

SPS is an advanced sintering technique that employs pulsed direct electric current via the electrodes at the top and bottom punches of the conducting graphite die, in addition to uniaxial pressure, to produce dense sintered materials with significantly greater heating rates and lesser holding times at the sintering temperatures [88]–[95]. Overall, SPS may be considered a modification of the hot press, with the fundamental difference being the passage of pulsed direct current (DC) through the die/punch and powder compact as shown in **Figure 2.2** [91]. In SPS, the sample is heated through direct heating of the die, unlike hot press which involves indirect heating. During SPS, the combination of a low voltage, high intensity pulsed DC and uniaxial pressure offers the possibilities of achieving rapid heating rates (up to ~1000 °C/min) and very short holding times to obtain highly dense samples [92], [93].

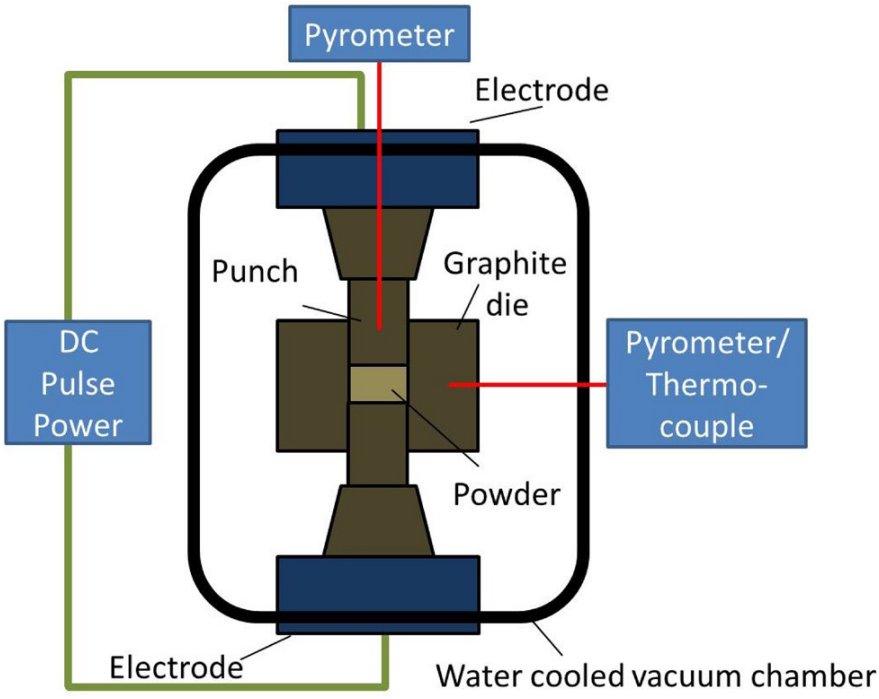

Figure 2.2 Schematic representation of an SPS apparatus [96]

The SPS processing follows mainly two steps

(a) Plasma activation: The pulse direct contact flows through graphite dies and powders from the graphite punches. The high intensity DC flows through graphite dies develops a large amount of joule heating, this heat is one of the sources for powders densification. Further,

current flows through the powders, which develops the plasma as an effect of the spark discharge of some gaseous phases in the gap between the powders, developing high-speed particles flow in reverse, which employs high punch pressure on the particles and thereby blows away the broken oxide film and activating the particles surface. This effect is also known as the electron wind effect [96], [97].

(b) Thermoplastic deformation: Due to joule heating and discharge heat in contact zone and non-contact zone, respectively between powder particles and instantaneously high-temperature zone is formed. This high temperature zone leads to melting and evaporation of powder particles surface for the developments of necks around the particles contact zone and the diffusion of powder particles increases significantly. The diffusion coefficient of powders in SPS processing is higher than that of general HP conditions, thereby understanding that powders sinters quickly, with less sintering temperature and time and with controlled grain growth [88], [96], [98].

The spark plasma sintered diborides are usually observed to possess fine microstructure and good combination of properties. In order to address some issues related to non-uniform densification (and properties) primarily due to fast heating rate and lesser holding times, recently, researchers explored the application of MS-SPS schedule, which involves holding at one or more intermediate temperatures for few minutes before reaching the final sintering temperatures [41], [99]–[104]. Keeping the total holding time constant (i.e. lesser holding time at the final sintering temperature), more uniform densification and finer microstructures were achieved for ZrB_2 [102] and TiB_2 composites [104], resulting in still improved mechanical properties as compared to similar compositions sintered via the usual single-step SPS route.

2.3.4 Flash sintering

In contrast to other sintering techniques, flash sintering (FS) is energetically more efficient and takes even lesser sintering time than SPS. FS is one of the fastest approach to sinter the materials by direct Joule heating and thermal runaway [105]. Further, to reduce the grain size of the

ceramic during consolidation, FS came into picture. In FS, the current passes entirely through the sample and it involves direct application of AC or DC voltage across sinter body during heating. Once a certain threshold temperature is reached, a sudden non-linear increase in current leads to rapid Joule heating (the "flash") and the sinter body densifies within a few seconds [106]–[108]. The studies on this technique started in 2010 by Cologna et al. who densified the yttrium-stabilized zirconia at low temperature less than 5 s under the application of electric field [109]. The drawbacks of this technique where it can densify only a less amount of volume and shape of the sample (less than 100 mm^3 for a dog-bone shaped yttrium-stabilized zirconia sample [109]), and use costly electrodes (such as platinum and gold). Due to these reasons, FS is less attractive for large scale production even though it has small sintering times. This technique still needs preheating, which wastes too much energy and time. Therefore, Grasso et al. developed a unique approach to solve these issues by using a new technique, namely, flash spark plasma sintering (FSPS), to consolidate dense ZrB_2 [110]. They used special molds with conventional SPS (CSPS) equipment and applied high currents for 1 min for developing FS effects. To densify (98% ρ_{th}) ZrB_2 via CSPS at 2100 °C for 20 min 4 kWh energy was applied, while the same sample was densified to 95% ρ_{th} by FSPS using only 0.2 kWh. It corresponds to 95% of energy saving.

One of the reasons for the faster densification in the case of FSPS was the very rapid heating rate of around 4000 °C/min, when compared with 100 °C/min for CSPS. Additionally, the FSPS used very low voltages (FSPS <10 V) and energy saving of nearly 95% compared to the conventional SPS. The grain size of the sintered ZrB_2 was reported to be ~11.8 μm for the samples developed via FSPS, while it was ~18.2 μm for the sample developed via CSPS. In conventional sintering, considerably higher sintering temperatures and times are required for ZrB_2 when compared to those for SPS and FSPS. Furthermore, so far achievement of a maximum densification of ~95% ρ_{th} has been reported with ZrB_2 upon the usage of FSPS for very short sintering time of 30 s [110]–[112].

2.4 Densification of ZrB_2 ceramics and its composites

Different sintering additives such as SiC, C, B_4C, WC, ZrC, AlN, Si_3N_4, $MoSi_2$, $TaSi_2$ etc. are used to improve the densification of ZrB_2 ceramics. **Table 2.1** shows the densification and mechanical properties of different ZrB_2-based composites processed using different sintering methods. It is reported that carbon or carbide-based sinter-additives help in enhancing the densification of ZrB_2 primarily by removing the surface oxide impurities that are present on the ZrB_2 starting powders [25]. It may be reiterated here that elimination of surface oxides is very important since it inhibits densification by promoting grain growth through evaporation and condensation of the surface oxides during sintering. The various reactions are as the following [113]–[116]

$$ZrO_2 + C = ZrC + CO \quad (11)$$

$$ZrO_2 + 3WC = ZrC + 3W + 2CO \quad (12)$$

$$7ZrO_2 + 5B_4C \rightarrow 7ZrB_2 + 5CO + 3B_2O_3 \quad (13)$$

$$2ZrO_2 + 3B_2O_3 + 5SiC \rightarrow 3ZrB_2 + 5SiO_2 + 5CO \quad (14)$$

For example, **Figure 2.3** shows the effect of sintering additive (4wt.% B_4C) on the density obtained with ZrB_2 as-received and attrition milled powders as function of sintering temperature. The use of mechanically milled ZrB_2 powders having particle size of ~0.1 μm (as milled down from ~1 μm), along with sinter additives, allowed considerable reduction of the sintering temperature (to 1850 °C) for attaining almost near theoretical sinter density. It is evident that the addition of B_4C addition is beneficial towards enhancing the densification of ZrB_2 ceramics for as-received and milled powders as well [25]. Such improvement in densification is believed to be primarily due to the reaction between ZrO_2 oxide layer that was present on the surface of ZrB_2 powders with the added B_4C.

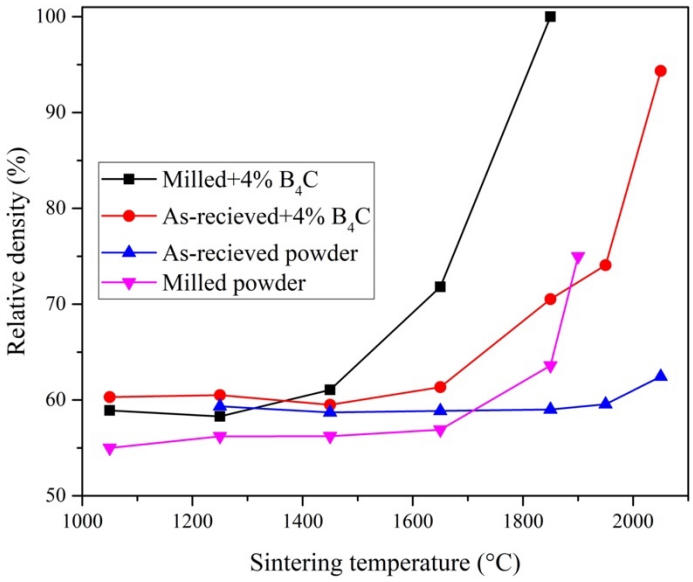

Figure 2.3 The effect of sintering additive (4wt.% B_4C) on the density obtained with ZrB_2 as-received and attrition milled powders as function of sintering temperature [25].

Among the carbides, SiC has been extensively used and investigated as a sintering additive since the SiC addition enhances densification, inhibits grain growth and improves mechanical, oxidation and other properties [29], [73], [117]–[121]. Use of SiC as sintering additive to ZrB_2 studied in different ways by varying SiC content (up to ~30vol.%), use of different sizes of SiC starting powders (viz., micron, sub-micron and nano-sized) [117], different forms of SiC (particulate, whisker and fibre) [121]–[123] and combining other additives along with SiC. It has been reported that the densification and densification rate of ZrB_2 ceramics gets enhanced with increasing SiC content due to liquid phase formation and control of grain growth [29]. Monteverde et al. reported that with the use of 10vol.% SiC (ultrafine, 0.8 μm), near-theoretical sinter-density could be achieved for ZrB_2 after hot press sintering at 1900 °C for 20 min in vacuum [118]. Similarly, in another work, ZrB_2 could be fully densified at still lower sintering temperature (HP at 1650 °C, 120 min) by using ~22.4vol.% nano sized SiC powders [39]. In both cases, liquid phase sintering was reported as main densification mechanism. In another work, Khoeini et al. further used carbon as sintering additive to improve the densification of ZrB_2-SiC via pressureless sintering. Removal of ZrO_2,

B_2O_3 and SiO_2 surface oxides on the starting powder particles aided the densification in the densification of ZrB_2-SiC composite [73].

Transition metal disilicides were also attempted as sintering additives for ZrB_2 [124]–[127]. The following sintering reactions take place with the silicides

(i) Sintering reactions with $MoSi_2$ sintering additive:

$$2MoSi_2\ (s) + B_2O_3\ (l) = 2MoB\ (s) + 2.5Si\ (l) + 1.5SiO_2\ (l) \quad (15)$$

(ii) Sintering reactions with $TaSi_2$ sintering additive:

$$2TaSi_2\ (s) + B_2O_3\ (l) = 2TaB_2\ (s) + 2.5Si\ (l) + 3SiO_2\ (l) \quad (16)$$

$$(1 - x)\ ZrB_2\ (s) + xTaB_2\ (s) = (Zr_{1-x}Ta_x)B_2\ (s) \quad (17)$$

The sintering temperature range for densification of ZrB_2 is influenced by melting point of the silicides used as the sinter aids [124]–[127]. The densification temperature (1600 °C) is lower for $ZrSi_2$ reinforced ZrB_2 when compared to other silicides since the melting point of $ZrSi_2$ is relatively low. Sciti and Silvestroni extensively studied the use of $MoSi_2$ sinter additive for ZrB_2 [37], [125], [128]–[130]. Their work revealed that achievement of near-theoretical density was possible for ZrB_2 with the use of $MoSi_2$ (3–20vol. %) via PS at 1900 °C, HP at 1800 °C and SPS at 1750 °C. The densification was assisted by transient liquid phase that formed due to the reaction between $MoSi_2$ and surface oxide impurities on ZrB_2, as was shown by Eq. (15). During hot pressing, the plastic deformation of silicides at high temperatures (>800 °C) would also contributes to the densification of ZrB_2 as the deformation forces soft silicide particles to fill in the voids left by ZrB_2 particles [125], [128].

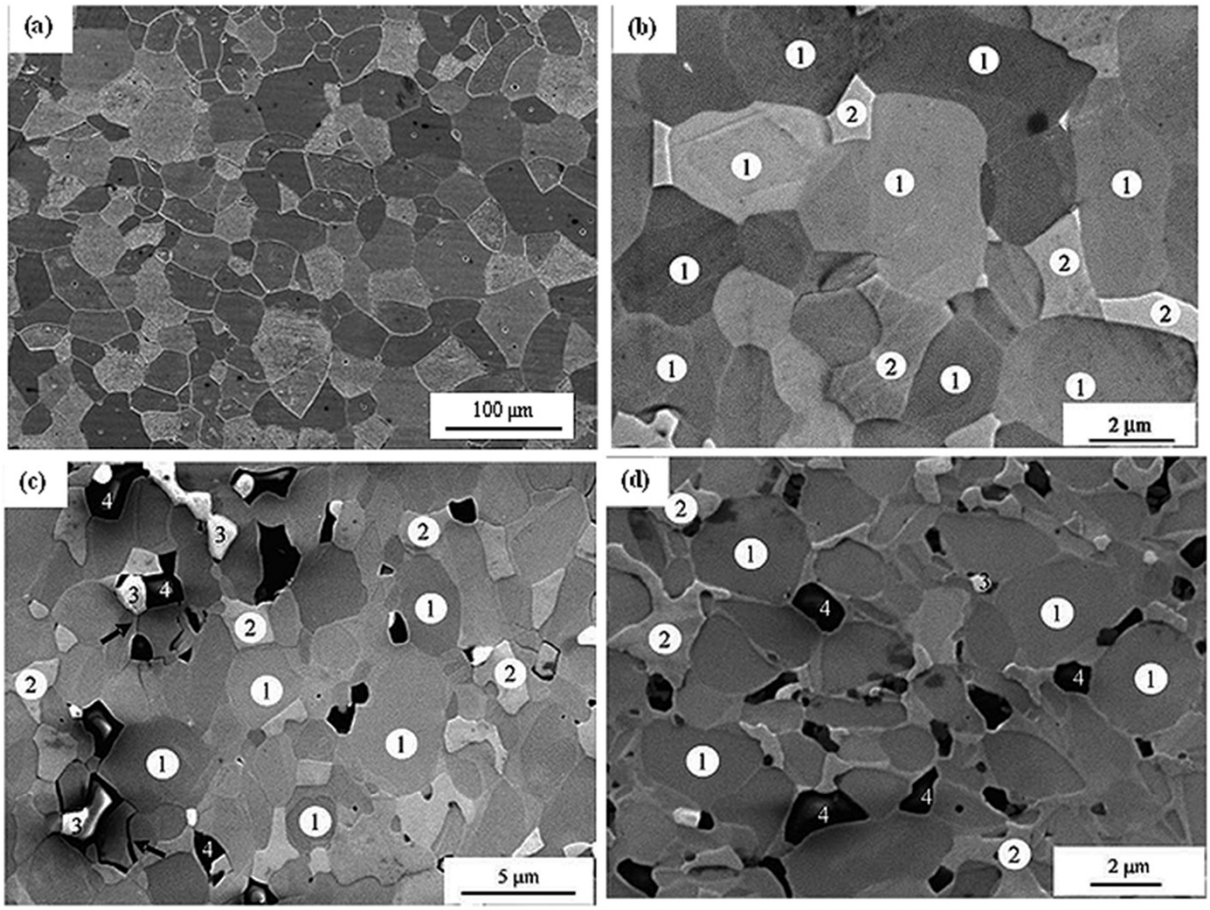

Figure 2.4 Sintering conditions influence microstructure development-scanning electron micrographs of (a) monolithic ZrB_2 (possessing near-theoretical sinter density) after hot-pressing at 2150 °C for 60 min [131]; (b) ZrB_2 containing 20vol.% $MoSi_2$ sinter-additive after pressureless sintering at 1850 °C for 30 min, with the microstructure consisting of only ZrB_2 (legend 1) and $MoSi_2$ (legend 2); (c) ZrB_2-15vol.% $MoSi_2$ hot pressed at 1750 °C for 20 min and (d) ZrB_2-15vol.% $MoSi_2$ spark plasma sintered at 1750 °C for 7 min, showing the presence of ZrO_2 (legend 3) and SiO_2 (legend 4) along with ZrB_2 and $MoSi_2$ [128].

Figure 2.4 shows the role of sintering aid and sintering route on the microstructure of sintered composite. **Figure 2.4 (a)** shows the microstructure of monolithic ZrB_2 after hot-pressing at 2150 °C, 32 MPa for 60 min with near theoretical density and grain size of 19.4 µm [131]. The resultant microstructure of ZrB_2-20vol.% $MoSi_2$ consisted of globular shaped ZrB_2 and irregular shaped $MoSi_2$ phases (**Figure 2.4 (b)**). This highlights the importance of sintering additive for the densification of ZrB_2. In the case of hot pressed and spark plasma sintered ZrB_2-

15vol.% $MoSi_2$ samples, fine microstructure with various phases such as ZrB_2, $MoSi_2$, SiO_2 and ZrO_2 were evident (**Figure 2.4 (c) and (d)**) [128]. The presence of such additional phases reflects on the occurrence of sintering reactions. In the case of ZrB_2-15vol.% WSi_2, the microstructure consists of ZrB_2 core surrounded by $(Zr,W)B_2$ solid solution, with refractory compounds (WC, WB and WSi_2) settled at triple junctions. This type of core-rim structure is believed to be beneficial for high-temperature strength of ZrB_2 composites, at least up to 1650 °C [132]. In **Figure 2.5 (a-d)** represents, FESEM and TEM characterization of hot-pressed (at 1930 °C, 40 MPa for 40 min) ZrB_2-15vol.% WSi_2 composites. The microstructure revealed the presence of ZrB_2 as core surrounded by $(Zr,W)B_2$ shell and various residual phases (W-C-O, WB, SiO_2, ZrO_2 and WSi_2). Manifestation of those new phases indicates involvement of sintering reactions. Monteverde and Silvestroni studied the combined effect of SiC and WC on the densification, microstructure and properties of ZrB_2 [120]. The microstructure of hot pressed ZrB_2-3SiC-5WC (vol.%) ceramic consisted of ZrB_2 core, $(Zr,W)B_2$ rim substructures, along with (Zr,W)C and SiC phases. It exhibited room temperature strength of 630 MPa, with the strength being increased to 720 MPa with further increasing of the test temperature to 1500 °C (in air). The solid solution formation, depletion of grain boundary phases and healing of surface flaws by the glassy oxide layer were believed to contribute to such impressive response of the material at elevated temperature. Recently, researchers started exploring the core-rim microstructure containing materials [69]. The core-rim structures facilitate to improve the high temperature mechanical properties and oxidation resistance. These type of materials are suitable in hot-regime as TPS applications which can accommodate high loads at high temperatures.

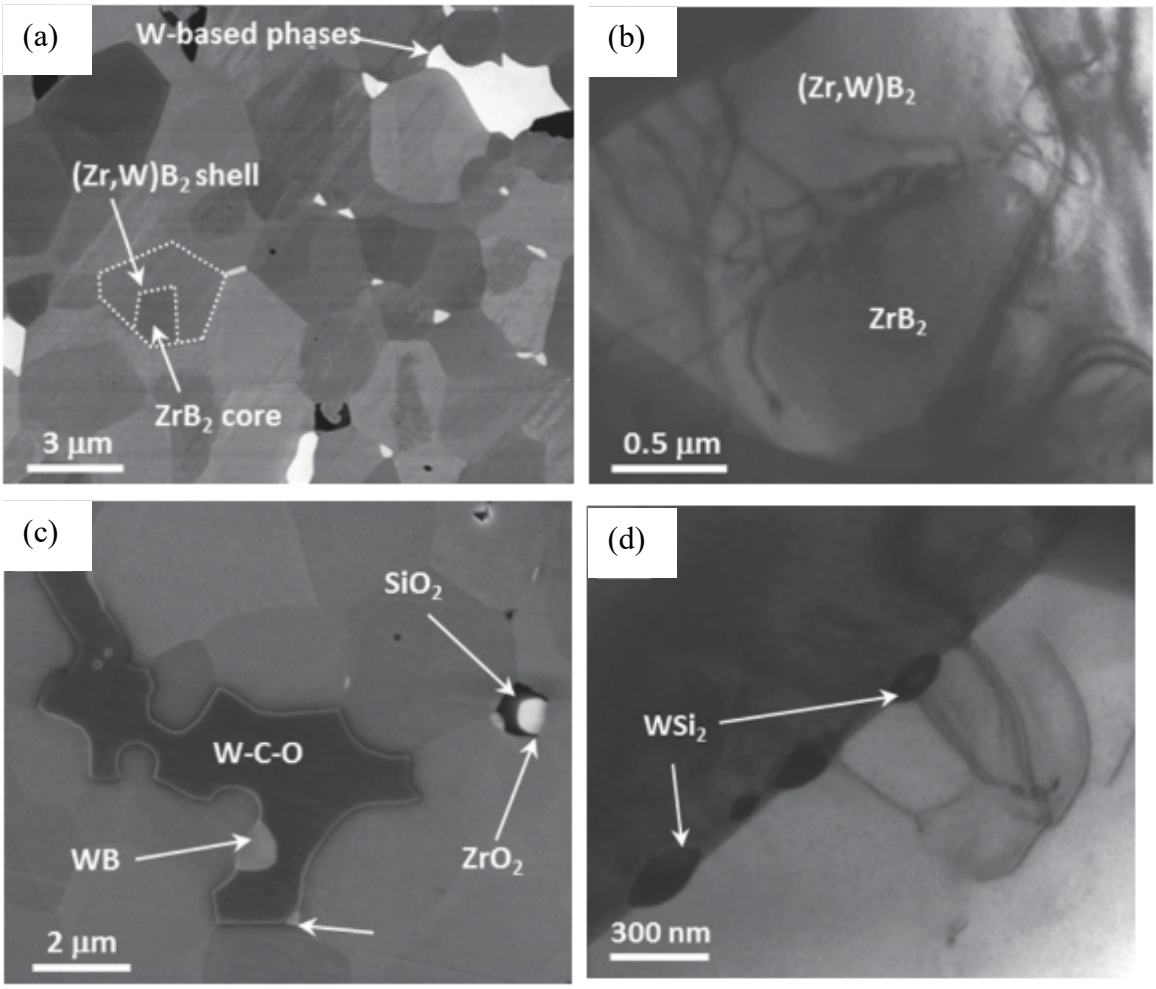

Figure 2.5 FESEM micrographs of hot-pressed (at 1930 °C, 40 MPa for 40 min) ZrB_2-15vol.% WSi_2 composite showing (a) core-rim structures of the composite, in this ZrB_2 as core surrounded by $(Zr,W)B_2$ shell and TEM image (b) showing the difference between core–shell structure at high magnification, (c) residual phases of W-C-O, WB, SiO_2 and ZrO_2, (d) remaining amount of WSi_2 at the grain boundaries [132].

It was reported that nitrides addition also enhances the densification of ZrB_2 since they eliminate the surface oxides on the boride powders as well due to the propensity of nitrides for oxygen. Monteverde and Bellosi found that addition of ≥2.5wt.% Si_3N_4 is beneficial towards achieving near theoretical sinter density at lower hot-pressing temperature of 1700 °C and in just 15 min [52]. The formation of liquid phase at the sintering temperature enhanced the densification since the liquid phase favors particle rearrangement and densification kinetics by partial dissolution of ZrB_2, bulk diffusion and reprecipitation. **Figure 2.6** shows the

microstructure of ZrB_2-5vol.% Si_3N_4 and ZrB_2-20SiC-4Si_3N_4 (vol.%) showing the low-density secondary phases (BN, BN-rich glassy phase) along with unreacted ZrO_2 in both the samples. The reduction of oxygen causes boron activity, grain boundary diffusion and promotes densification. The microstructure of ZrB_2-Si_3N_4 consists of ZrB_2, ZrO_2, BN, and borosilicate glass. These phases were present due the following sintering reaction [52], [84].

$$Si_3N_4 + 2B_2O_3 = 4BN + 3SiO_2 \qquad (18)$$

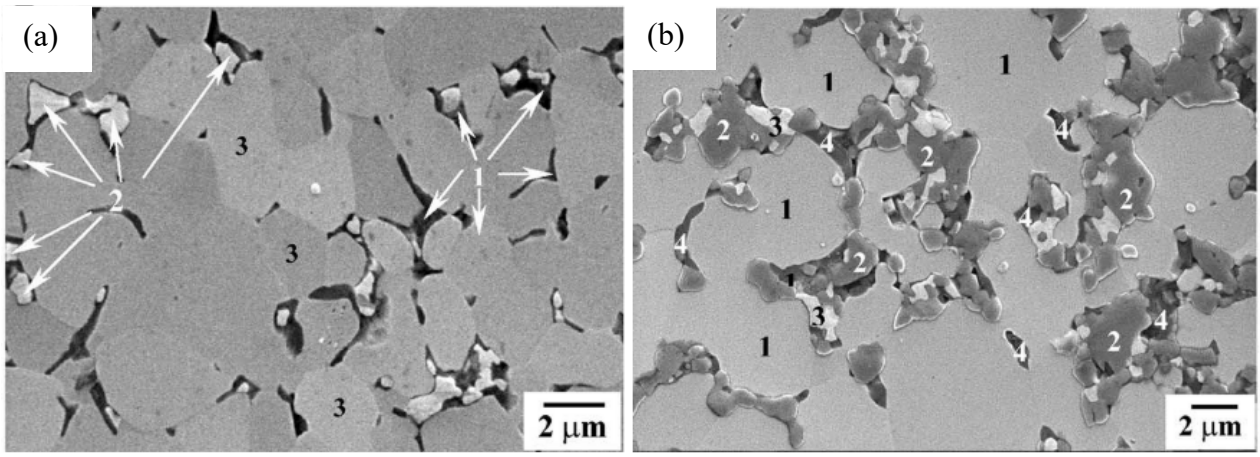

Figure 2.6 SEM micrograph of (a) ZrB_2-5vol.% Si_3N_4 after hot pressing at 1700 °C, 30 MPa for 15 min, showing the phases of (1) low density secondary phases (BN, BN-rich glassy phase) (2) ZrO_2 and (3) ZrB_2. (b) ZrB_2-20SiC-4Si_3N_4 (vol.%) after hot pressing at 1870 °C, 30 MPa for 10 min, showing the phases of (1) ZrB_2 (2) SiC (3) ZrO_2 and (4) low density secondary phases [84].

2.5 Mechanical properties of ZrB_2

Being structural materials, it is important that the basic mechanical properties of the UHTCs are also engineered as per requirement. Various aspects, right from processing and incorporation of sinter additives to phase evolution and microstructure development have considerable influence on these properties, necessitating careful optimization. This section will present a survey on the effects of the various parameters on the room temperature properties, highlighting some of the efforts that have demonstrated the possibilities of further improvement via careful optimizations. The effects of sintering additive contents/types (along with sinter

densities) on the mechanical properties of the various ZrB_2-based composites have been presented.

2.5.1 Hardness

Reported hardness values of polycrystalline ZrB_2 is 21–23 GPa [87]. The addition of SiC (H_V ~28 GPa [133]) to ZrB_2 resulted in a slight increase in hardness. On the other hand, $MoSi_2$ has a low hardness (~9 GPa [134]) and its addition decreased the hardness of ZrB_2-based ceramics [135]. Asl et al. [136] reported the dependence of hardness of ZrB_2-SiC composites on sintering density and volume fraction of SiC; as per the following relation

$$H_v = A.\ \exp(B.\rho) \qquad (19)$$

Where, H_V is the Vickers hardness (in GPa), A, B are constants for a fixed composition ($A = 4.53\exp(-0.07V_{SiC})$ and $B= 0.0009V_{SiC} + 0.009$) and ρ is the sinter density. Hence, the final simplified equation for the Vickers hardness as a function of ρ and vol.% of SiC (V_{SiC}) is:

$$H_v = 4.53\ \exp(0.009\rho-0.07V_{SiC}+0.0009\rho V_{SiC} \qquad (20)$$

The use of metallic sintering additives for improving sinter densities via liquid phase sintering and they may not improve hardness of ZrB_2 due to the presence of the softer metallic phase and more importantly they are more deleterious for the high temperature applications [26], [64], [137].

2.5.2. Fracture toughness and flexural strength

Transition metal diborides and other UHTCs possess superior hardness and modest fracture strength, however, their fracture toughness is considerably lower compared to the other materials classes. This drawback often renders the concerned diborides not suitable for usage in the bulk form for applications involving shock loading or impact, unless engineered for improving the fracture toughness. The lower fracture toughness makes it imperative to reduce the voids, flaws, porosities to the minimum possible levels and improve the surface finish. In general, the actual properties of ceramics in bulk polycrystalline form depend critically on the microstructural development and composition, which in turn depend on the processing route

[25], [138], [139]. The fracture toughness of ZrB_2 with and without additives, is generally in the range of 3.5–4.5 $MPam^{0.5}$. Improvements in fracture toughness by ~50% and flexural strength by ~90%, along with marginal improvements in hardness, have been reported for ZrB_2 upon reinforcement with SiC particulates [38], [118], [140]–[143]. Such improvements are usually correlated with better sintering densities and refined matrix grain sizes (especially for flexural strength [142], [144]). With respect to the other toughening mechanisms, few researchers also attributed crack bridging by SiC particles and the residual stresses due to mismatch in the CTE between the borides and SiC (tensile ~152 MPa in ZrB_2 and compressive ~452 MPa in SiC [140], [141]), while explaining the effects of SiC incorporation on the fracture toughness [145].

Recently, Paul et al. evaluated the fracture toughness of ZrB_2-20vol.% $MoSi_2$ composite with varying amounts of SiC_w (whiskers) [146]. It was observed that fracture toughness increased with increasing SiC_w amounts due to crack deflection and crack arrest. As far as the fracture toughness is concerned, large ZrB_2 grains and fine uniform distribution of SiC is preferred. Large ZrB_2 grains enhances elastic or frictional bridging, while the uniformly distributed fine SiC grains lead to frequent crack deflection and pull-outs; thus, contributes towards enhancing the fracture toughness of ZrB_2. In the case of ZrB_2-$MoSi_2$, the fracture toughness (2.9–4.0 $MPam^{0.5}$) was relatively low, with crack propagation along ZrB_2 boundaries and across $MoSi_2$ grains being observed [147].

Based on the more common ZrB_2-20vol.% SiC composite, Guo and Opeka had shown that the properties can still be further improved by minor additions of rare-earth oxides (up to 3vol.%) [14], [148]. The more important observation was that the type of the rare-earth oxides had notable influences on the mechanical properties for fairly similar densifications, with Y_2O_3 and Yb_2O_3 improving the fracture toughness considerably (by ~25%), along with marginal improvements in the hardness, as opposed to the rather slightly detrimental effects of La_2O_3 and Nd_2O_3. The effects were attributed to the types of grain boundary phases formed due to

sintering reactions (crystalline in case of Y_2O_3 and Yb_2O_3; while amorphous in the case of La_2O_3 and Nd_2O_3) and concomitantly exaggerated matrix grain growth in the presence of La_2O_3 and Nd_2O_3. This highlights the importance of phase evolution and microstructural development on the mechanical properties of UHTCs.

Table 2.1 Densification, microstructure and mechanical properties of ZrB_2 ceramic and its composites processed by different sintering techniques

Composition	**Sintering conditions (°C, min, MPa)**	**Phases**	**RD**	**GS (μm)**	**H (GPa)**	**FT ($MPam^{0.5}$)**	**Ref.**
ZrB_2-20vol.% SiC	PS, 2000, 120	ZrB_2, SiC	98	10	16.5	5.67	[149]
ZrB_2-10SiC-2C (wt.%)	PS, 2000, 180	ZrB_2, SiC, $ZrSi_2$, B_4C	99.6	-	32.5	15.7	[73]
ZrB_2-5vol.% B_4C	PS, 2300, 120	ZrB_2, B_4C	97.1	94.9	-	-	[75]
ZrB_2	HP, 2150, 60, 32	ZrB_2	97.3	33.4	14.1	3	[80]
ZrB_2-(0-30)vol.%SiC	HP, 1900, 45, 30	ZrB_2, SiC, WC	100	3-5	23-24	3.5-5.3	[87]
ZrB_2-10SiC-10ZrC (vol.%)	HP, 1900, 60, 30	ZrB_2, SiC, ZrC	100.2	2.87	17.7	4.6	[150]
ZrB_2-(15-30)vol.% SiC	HP, 2000, 30, 10	ZrB_2, SiC	98.3-99.8	-	14.9-21.3	3.5-4.7	[136]
ZrB_2-20vol.% SiC	HP, 1900, 60, 30	ZrB_2, SiC	97.4	-	19.82	3.68	[151]
ZrB_2-20SiC-10$MoSi_2$ (vol.%)	HP, 1900, 60, 30	ZrB_2, SiC, $MoSi_2$, ZrO_2	99.9	-	18.03	5.15	″
ZrB_2-20SiC-5C (vol.%)	HP, 1900, 60, 30	ZrB_2, SiC, ZrC	99.2	1-4	12.3	6.6	[152]

ZrB_2-20SiC_w-5Graphene (vol.%)	HP, 1950, 60, 30	ZrB_2, SiC, C	98.5	-	-	6.6	[153]
ZrB_2-20SiC-10Graphite (vol.%)	HP, 1900, 60, 30	ZrB_2, SiC, C	-	2	-	12.4	[154]
ZrB_2-25vol.%SiC-5wt.% Graphene	HP, 1850, 60, 20	ZrB_2, SiC, C	99.1	3.5	15.7	6.4	[155]
ZrB_2-20SiC-(5-10)$C_{spheres}$ (vol.%)	HP, 2000, 60, 30	ZrB_2, SiC, C	-	2.3-2.1	16.6-15.5	7.5-7.1	[156]
ZrB_2-20SiC-5AlN (vol.%)	HP, 2000, 60, 30	ZrB_2, SiC, AlN	100	-	19.4	5.35	[157]
ZrB_2-20SiC-6$TaSi_2$ (vol.%)	HP, 1900, 45, 30	ZrB_2, SiC, $ZrSi_2$, $TaSi_2$, ZrO_2, (Zr, Ta)B_2	100.1	1.38	18.54	5.71	[158]
ZrB_2-15vol.% $MoSi_2$	HP, 1750, 20, 30	ZrB_2, $MoSi_2$, ZrO_2, SiO_2	98	1.8	15	-	[128]
ZrB_2-15$MoSi_2$-2.3C (vol.%)	HP, 1780, 12, 30	ZrB_2, $MoSi_2$, ZrO_2, SiC	99	1.5	17	-	″
ZrB_2-15vol.% $TaSi_2$	HP, 1850, 10, 30	ZrB_2, $TaSi_2$, (Zr, Ta)B_2, ZrO_2	99	2	18	3.8	[124]
ZrB_2-25$ZrSi_2$-5WC (vol.%)	HP, 1450-1550, 30, 30	ZrB_2, $ZrSi_2$, WC, WB, ZrC, WSi_2	98.5-99.5	1-2.17	18.9-18.4	6.2-6.8	[159]
ZrB_2-40vol.% B_4C	HP, 1900, 30, 32	ZrB_2, B_4C, W, WC	99.8	2.1	21.4	5.3	[85]
ZrB_2-20vol.% SiC-0.2wt.% MWCNT	HP, 1900, 60, 30	ZrB_2, SiC, ZrO_2	94.4	-	15.5	4.6	[160]
ZrB_2-20SiC-10CNT (vol.%)	HP, 1850, 60, 20	ZrB_2, SiC	93.9	-	8.6	5.1	[161]
ZrB_2-(15-30)vol.% SiC	SPS, 1375, 5, 25	ZrB_2, SiC	93-94	3-10	10.5-11.1	-	[162]

ZrB_2-20wt.% SiC	SPS, 2000, 15, 50	ZrB_2, SiC	91.9	10	16.22	3.69	[163]
ZrB_2-(17-45)vol.% SiC	SPS, 1950, 15, 50	ZrB_2, SiC	-	2-7	-	2.5-2.9	[164]
ZrB_2-20SiC_w-20$MoSi_2$ (vol.%)	SPS, 1600, 10, 50	ZrB_2, SiC, $MoSi_2$	95	-	14	6.85	[146]
ZrB_2-37vol.% BN	SPS, 1700, 10, 60	ZrB_2, BN	>97	1.5	6.7	-	[165]
ZrB_2-15vol.% $MoSi_2$	SPS, 1750, 7, 30	ZrB_2, SiC, $MoSi_2$	98	1.4	16	4.4	[166]
ZrB_2-30ZrC-10SiC (vol.%)	SPS, 2100, 2, 30	ZrB_2, SiC, ZrC, ZrO_2	99	2	19	3.5	″
ZrB_2-10CNT-1mullite (wt.%)	SPS, 1350, 5, 30	ZrB_2, mullite	99.1	-	16.24	4.18	[167]
ZrB_2-6wt.% Cu	SPS, 1500, 15, 40	ZrB_2, Cu	94.8	-	19.1	7.4	[168]
ZrB_2-30SiC-8ZrC (vol.%)	SPS, 1800, 9, 30	ZrB_2, SiC, ZrC	93.4	6.1	-	-	[169]
ZrB_2-25vol.% SiC-4wt.% V	SPS, 1900, 7, 40	ZrB_2, SiC, ZrC, VB_2	-	-	22.9	4.5	[170]
ZrB_2-30SiC-8HfB_2 (vol.%)	SPS, 1800, 9, 30	ZrB_2, SiC, (Zr, Hf)B_2	92.3	3.4	17	7.3	[171][172]
ZrB_2-10vol.% SiC_w	SPS, 1550, 5, 40	ZrB_2, SiC	97	2-3	-	6.21	[173]
ZrB_2-10SiC_w-5AlN (vol.%)	SPS, 1550, 5, 40	ZrB_2, SiC, ZrN, BN, Al_2O_3	100	-	-	8.15	″
ZrB_2-10wt.% SiC	SPS, 2050, 10, 50	ZrB_2, SiC	98.7	2.0	17.3	4.47	[174]
ZrB_2-10wt.% B_4C	SPS, 2050, 10, 50	ZrB_2, B_4C	99.1	2.0	19.0	4.40	″
ZrB_2-10wt.% ZrC	SPS, 2050, 10, 50	ZrB_2, ZrC	99.7	3.5	14.7	5.26	″

ZrB_2-20VB_2-20ZrC (vol.%)	SPS, 1900, 7, 40	ZrB_2, VB_2, ZrC	99.1	4.1	19.2	4.5	[175]
Monolithic ZrB_2	SPS, 1900, 15, 70	ZrB_2	84.8	-	16.6	1.5	[176]
ZrB_2-2-6vol.% MWCNT	SPS, 1900, 15, 70	ZrB_2	95.3-99.3	-	14.1-16.3	1.5-3.5	″
ZrB_2-(10-40)vol.% SiC	SPS, 1900, 15, 70	ZrB_2, SiC	99.1-99.7	-	19.3-22.7	1.9-2.6	″
ZrB_2-20SiC-15MWCNT (vol.%)	SPS, 1600-1800, 10, 25	ZrB_2, SiC, C	94.6-99.1	1.5-3.4	11.5-16	5.9-8	[177]
ZrB_2-25vol.% SiC-5wt.% graphite	SPS, 1900, 7, 40	ZrB_2, SiC, C, ZrC	100.7	3.3	16.6	6.7	[178]

2.6 Oxidation studies of ZrB_2 ceramics

The most application of diborides involves the exposure to oxidation environment at high temperatures. The oxidation resistance of diborides is characterized by the oxidation products and the combination of physical and chemical changes taking place on the surface of the samples after oxidation. The oxidation behaviour of the diboride is evaluated as a function of temperature, partial pressure of oxygen, exposure time, porosity and composition [179]–[183]. **Table 2.2** shows the weight gain, oxide layer thickness and oxide phases formed during the oxidation of different ZrB_2-based composites.

Figure 2.7 shows the oxidation of ZrB_2 in three different temperature regimes and the formation of oxide products. This three temperature regimes are classified as low, intermediate and high temperature regimes [184]. When, the ZrB_2 exposed to air at elevated temperatures the following reaction will occur [14].

$$ZrB_2\,(s) + 2.5O_2\,(g) = ZrO_2\,(s) + B_2O_3\,(l) \qquad (21)$$

Oxidation of ZrB_2 starts at the temperature range of 500–550 °C, without any microstructural changes observed at the temperature up to 500 °C. After heating at temperature above 550 °C, the layer of B_2O_3 covered the surface of the sample, which protects the sample from further oxidation. In the temperature range of 650–800 °C, the oxidation of borides still follows the parabolic kinetics [185], [186]. At temperature less than 1000 °C, ZrO_2 and B_2O_3 forms a continuous layer that controls further diffusion of oxygen, due to passive behaviour of B_2O_3, which gives parabolic kinetics for weight gain and oxide layer thickness [14], [24].

In the temperature range of 1000-1400 °C ZrB_2 ceramics shows para-linear kinetics because of combination of weight gain due to ZrO_2 and liquid B_2O_3 formation and weight loss due to evaporation of liquid B_2O_3. As liquid boria evaporates, a porous zirconia left, although it has small amount of boria may be retained [187].

$$B_2O_3\,(l) = B_2O_3\,(g) \text{ at } 1100\ ^\circ C \qquad (22)$$

In the intermediate temperature region, the cross-sectional of oxidized sample reveals the two layer oxide scale, which consists of outer glassy B_2O_3 layer and inner layer that consists of porous ZrO_2 filled by glassy B_2O_3. In this temperature regime, para-linear kinetics have been observed which is due to vaporization and formation of B_2O_3. In between 1100-1400 °C range, the overall weight change is a combination of weight gain due to oxidation and vaporization of B_2O_3 [188]–[190]. As the temperature increases from 1000 °C to higher temperatures ZrO_2 microstructure changes from equiaxed grains to columnar grains. In this temperature range, ZrO_2 phase changes from monoclinic to tetragonal, which effect a change in the porosity of the oxide scale. With increasing temperature, the transformation results in volumetric shrinkage. The m-ZrO_2 nucleates and grows during transient heat up to transformation temperature and after that it transforms to tetragonal structure, shrinkage in the layer and the gap between ZrO_2 grains increases. Thus, the increase in porosity of oxide scale at transformation temperature, and that this high amount of porosity retained during further oxidation [191].

In high temperature regime above 1400 °C, the linear weight gain kinetics have been observed and the oxide layer is no longer protective. Because the rate of B_2O_3 vaporization is more compared to rate of B_2O_3 formation during oxidation [185]. At oxidation temperature more than 1800 °C, the rate of B_2O_3 evaporation is more than rate of formation of B_2O_3, results in the porous ZrO_2 layer formation [191]. As porous ZrO_2 does not act as barrier for diffusion of oxygen, the oxidation resistance of diborides deaccelerated not only by the evaporation of boria layer but also by the crack penetration in this temperature range [192]. **Figure 2.7** shows that as the B_2O_3 is completely evaporated and forms porous ZrO_2, which gives chances for rapid oxidation of ZrB_2.

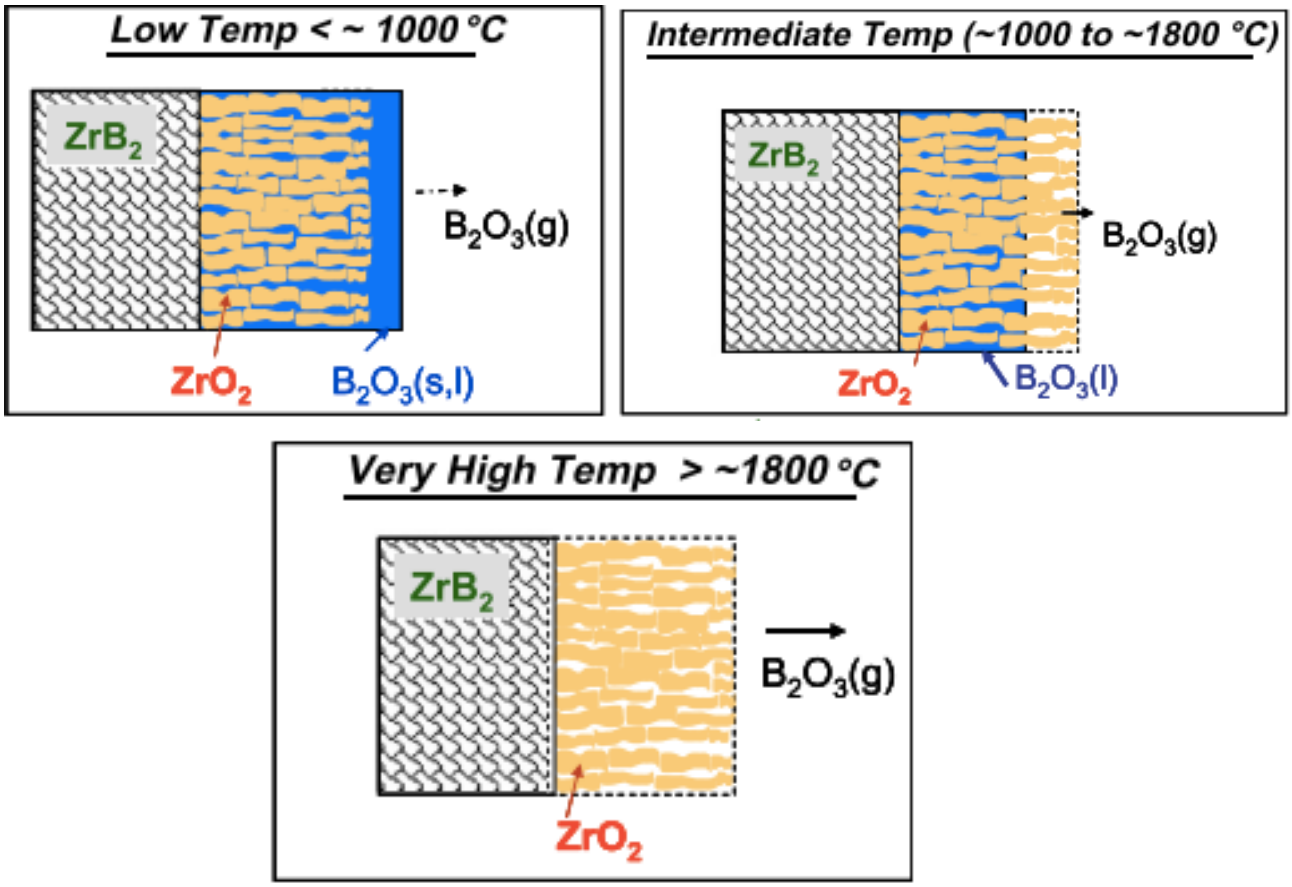

Figure 2.7 The oxidation of ZrB_2 in three different temperature regimes and the formation of oxide products [184].

In addition to experimental results, the oxidation resistance of borides has been described using different thermodynamic models [184], [193]. The oxidation resistance of the diborides are evaluated by using weight gain, oxide layer thickness and different phases formed

during oxidation are shown in **Table 2.2** [130], [151], [194]–[218]. For monolithic ZrB_2, the weight gain of 14.9 mg/cm^2 and oxide layer thickness of 150 μm was evident after oxidation at 1500 °C for 3 h [219]. On the other hand, the weight gain of 8.8 mg/cm^2 and oxide layer thickness of 248 μm was evident after oxidation at 1400 °C for 1 h [220]. Overall, single phase ZrB_2 show poor oxidation resistance at elevated temperatures. Hence, ZrB_2 alone can't withstand high temperature atmospheric condition. So, to improve the oxidation resistance of ZrB_2 the composition of oxide layers must be altered and it can be performed by adding reinforcement in the matrix. A number of different additives (in particular silicon based compounds/ceramics) have been attempted to enhance the oxidation resistance of diborides.

One of the widely used approach was observed to be the reinforcing SiC as secondary phase, which limits the oxide layer thickness across a wide range of temperature when comparted to monolithic diborides [30], [221]. The oxidation resistance could be improved due to the formation of a stable and passive borosilicate glass layer and thin layer of SiO_2 on ZrB_2 ceramics. These layers are characterized to be more stable at high temperatures as compared to boria layer. The weight gain measurements of SiC reinforced ZrB_2 at temperature less than 1100 °C is not affected by the SiC additions. The oxide scale of diborides at these temperature levels confirms that diborides oxidized preferentially, which forms B_2O_3 and ZrO_2 oxide scales, and leaves the unoxidized SiC [222]. On the other hand, at temperature above 1100 °C, evaporation of B_2O_3 becomes significant and SiC oxidation is inevitable. In this temperature range, borosilicate glassy layer forms and it gives parabolic weight gain kinetics [223], [224]. The borosilicate glass fills the pores formed during oxidation and also it forms passive glassy external layer on the surface of the sample. Hence, the SiC addition helps to form stable passive layer, which is responsible for inhibiting further diffusion of oxygen towards unoxidized composite [225]. The oxygen diffusion coefficient of SiO_2 is 10^{-21} m^2/s at 1550 °C, while for ZrO_2 is 10^{-10} m^2/s at 1500 °C [220]. During furnace oxidation in static air, a continuous passive

layer is formed, but at high temperature conditions, the glassy layer flows which is due to decrease in viscosity, which gives the scattering in experimental results.

Figure 2.8 shows the cross-sectional microstructural changes of ZrB_2-SiC composite as a function of oxidation temperature. At temperature 1000 °C for 30 min, the composite forms top thin B_2O_3 layer (2 μm), intermediate ZrO_2 layer with unoxidized SiC (~6 μm) and unaffected ZrB_2-SiC [186], [226] (shown in **Figure 2.8(a)**). The oxidation of SiC is much slower compared to ZrB_2 matrix at this temperature conditions, because of that in an intermediate layer SiC particles were present in ZrO_2 layer. Due to passive oxidation behaviour of top B_2O_3 layer, it characterized with parabolic weight gain kinetics. As the oxidation temperature for ZrB_2-SiC increases to 1200 °C, the composition and structure of the cross-sectional surface is altered. In the temperature range of 1200-1400 °C, B_2O_3 is started evaporating and SiC oxidation takes place.

$$SiC + 1.5O_2 = SiO_2\ (l) + CO\ (g) \qquad (23)$$

At oxidation temperature of 1200 °C for 30 min, ZrB_2-SiC forms continuous SiO_2 layer above the porous ZrO_2 layer (shown in **Figure 2.8(b)**). A thin layer of SiO_2 protects the underlying surface of the sample by providing inhibition to the diffusion of oxygen with parabolic weight gain kinetics. The passive SiO_2 layer have some amount of B_2O_3, which is due to incomplete evaporation of B_2O_3 or the continuous production of B_2O_3 from underlying surface of the sample. At 1400 °C, the vapor pressure of B_2O_3 increases extensively, causes to its rapid evaporation. When B_2O_3 is evaporating, it is not replaced as in the case of monolithic diboride oxidation, the efficiency of the passive barrier is deteriorated since the porous ZrO_2 layer alone does not protect the underneath ZrB_2 from further oxidation. The addition of SiC to ZrB_2 helps to improve the oxidation resistance at high temperatures by forming a borosilicate glass layer on oxidized surfaces, which gives the parabolic weight gain kinetics. The SiO_2 layer and underneath SiO_2-ZrO_2 layer thickness was not uniform over the cross-sectional surface of the sample at 1400 °C (shown in **Figure 2.8(c)**). This is due to local variation in composition,

surface cracks and topology, which enhances the local oxidation resistance. The cross-sectional morphology of ZrB_2-SiC at oxidation temperature of 1500 °C was similar to the structure observed at 1400 °C, but at 1500 °C the oxide layers were thick and uniform (shown in **Figure 2.8 (d)**). The layered structure consisted of (1) SiO_2 layer, (2) a thin layer of ZrO_2-SiO_2, (3) ZrB_2-ZrO_2 layer, it also considered as SiC depleted layer (4) unreacted ZrB_2-SiC layer. This similar layered structure is also observed in other works during the oxidation of ZrB_2-SiC [223], [227]–[229]. The SiC depleted layer forms under the SiO_2 rich scale and it contains unreacted diboride and some amount of retained SiC. Under some other conditions, a layer of ZrO_2 and/or amorphous SiO_2 (l) was observed between the outer glassy layer and SiC depleted layer [230], [231]. Generally, the SiC depleted layer was a porous structure due to the evaporation of SiO_2, due to this spallation and delamination of the oxide scale [231]. The SiC depleted layer was formed due to following chemical reactions [222].

$$SiC + O_2\,(g) = SiO\,(g) + CO\,(g) \qquad (24)$$

$$SiO_2\,(l) = SiO\,(g) + 0.5O_2\,(g) \qquad (25)$$

$$SiO\,(g) + 0.5O_2\,(g) = SiO_2\,(l) \qquad (26)$$

ZrB_2-SiC composites continued to perform protective nature in these extreme experimental conditions. The SiC phase was withdrawn from diboride matrix as a gaseous phase according to Reaction (24) and (25). In addition, the formation and decomposition of SiO_2 was observed from Reaction (26). In SiC depleted layer, neither SiO_2 nor other condensed phases were reportedly observed. The preferential oxidation of SiC was happened due to decrease in oxygen partial pressure and increase in oxidation temperature [232]–[234].

Figure 2.9 shows the reaction sequence for the formation of SiC depleted region (from top to down). **Figure 2.9(a)** shows unoxidized ZrB_2 and SiC in ZrB_2-30vol.% SiC composite. When the composite was exposed to initial heating, ZrB_2 oxidizes to form ZrO_2 and B_2O_3 at temperature below 1200 °C. Kinetically, the oxidation of ZrB_2 is more compared to SiC in this temperature regime [222], [226] (**Figure 2.9(b)**). At temperature below 1200 °C, the top layer

consists of B_2O_3 (l) with ZrO_2 and unreacted SiC (**Figure 2.9(b)**). This continuous layer protects the ZrB_2 from further oxidation. In this temperature range, the SiC phase was not oxidized significantly and it is not changed by incorporation in to the oxide layer. As the temperature reaches to 1500 °C, B_2O_3 evaporates due to high vapor pressure and SiC oxidizes to form SiO_2 (l). The ZrO_2 forms near the unreacted ZrB_2-SiC bulk and results in the formation of ZrO_2-SiO_2 layer (**Figure 2.9(c)**). This layer contains some amount of residual boron in the form of B_2O_3, which is dissolved in SiO_2 (l) in top ZrO_2-SiO_2 layer. The passive layer of SiO_2 forms on the top of the composite after oxidation at 1500 °C. The ZrO_2-SiO_2 layer is present between the outer rich SiO_2 (l) layer and the SiC-depleted layer (**Figure 2.9(d)**). The ZrO_2-SiO_2 layer thickness increased relatively by arc heater testing [185], [235], but in static oxidation, this layer remains to be thin compared to outer SiO_2 (l) and SiC-depleted layer. For the growth of SiO_2 (l) layer, silicon must be transported from unreacted layer to oxide layer through the SiC-depleted layer. When the SiC reacts with SiO_2 (l) it forms SiO (g) which is the reason for the formation of SiC-depleted layer.

$$SiC + 2SiO_2\ (l) = 3SiO\ (g) + CO\ (g) \qquad (27)$$

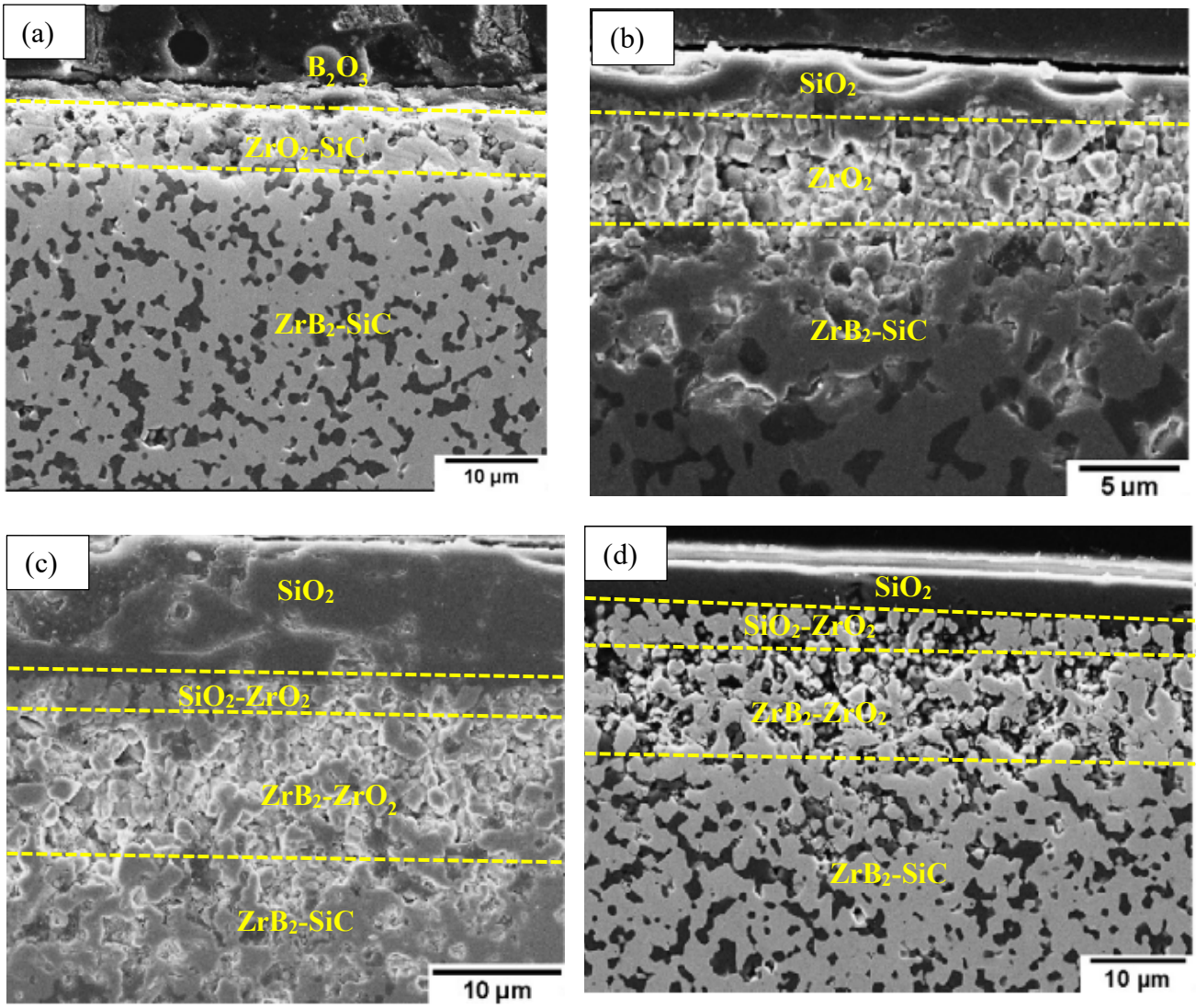

Figure 2.8 Cross-sectional morphology of ZrB_2-30vol.% SiC after oxidation in air at (a) 1000 °C, (b) 1200 °C, (c) 1400 °C and (d) 1500 °C for 30 min. At temperature below 1000 °C, B_2O_3 act as passive layer and at temperature above 1000 °C boria got evaporated and silica acted as passive layer [193], [225], [236].

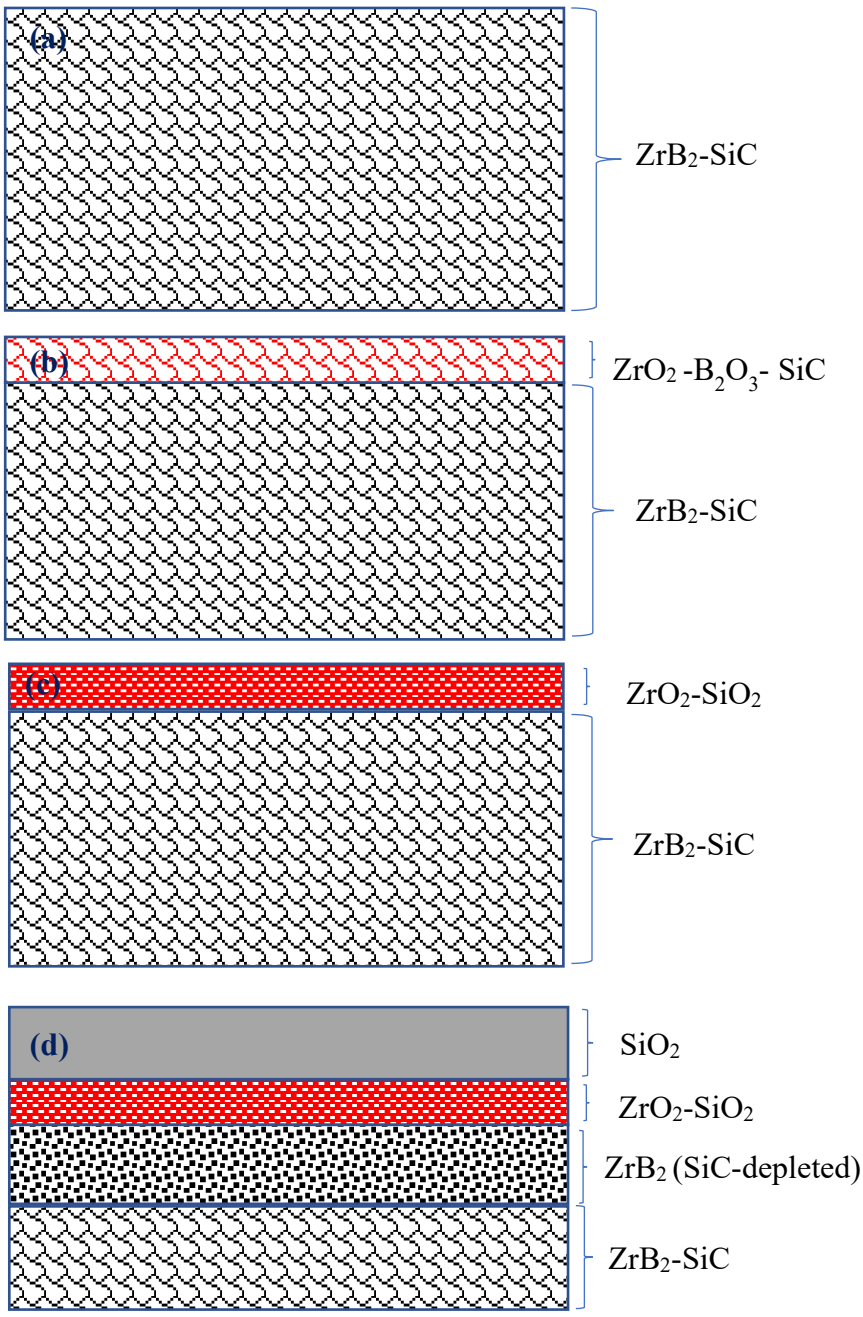

Figure 2.9 The diagram represents reaction sequence for the formation of the layer of SiC-depletion during the oxidation of ZrB_2-SiC at 1500 °C in air [237]. The sequence follows (from top to down) that is, (a) unaffected ZrB_2-SiC, (b) preliminary response during oxidation (c) cross-sectional morphology when the oxidation temperature reaches to 1500 °C and (d) during steady state holding at 1500 °C.

During isothermal oxidation at 1500 °C, SiO (g) was transported across the SiC -depleted region due to chemical potential gradient. The partial pressure of oxygen is constant across the SiC-depleted region and the concentration of some other species drives SiO (g)

transport. The formation of SiC-depleted region depends on the oxygen diffusion through top SiO_2 layer and the ZrO_2–SiO_2 layer. Based on this discussion, the thickness of the passive SiO_2 (l) layer should increase continuously with increasing time due to continuous oxidation of SiC, which increases the thickness of SiC-depleted layer in ZrB_2-SiC bulk [237].

Inoue et al. observed the SiC depleted layer in ZrB_2 based composites at 2000 °C for 10 s with varying amounts of SiC (**Figure 2.10**) [208]. **Figure 2.10(a)** shows the cross-sectional morphology of monolithic ZrB_2 after oxidation, it is observed that grain size of ZrB_2 under the ZrO_2 oxide layer was larger than that of the as sintered sample, because sintering of ZrB_2 starts in the temperature range of ~2000–2150 °C [66], [76]. The ZrB_2-SiC (ZS) composites form the layered structures comprising of top ZrO_2 layer and intermediate porous SiC-depleted layer and bottom unreacted bulk. In SiC depleted layer, the grains are larger compared to the unreacted bulk, also the grains are interconnected and pores are nucleated between the large particles. From **Figure 2.10**, it can be observed that the morphology of ZrO_2 layers is similar in all ZS composites. The thickness of ZrO_2 and SiC depleted layer for ZS20 is lower among the other samples. The porosity in SiC depleted layer was increased with increasing amount of SiC, as the more amount of SiC particles are consumed in SiC depleted layer. The thickness of SiC depleted layer decreased with increasing SiC amount in ZS composites. It is mainly because of the increased SiC amount that decreases the oxygen diffusion in unoxidized region. Inoue et al. observed that at 2000 °C with holding time less than 10 s, a SiC-depleted layer formed due to oxygen partial pressure in the air environment which was not enough to form SiO_2 by the oxidation of SiC. However, further increased addition of 20vol.% SiC showed high oxidation resistance of ZrB_2 [208].

The increase in amount of SiC accelerates the creep mechanism, due to high amounts of interfacial glassy phase that boosts the grain boundary sliding and forms cavities at particle-matrix boundaries [238], [239] and researchers suggested that ZrB_2-20vol.% SiC is the optimum composition to improve the properties. Recently, researchers tried different methods

to further improve the oxidation resistance of ZrB_2 ceramics at extreme high temperature conditions. The oxidation behavior of ZrB_2 composites was reportedly improved with the addition of different transition metal disilicides (which shows the combined effect of SiC and transition metallic addition).

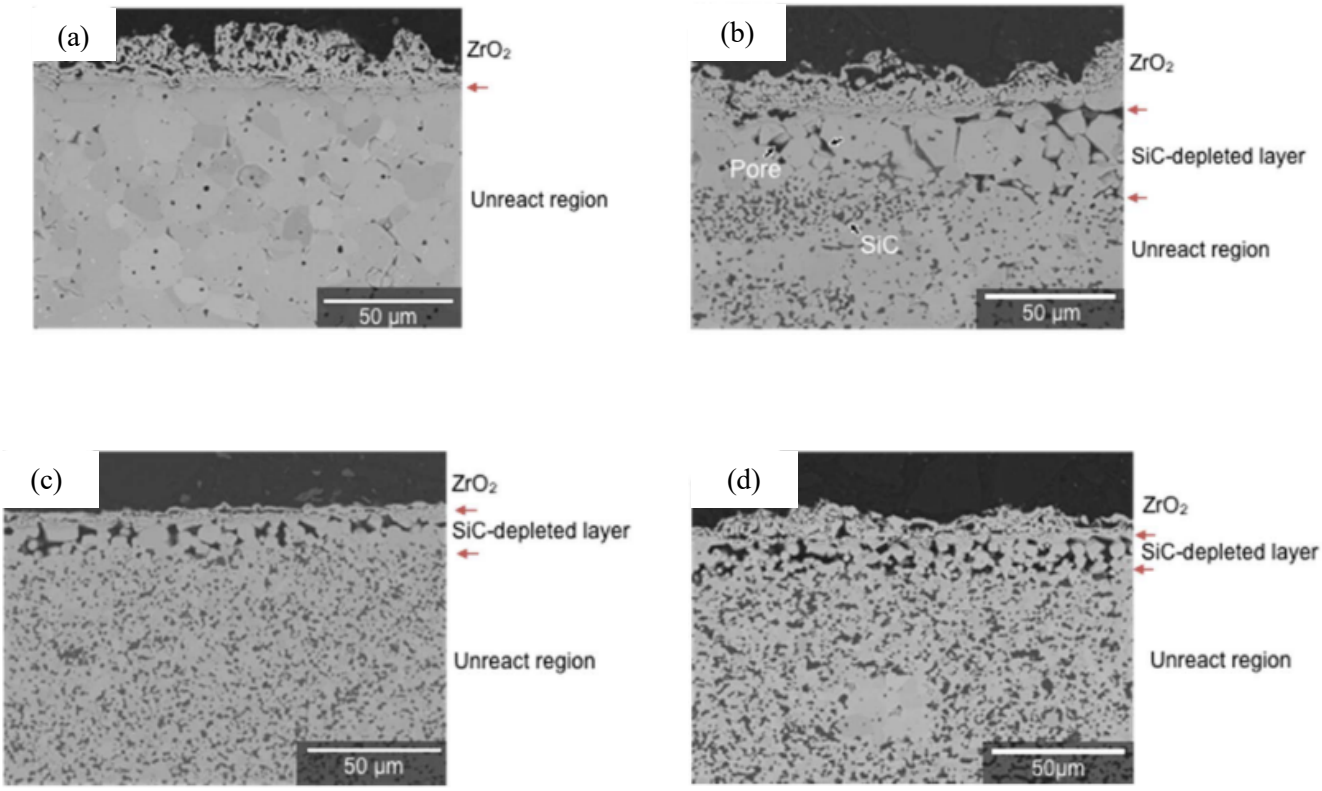

Figure 2.10 Cross-sectional morphology of (a) ZrB_2, (b) ZrB_2-10vol.% SiC (ZS10), (c) ZrB_2-20vol.% SiC (ZS20) and (d) ZrB_2-30vol.% SiC (ZS30) after oxidation at 2000 °C for 10 s [208].

The addition of disilicides helps to improve the densification, oxidation and high temperature mechanical properties of diborides. For example, the addition of $ZrSi_2$ improved the oxidation resistance of ZrB_2 at 1200 °C, it is further improved by the addition of $MoSi_2$ and WSi_2 [240]. The oxidation behavior of ZrB_2-20vol.% $MoSi_2$ was studied in air (at 700-1400 °C). The oxidation resistance of the composite was significantly improved by the addition of $MoSi_2$, because SiO_2 scale was formed on the surface, which inhibits the oxygen diffusion. The oxide layer consists of SiO_2, ZrO_2, $ZrSiO_4$, MoO_2 and MoB. The top surface layer of oxidized composite consists of SiO_2 rich glassy layer, a subsurface oxide layer and SiO_2, ZrO_2 and MoB containing mixture layer, depending on the oxidation temperature [130], [241]. Similar

oxidation species were observed in the same composite through thermogravimetric analysis (TGA) up to 1400 °C temperature for 30 h, which reveals the parabolic weight gain kinetics at 1400 °C, because of the formation of silica-based glass and refractory phases containing subsurface oxide layer formation [240], [242]. At temperature more than 1400 °C, the composite forms condensed stable phases in the oxide subsurface layer, such as MoB and Mo_5Si_3 phases, which are formed by following reactions [241], [243], [244]

$$ZrB_2 + 5MoSi_2 + 9.5O_2 = ZrO_2 + 7SiO_2 + Mo_5Si_3 + B_2O_3 \quad (28)$$

$$2MoSi_2 + B_2O_3 + 2.5O_2 = 4SiO_2 + 2MoB \quad (29)$$

The addition of disilicides helps to control the evolution of columnar ZrO_2 grains in the subsurface, which is unfavorable for the oxygen diffusion through the inward of matrix phase [240], [241]. **Figure 2.11(a)** shows the cross-sectional morphology of ZrB_2-15vol.% $MoSi_2$ after oxidation at 1650 °C for 15 min. The three-layered architecture shows the top layer of glassy SiO_2 with droplet shaped ZrO_2 with dispersed Mo/B particles. In intermediate layer, the accumulation of MoB phase was observed in the glassy SiO_2, underneath this layer unreacted bulk was observed [244]. As the oxidation temperature increased to 1800 °C, columnar ZrO_2 grains were formed, which gives the chance to the boiling of glasses. However, the top passive SiO_2 scale controlled the extreme weight loss. But at this condition, B_2O_3 preferably oxidized to form stable phase of MoB (Reaction (29)). The MoB phase was observed at the interface between outer SiO_2 scale and columnar ZrO_2. Due to low oxygen partial pressures, MoB starts to oxidize and forms MoO_3 phase by the following reaction.

$$2MoB + 4.5O_2 = 2MoO_3 + B_2O_3 \quad (30)$$

Then the glass layer viscosity reduces and due to this ZrO_2 pillars were developed. But as long as P_{O2} increases, MoB re-condenses again and forms high viscous boron containing SiO_2 glass on the top [240]. Silvestroni et al. observed the sintering temperature (1900 and 2150 °C) effect on cyclic oxidation resistance of ZrB_2-15vol.% $MoSi_2$ composite at 1650 °C for 15 min [245]. At higher sintering temperature, oxidation resistance was high in the composite due to higher

amount of SiC, which provides passive outer SiO_2-glassy layer. Further, MoB and volatile MoO_3 phases were formed at temperature of 1900 °C and it caused the bubble bursting phenomenon and reduced the oxidation resistance. At 2150 °C, grain growth and oxygen diffusivity along the grain boundaries reduced borosilicate glassy layer. Hence, the sintering conditions also plays a role in improving oxidation resistance, but the literature is limited in this concept.

The addition of WSi_2 to ZrB_2 helps to improve the oxidation resistance by forming SiO_2 layer at oxidation temperature of 1200-1350 °C, the chemical reactions are shown below:

$$WSi_2 + 3.5O_2\,(g) = WO_3 + 2SiO_2 \qquad (31)$$

$$(Zr,W)B_2 + O_2\,(g) = ZrO_2 + WO_3 \qquad (32)$$

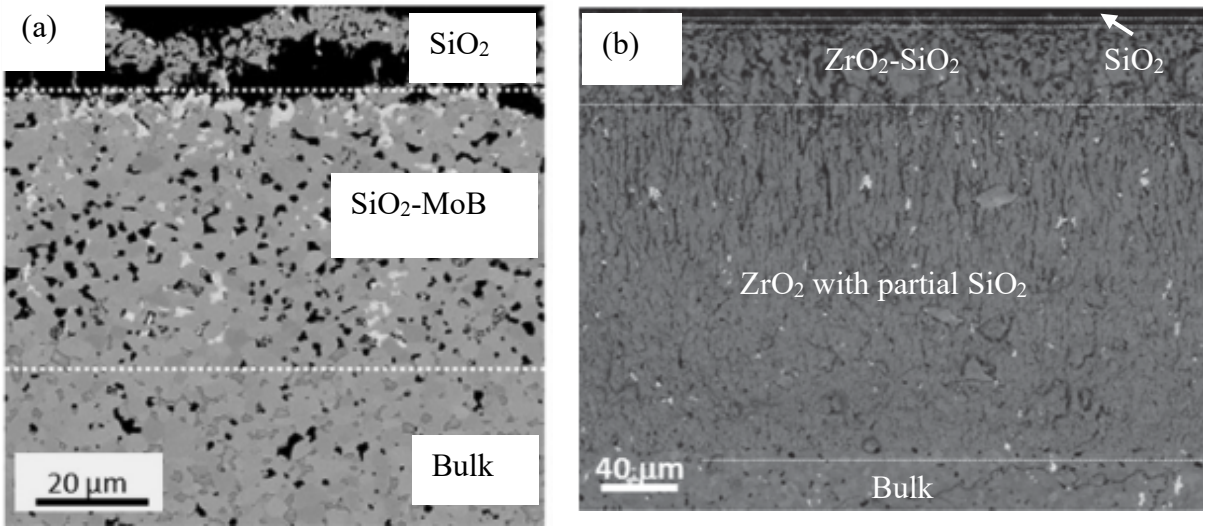

Figure 2.11 Cross-sectional morphology of (a) ZrB_2-15vol.% $MoSi_2$ [244] (b) ZrB_2-15vol.% WSi_2 [132] after oxidation at 1650 °C for 15 min.

During the oxidation at 1275 °C a eutectic phase was formed between WO_3 and ZrO_2 that decreases the porosity of the outer oxide scale by liquid phase sintering. The added W in the borate glass improves its stability [219], [246], [247]. Silvestroni et al. reported the oxidation behavior of ZrB_2-15vol.% WSi_2 at 1650 °C for 15 min [132]. After oxidation, the distinct layered cross-sectional structure was observed: (1) the top SiO_2 glass layer, (2) coarse rounded ZrO_2 with SiO_2, (3) a columnar ZrO_2 and (4) unreacted bulk (shown in **Figure 2.11**

(b)). W and WO_3 whiskers were observed in SiO_2 glass and identified across the oxide layer at different depths, depending on the P_{O2}. The WO_3 phase does not offer oxidation resistance to ZrB_2 ceramics. The presence of small amounts of WB, which have high oxidation resistance compared to that of ZrB_2 and WSi_2, which helps to form passive borosilicate glass. Even though it has less oxidation resistance compared to that of $MoSi_2$ containing diborides.

The addition of $TaSi_2$ to ZrB_2 helps to form top SiO_2 layer with small ZrO_2 particles at oxidation temperature of 1200 and 1350 °C. The SiO_2 formed by following reaction:

$$TaSi_2 + 6.5O_2\ (g) = Ta_2O_5 + 4SiO_2\ (l) \quad (33)$$

Furthermore, at oxidation temperature of 1500 °C for ZrB_2-$TaSi_2$, the following reactions were reported.

$$TaSi_2 + B_2O_3\ (l) + 0.5O_2\ (g) = TaB_2 + 2SiO_2\ (l) \quad (34)$$

$$(Zr,Ta)B_2 + O_2\ (g) = TaZr_{2.75}O_8 \quad (35)$$

$$2.75ZrO_2 + 0.5Ta_2O_5 = TaZr_{2.75}O_8 \quad (36)$$

The formation of solid solution $(Zr,Ta)B_2$ phase in sintered composite is useful for improving the oxidation resistance of the composite at 1500 °C. At this temperature the multilayer structure was observed which comprises of $TaZr_{2.75}O_8$ platelets in topmost SiO_2-glass, then a coarse ZrO_2 layer with incompletely filled glass and enclosing TaB_2 grains [248]–[250]. At temperature above 1650 °C, the oxide layer forms and it contains Zr, Ta and Si and a liquid phase. The $TaZr_{2.75}O_8$ phase in oxide layer allows oxygen diffusion of Ta_2O_5, along with other phases such as SiO (g) and B_2O_3 (g) evaporation. **Figure 2.12(a)** shows cross-sectional SEM image of ZrB_2-15vol.% $TaSi_2$ after oxidation at 1650 °C for 15 min which consists of layer-I: SiO_2-$TaZr_{2.75}O_8$-Ta_2O_5-ZrO_2, layer-II: SiO_2-Ta_2O_5-ZrO_2, layer-III and layer-IV consists of ZrO_2-TaB_2 and beneath unreacted bulk.

The total thickness of layer-I and layer-II consists of 500 μm, the external surface is composed of Ta-Zr-O partially filled with SiO_2, the bubbles and voids are observed over the entire thickness. The layer-II is partially delaminated from underneath layer-III. **Figure 2.12(b)**

shows TEM image of orthorhombic $TaZr_{2.75}O_8$ crystal within the glass. **Figure 2.12(c)** shows that TaB_2 grains embedded among ZrO_2 grains within the glassy layer of layer-III. ZrO_2 grains characterized by defective structure which is due to dislocations, twinning and stacking faults as a result of the tetragonal to monoclinic transformation (**Figure 2.12(d)**). **Figure 2.12(e)** shows the core-shell structure in TaB_2 particulate in layer-IV.

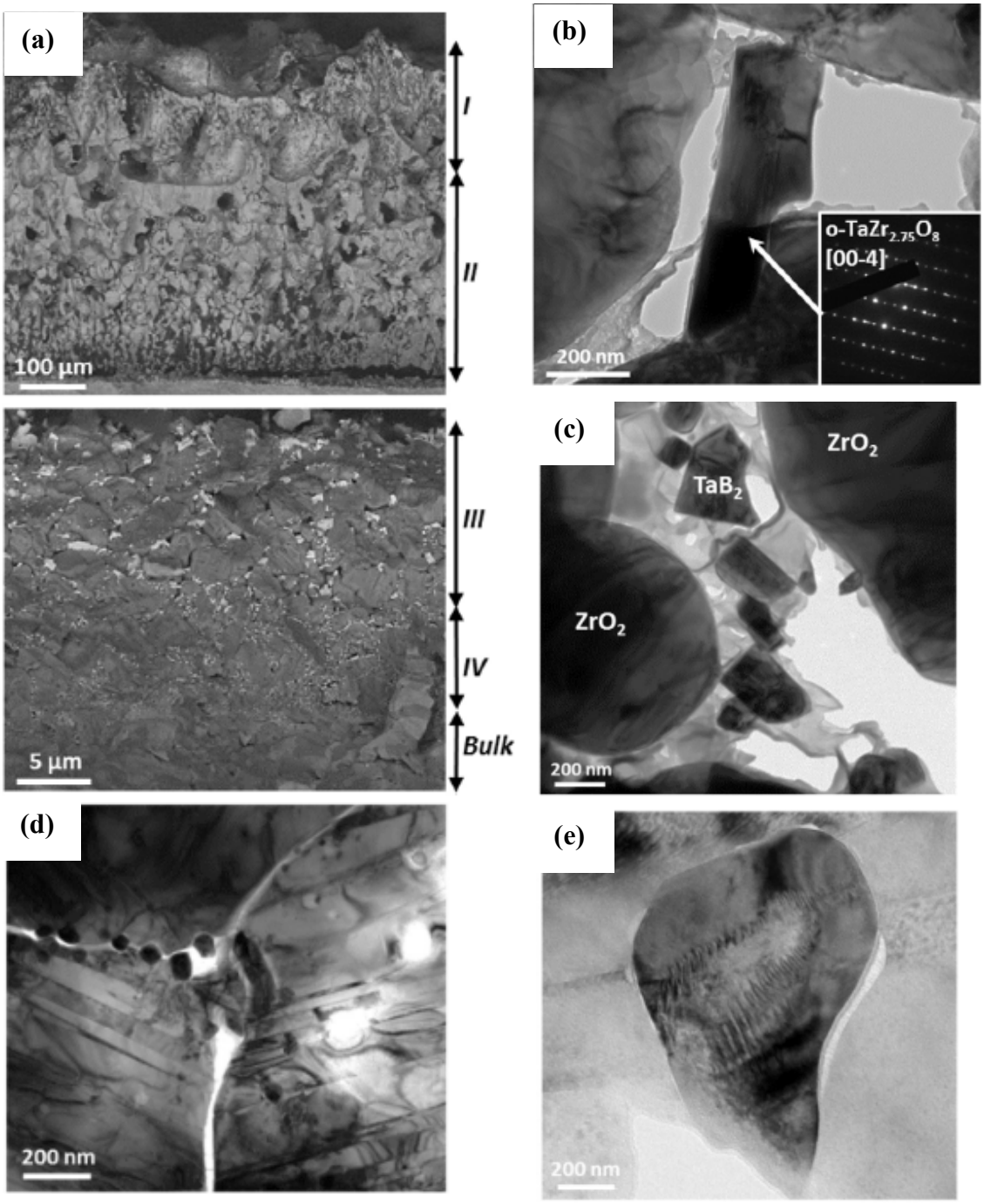

Figure 2.12 Cross-sectional SEM image of (a) ZrB_2-15vol.% $TaSi_2$ after oxidation at 1650 °C for 15 min which consists of layer-I: SiO_2-$TaZr_{2.75}O_8$-Ta_2O_5-ZrO_2, layer-II: SiO_2-Ta_2O_5-ZrO_2,

layer-III and layer-IV consists of ZrO_2-TaB_2, (b) TEM images of $TaZr_{2.75}O_8$ crystals embedded in glass with electron diffraction patterns in layer-I (c) TaB_2 grains embedded in glass among ZrO_2 grains in layer-III, (d) showing defective structure in ZrO_2 in layer-IV and (e) core-shell structure in the TaB_2 particulates in layer-IV [251].

Table 2.2 The oxidation of different ZrB_2-based composites evaluated by using weight gain and oxide layer thickness formed during oxidation

Composition	**Oxidation conditions (°C, h)**	**Weight gain (mg/cm^2)**	**Oxide layer thickness (μm)**	**Oxide phases**	**Ref**
ZrB_2-(10-30)vol.% SiC	1500, 10	16.4-5.9	55-18	ZrO_2, SiO_2	[252]
ZrB_2-(10-30)vol.% SiC	1900, 1	-	1100-800	ZrO_2, SiO_2	[206]
ZrB_2-15vol.% SiC	1700, 0.25	-	102	ZrO_2, SiO_2	[253]
ZrB_2-20vol.% SiC	2000, 10 sec	-	8.5	ZrO_2	[208]
ZrB_2-(20-40)vol.% SiC	1500, 10 ($P_{O2}=10^{-8}$ Pa)	-	122-172	ZrO_2	[254]
ZrB_2-(20-30)vol.% SiC	1800, 1 ($P_{O2}=20.26\times10^3$ Pa)	-	300-192	ZrO_2, SiO_2	[209]
ZrB_2-(20-30)vol.% SiC	1800, 1 ($P_{O2}=20.26$ Pa)	-	310-380	ZrO_2, SiO_2	″
ZrB_2-20vol.% SiC	2200, 0.5	-	776	ZrO_2	[210]
ZrB_2-20vol.% SiC	2200, 20 sec in Argon+H_2O	-	291	ZrO_2, SiO_2	[255]
ZrB_2-20vol.% SiC	1600, 10 (P_{O2}=200Pa)	-	172	ZrO_2	[211]
ZrB_2-20vol.% SiC	1700, 5	16.5	230	ZrO_2	[256]
ZrB_2-20vol.% SiC-3wt.% VC	1300, 100	26.937	520	SiO_2, ZrO_2, $ZrSiO_4$, ZrV_2O_7	[204]
ZrB_2-20vol.% SiC-5wt.% VC	1300, 100	15.951	275	“	“
ZrB_2-20vol.% SiC-7wt.% VC	1300, 100	17.859	350	“	“
ZrB_2-20vol.% SiC	1627, 1.66	4.3	53	ZrO_2, SiO_2	[257]
ZrB_2-20SiC-20$TaSi_2$	1627, 1.66	0.8	6	ZrO_2, SiO_2, Ta(C, B)	″
ZrB_2-20vol.% SiC	1800, 0.5	3.06	96	ZrO_2	[151]
ZrB_2-20SiC-10$MoSi_2$ (vol.%)	1800, 0.5	3.6	85	ZrO_2, MoB	″
ZrB_2-20wt.% SiC	1500, 1	-	28	ZrO_2, SiO_2	[212]
ZrB_2-20SiC-8Y_2O_3 (wt.%)	1500, 1	-	123	ZrO_2, SiO_2	″
ZrB_2-20vol.% SiC	2000, 5-10 sec	-	21	ZrO_2	[213]

ZrB_2-16SiC-64ZrC (vol.%)	2000, 5-10 sec	-	17	ZrO_2	″
ZrB_2-20SiC-15G (vol.%)	1800, 0.5 (P_{O2}=2000 Pa)	13	49	ZrO_2, SiO_2	[233]
ZrB_2-20SiC-15G (vol.%)	1800, 0.5 (P_{O2}=100 Pa)	-	47	ZrO_2, ZrB	″
ZrB_2-20SiC-15G (vol.%)	1800, 1.5 (P_{O2}=500 Pa)	-	66	ZrO_2, ZrB	[234]
ZrB_2-20SiC-15G (vol.%)	1800, 1.5 (P_{O2}=1500 Pa)		117	ZrO_2, ZrB	″
ZrB_2-20SiC-15G (vol.%)	1600, 1.5 (P_{O2}=50 Pa)	2.5	34	ZrO_2, ZrO	[214]
ZrB_2-20vol.% coarser SiC	1500, 3 (P_{O2}= 0.21 atm)	-	117	ZrO_2, SiO_2	[227]
ZrB_2-20vol.% fine SiC	1500, 3 (P_{O2}= 0.21 atm)	-	44	ZrO_2, SiO_2	″
ZrB_2-20vol.% coarser SiC	1500, 3 (P_{O2}= 2×10^{-4}-2×10^{-5} atm)	-	370	ZrO_2	″
ZrB_2-20vol.% fine SiC	1500, 3 (P_{O2}= 2×10^{-4}-2×10^{-5} atm)	-	54	ZrO_2, SiO_2	″
ZrB_2-15SiC-15G (vol.%)	1500, 8	-	68	ZrO_2, SiO_2	[193]
ZrB_2-20vol.% SiC	1600, 3	-	200-500	ZrO_2, SiO_2, $ZrSiO_4$	[215]
ZrB_2-20vol.% Si_2BC_3N	1600, 3	-	200-300	ZrO_2, SiO_2, $ZrSiO_4$	″
ZrB_2-20SiC-5.6B_4C-4.8Carbon- (7-14)LaB_6 (vol .%)	1300, 24	~11-8	129-103	ZrO_2, SiO_2, $ZrSiO_4$, $La_2Si_2O_7$	[216]
ZrB_2	1500, 3	29	1111	ZrO_2	[217]
ZrB_2-5vol.% AlB_2	1500, 3	24	775	ZrO_2, Al_2O_3	″
ZrB_2-20wt.% SiC	1650, 1	0.49	105	ZrO_2, SiO_2	[218]
ZrB_2-17.2SiC-14.01YB_4 (wt.%)	1650, 1	13.36	925	ZrO_2, SiO_2, $Zr_xY_{(1-x)}O_{(1.5+x/2)}$	″
ZrB_2-17.56SiC-12.22Y_2O_3 (wt.%)	1650, 1	29.57	839	ZrO_2, SiO_2, $Zr_xY_{(1-x)}O_{(1.5+x/2)}$	″
ZrB_2-5vol.% B_4C	1500, 3	0.05	193	ZrO_2	[75]
ZrB_2	1400, 1	11.7	291	ZrO_2	[194]
ZrB_2-20vol.% SiC	1400, 1	4.5	45	ZrO_2, SiO_2	″
ZrB_2-20vol.% SiC-2wt.% La_2O_3	1400, 1	2.1	28	ZrO_2, SiO_2	″
ZrB_2	1500, 3	14.9	150	ZrO_2	[219]
ZrB_2-4mol.% WC	1500, 3	10.7	50	ZrO_2, WO_3	″
ZrB_2-6mol.% Nb	1500, 3	-	79	ZrO_2, $Nb_2Zr_6O_7$	[258]
ZrB_2-(4-8)mol.% W	1600, 5 min	2.1-2.3	30-26	ZrO_2	[247]

ZrB_2-5wt.% B_4C	1500, 5	16.2	775	ZrO_2	[86]
ZrB_2-30vol.% SiC-2wt.% Al	1700, 1	24.5	200	ZrO_2, SiO_2	[195]
ZrB_2-30vol.% SiC-2wt.% Y	1700, 1	32.5	500	ZrO_2, SiO_2	″
ZrB_2-30vol.% SiC-7wt.% Y	1700, 1	24.5	200	ZrO_2, SiO_2, $Y_2Si_2O_7$	″
ZrB_2-20vol.% $MoSi_2$	1400, 30	6.5	-	ZrO_2, SiO_2, MoB	[130]
ZrB_2-15vol.% $MoSi_2$	1800, 0.25	-	180	ZrO_2, SiO_2, MoB, MoO_3	[244]
ZrB_2-20SiC-10$MoSi_2$ (vol.%)	1800, 1	12.79	~180	ZrO_2, SiO_2, MoB, $ZrSiO_4$	[196]
ZrB_2-0.5vol.% SiC	1600, 1	21.4	342	ZrO_2, SiO_2	[197]
ZrB_2-10SiC-10ZrO_2 (vol.%)	1200, 4	0.08	189	ZrO_2, SiO_2, B_2O_3	[198]
ZrB_2-10SiC-20ZrO_2 (vol.%)	1200, 4	0.19	241	ZrO_2, SiO_2, B_2O_3	″
ZrB_2-10SiC_f-10$ZrSi_2$ (vol.%)	1500, 10	12.7	130	ZrO_2, SiO_2	[199]
ZrB_2-15vol.% $TaSi_2$	1500, 0.25	-	68	ZrO_2, SiO_2, $TaZr_{2.75}O_8$	[251]
ZrB_2-15vol.% $TaSi_2$	1600, 0.25	-	500	ZrO_2, Ta_2O_5, $TaZr_{2.75}O_8$	″
ZrB_2-10vol.% $TaSi_2$	1500, 2	44	-	ZrO_2, $TaZr_{2.75}O_8$	[200]
ZrB_2-30vol.% $TaSi_2$	1500, 2	9	60	ZrO_2, $TaZr_{2.75}O_8$	″
ZrB_2-20vol.% SiC-10wt.% La_2O_3	1600, 1	-	250	ZrO_2, $ZrSiO_4$, $La_2Zr_2O_7$, La_2SiO_5	[201]
ZrB_2-20vol.% SiC-10wt.% LaB_6	1600, 1	-	250	ZrO_2, $ZrSiO_4$, $La_2Zr_2O_7$	″
Monolithic ZrB_2	1400, 2	18.7	300	ZrO_2	[200]
ZrB_2-15vol.% Ta_5Si_3	1400, 2	9.8	115	ZrO_2, $TaZr_{2.75}O_8$	″
ZrB_2-20vol.% Si_3N_4	1300, 2	6.7	60	ZrO_2	″
ZrB_2-15vol.% WSi_2	1650, 0.25	-	40	ZrO_2, SiO_2, WO_3	[132]
ZrB_2-20vol.% SiC	1600, 4	11.6	193	ZrO_2, SiO_2	[220]
ZrB_2-20vol.% SiC-2wt.% La_2O_3	1600, 4	19.6	343	ZrO_2, SiO_xC_y, ZrO_xC_y	″
ZrB_2-20SiC-6ZrC (vol.%)	1750, 0.5	-	62	ZrO_2, SiO_2	[202]
ZrB_2-15SiC- 10HfB_2 (vol.%)	1450, 20	4.88	125	ZrO_2, HfO_2, SiO_2	[203]
ZrB_2-40$MoSi_2$-5SiC (vol.%)	1500, 10	3	148	ZrO_2, MoB, $ZrSiO_4$	[205]

ZrB_2-40$MoSi_2$-20SiC (vol.%)	1500, 10	6	62	ZrO_2, MoB, $ZrSiO_4$, SiO_2	″

2.7 Applications

The unique combination of properties of diborides makes it suitable for various applications such as molten metal crucibles, cutting tools, wear resistant parts, electrodes for electro-discharge machining, cathode material for hall-heroult cell, electrical devices, reinforcement for improving conductivity and properties of other materials, armor materials, aluminum evaporation boat, energy applications (in nuclear and solar), rocket nozzles, refractory parts, and high temperature structural parts, etc. [9], [179], [259]–[271]. Among these applications, the possibility of using ZrB_2 composites as advanced structural material for TPS of space vehicles has resulted in such increasing interest and widespread research on this materials class [265], [266], [272]. In 1950s, blunt body concept was implemented for TPS in Apollo and Space Shuttle Orbiter. The large radius in blunt bodies developed a heavy detached shock wave with a high thickness of subsonic boundary layer that reduced the temperature and heating rate of TPS. This concept eradicates ablation on reusable leading edges and it also rises the drag. From this, sharp body concept came into picture with low drag and it requires lower thrust during lift-off and attain higher cross-range during re-entry [5], [9], [267]. The limiting step with sharp wing leading edge (WLE) designs is that the convective heating to the surface and the temperature of the surface with decreasing WLE radius. The temperature of WLE is inversely proportional to square root of WLE radius, i.e., temperature increases as the leading-edge radius decreases [273]. The surface temperature of sharp leading edges can reach to the temperature more than 2000 °C on the stagnation region. Only few materials such as the transition metal borides can withstand such extreme high temperatures and retain their dimensional stability in harsh oxygen flow environment [236].

Severe aerodynamic heating at the surface, especially at the sharp leading-edge geometries and noses, during atmospheric re-entry of such vehicles makes it rather mandatory

to use UHTC, especially the diborides, usually in the form of tiles. In addition to being used directly as bulk structural parts, the diborides are also being considered for use as protective coatings on other load bearing materials, including C/C composites, to minimize the problems involving oxidation during applications in hypersonic vehicles [9], [179], [268], [272], [274].

In an air breathing hypersonic cruise vehicle design, aerodynamic heating due to viscous dissipation increases as the cube of velocity which results in stagnation temperature of the order of 2400 K for cruise Mach number 7. Owing to high L/D ratio, wave rider derived hypersonic vehicles are used for long duration cruise mission in which stagnation is experienced all over the leading edge of wave rider. Thus, to withstand elevated thermal loads and pressure loads without any change in aerodynamic shape (i.e., to maintain shock-on-lip condition) and to retain the mechanical properties, UHTC are often the key candidate materials for the hypersonic regime. Within this family of potential materials, the ZrB_2 and HfB_2 based ceramics and composites are possibly the most promising (or most investigated) candidates for such applications. It is mainly because of its good elevated temperature properties (mechanical, and oxidation), when compared to TiB_2 and TaB_2 [269]–[271].

The diborides are also used for making ball bearings and other parts in machines that are subjected to high temperature applications. Furthermore, the chemical inertness and favorable electrical conductivity of the diborides, as compared to most ceramic materials, render them suitable as electrode materials for aluminum electro-smelting; and also, as elements for vacuum metal deposition equipment. With respect to structural applications involved with the generation of nuclear energy, the low neutron-absorption cross-sections of diborides make them excellent candidates for use as control rods in high temperature nuclear reactors. UHTC, in general, have also been thought about as potential candidates for solar energy absorbers in solar power applications with the expectations that they might be capable of raise the operating temperature capabilities of the solar plants without considerable material degradation [261], [262], [275]–[277]. The spectral characteristics have been found to be very favorable with

higher absorbance to emittance ratio and thus resulting in superior solar absorber performance. However, a possible drawback of using diborides for solar applications and allowing high temperatures in air is the possible oxidation of the surfaces. Transition metal diborides have been used as neutron shield in nuclear industry since these ceramics contain boron [278].

2.8 Summary

Among the group of UHTC, ZrB_2 ceramic is promising for hypersonic and atmospheric reentry vehicle applications. The difficulties in densifying single-phase ZrB_2, its moderate fracture toughness and low oxidation resistance at elevated temperatures limited the applications. Sintering temperatures more than 2000 °C and long holding times are necessary to get fully dense single phase ZrB_2. Hence, conventional and advanced sintering techniques and use of sintering additives were also extensively researched for improving sinterability and properties of ZrB_2. In particular, advanced sintering techniques and the sintering additives (in optimal quantity) aided in enhancing the densification and high temperature properties. The monolithic ZrB_2 is susceptible to high temperature oxidation. To improve the oxidation resistance of ZrB_2 ceramics different additives were used to form passive oxide layer on the surface of the composite from further diffusion of oxygen. SiC is a common reinforcement added to ZrB_2, which gives high dimensional stability, low creep rate and thermal expansion. Hence, ZrB_2-SiC composite is a good candidate for the different applications that need dimensional stability at high temperatures. From the literature, it realised that the addition of 20vol.% SiC to ZrB_2 is beneficial in improving its oxidation resistance along with lowering density.

In this backdrop, ZrB_2-20vol.% SiC was chosen as a base material in the present dissertation work. Si_3N_4 is an interesting ceramic with good strength, fracture toughness and oxidation resistance, while Ta is a refractory metal with good mechanical properties and ductility. Very limited studies exist on the use of Si_3N_4 or Ta as an additive for ZrB_2 or ZrB_2 based composites. The present study aims at developing dense ZrB_2-20vol.% SiC composites with varying addition of Si_3N_4 and tantalum by multi-stage SPS (MS-SPS) processing.

Particularly, in SPS processing, samples are heated at final sintering temperature for little longer holding times which causes degradation of the mechanical properties due to grain growth. To control this limitation, MS-SPS is advantageous.

Chapter 3

Experimental procedure

This chapter discusses the research methods followed in the present dissertation. It presents the framework of research methodology in preparing the sintered samples followed by microstructural and mechanical characterization. Further, this chapter describes the research methods followed for oxidation studies of the composites.

3.1 Raw materials

Commercially available ZrB_2 (H.C. Starck Grade B, GmbH and Co., Goslar, Germany), SiC (purity>99.8%, Alfa Aesar), Si_3N_4 (purity>99.8%, Alfa Aesar) and Tantalum (purity> 99.99%, India) powders were used for the processing of ZrB_2-SiC-Si_3N_4 and ZrB_2-SiC-Ta ceramic composites. The specifications of raw powders used in the processing of different composites is shown in **Table 3.1**.

Table 3.1 Specifications of raw materials used in the processing of the ZrB_2 composites

Material	Density (g/cm^3)	Average particle size (μm)
ZrB_2	6.08	2.25
SiC	3.21	1.45
Si_3N_4	3.20	0.85
Ta	16.69	3.80

The morphology of starting powders that are used in preparing of ZrB_2-SiC-Si_3N_4 and ZrB_2-SiC-Ta ceramic composites were analyzed using scanning electron microscopy (SEM) in **Figure 3.1**. The ZrB_2 particles are of platelet shape and its average particle size observed as 2.25 μm. Whereas the SiC and Si_3N_4 powders are of much finer, irregular and in the agglomerated form (**Figure 3.1 b and c**). The average particle size of SiC is 1.45 μm and Si_3N_4

average particles size is 0.85 µm. On the other hand, the Ta powders are of mixed shape (rod-like, spherical and platelet) and its average particle size is 3.8 µm (**Figure 3.1 d)**.

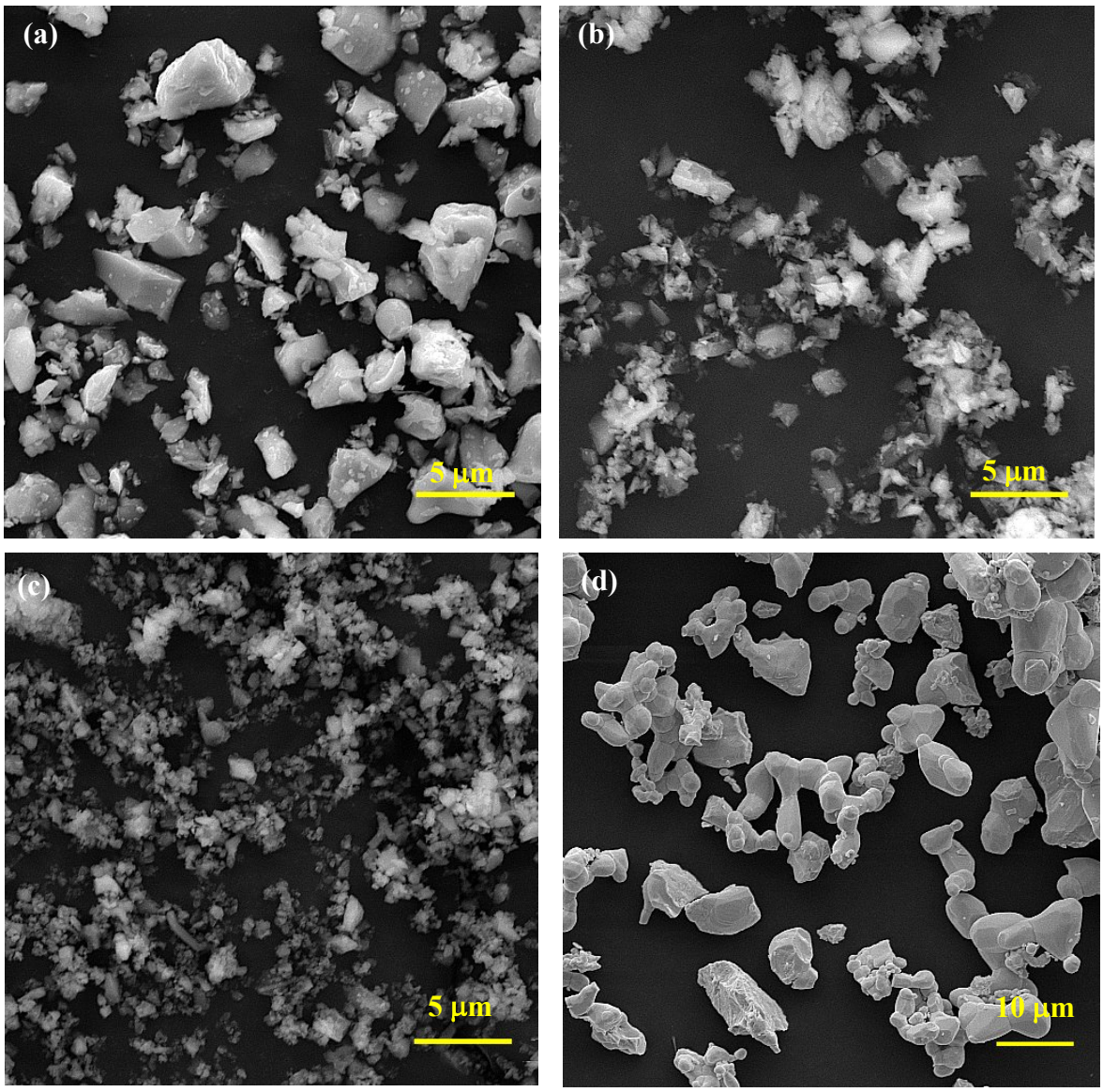

Figure 3.1 SEM images of starting powders (a) ZrB_2, (b) SiC, (c) Si_3N_4 and (d) Ta

The corresponding X-ray diffraction (XRD) patterns of starting powders is also presented in **Figure 3.2**, reveals only the respective crystalline phases of raw materials and no other additional phases could be found within the detection limits of XRD.

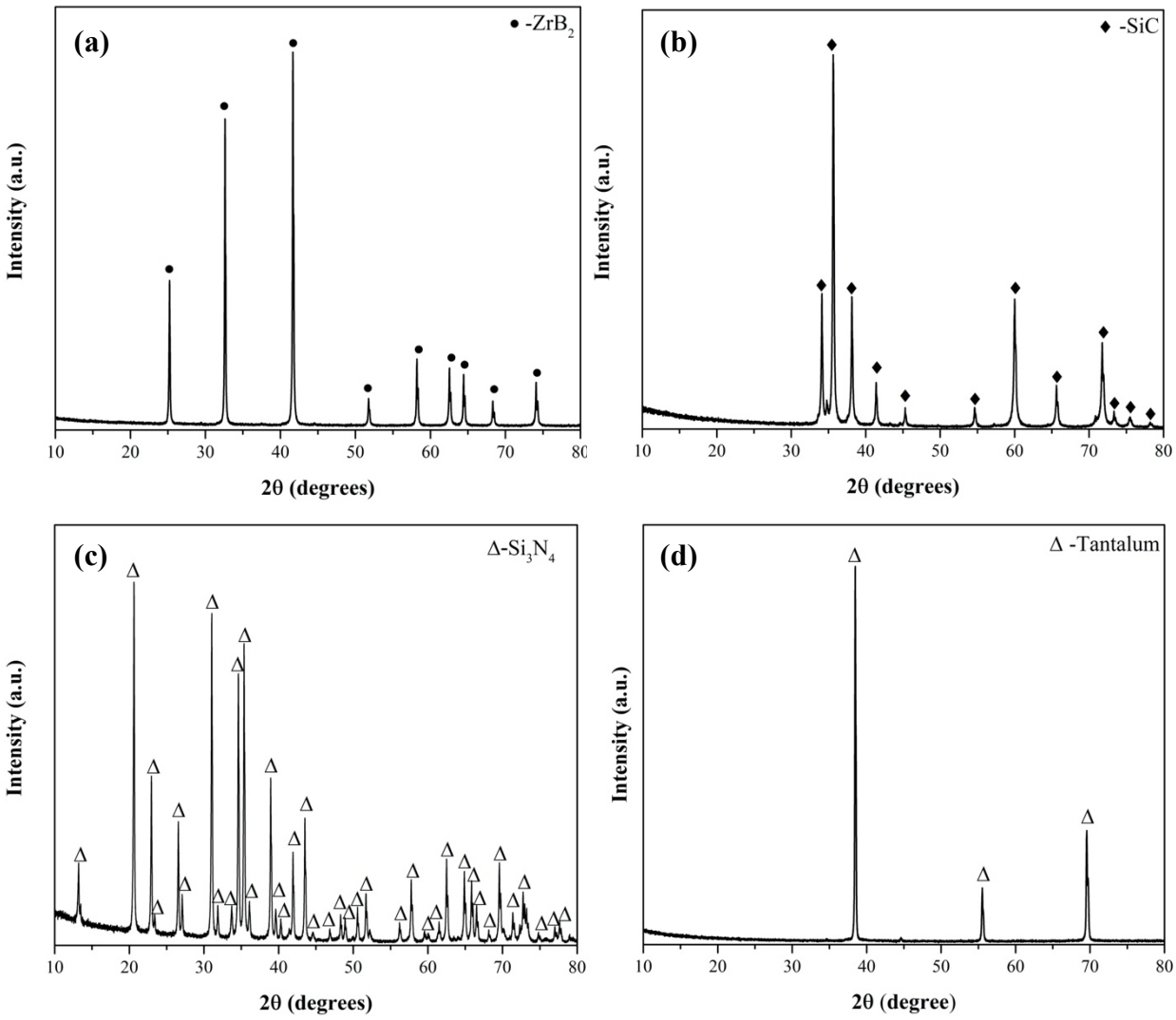

Figure 3.2 XRD patterns of (a) ZrB_2, (b) SiC, (c) Si_3N_4 and (d) Tantalum starting powders.

3.2 Powder processing

To prepare ZrB_2-based composites, the powders in appropriate amount were mixed by wet ball-milling using a planetary ball mill (Fritsch Pulverisette 6, Germany). The ball milling was carried out at 200 rpm for 6 h using Si_3N_4 milling media (the Si_3N_4 balls and the vials were lined with Si_3N_4) and toluene was used as a liquid medium with balls to powders weight ratio as 2:1. The use of toluene prevents oxidation and also acts as a process control reagent by maintaining lower temperature during milling. After mixing, the slurry was dried in a rotary vacuum evaporator at ~98 °C to remove toluene and minimize the particles agglomeration. The dried powders were granulated by pulverizing with a mortar and pestle.

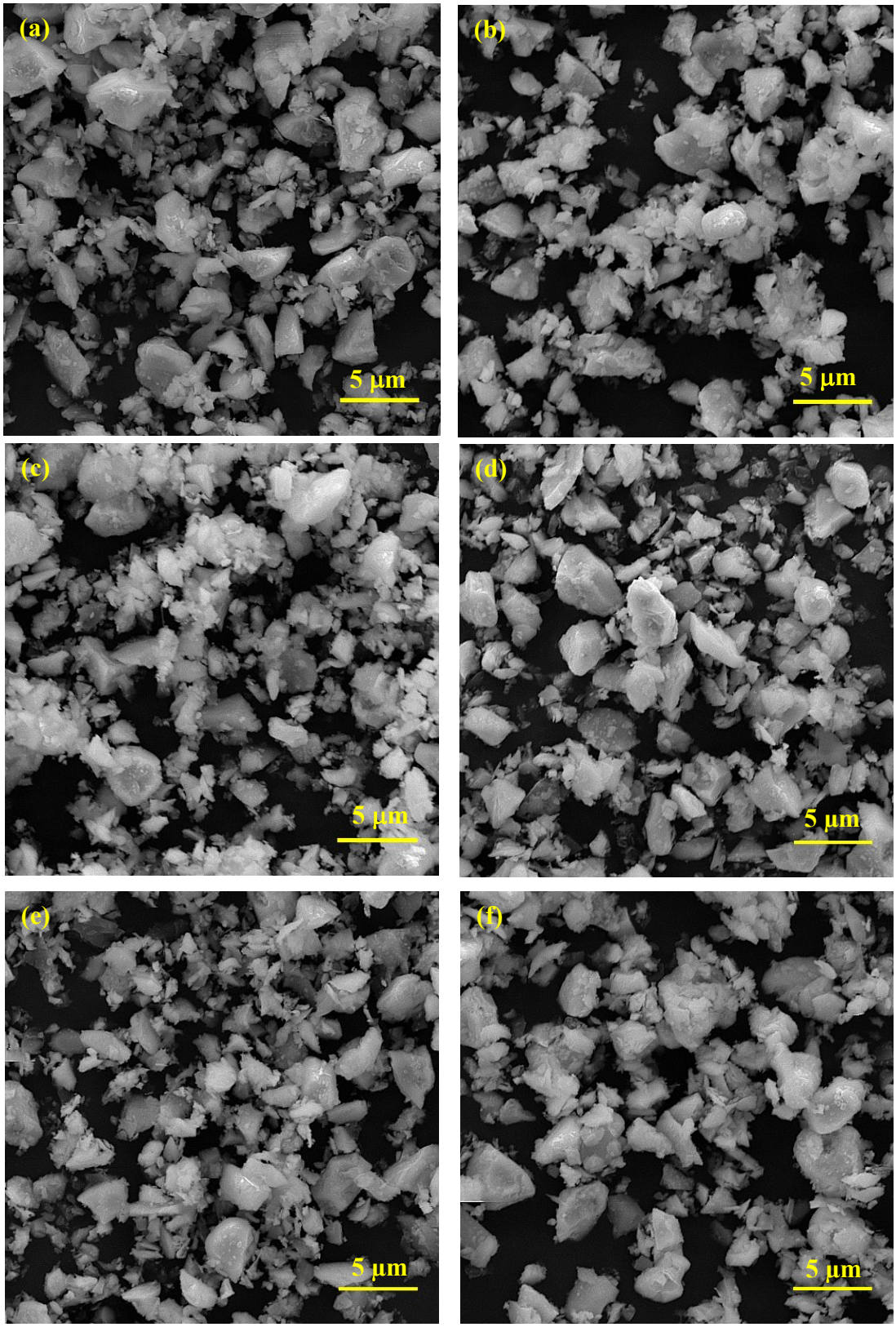

Figure 3.3 SEM images of ball-milled (a) ZS-2.5SN, (b) ZS-5SN, (c) ZS-10SN, (d) ZS-2.5Ta, (e) ZS-5Ta and (f) ZS-10Ta powders.

For convenience, the base composition ZrB_2-20vol.% SiC (ZS) reinforced with 2.5, 5 and 10vol.% Si_3N_4 was designated as ZS-2.5SN, ZS-5SN and ZS-10SN, respectively. On the other hand, ZS reinforced with 2.5, 5 and 10wt.% Ta was designated as ZS-2.5Ta, ZS-5Ta and ZS-10Ta, respectively. All the ball-milled powder compositions do not show any change in powder morphology and size as shown in **Figure 3.3**.

The XRD phases of ZrB_2-SiC- Si_3N_4 powder compositions after ball-milling (at 200 rpm for 6 h) is shown in **Figure 3.4(a)**. In case of ZS-2.5SN, only ZrB_2 and SiC phases could be observed and no traces of Si_3N_4 could be detected. It may be due to the detection limit of XRD to identify small fraction (2.5vol.%) of Si_3N_4. On the other hand, the presence of ZrB_2, SiC and Si_3N_4 phases were very evident in ZS-5SN and ZS-10SN samples. It also can be noted that the peak intensity of Si_3N_4 increased with increasing addition of Si_3N_4 amount to ZS powder compositions. **Figure 3.4(b)** shows the phases of ZrB_2, SiC and Ta in all the compositions and it is also observed that peak intensity of Ta increased with increasing amount of Ta.

3.3 Spark plasma sintering

Figure 3.5 shows the high temperature spark plasma sintering facility (Model: SPS 25–10, GT Advanced Technologies, USA) used for the densification of ZrB_2-based composites. The powders were sintered at different stages (multi stage) using SPS at temperature of 1800-1900 °C for 3 min under 50 MPa pressure in a vacuum (10^{-3} Pa) using graphite die and punches. Internal surface of dies was lined with graphite sheet prior to the filling of the powders. The multi stage SPS (MS-SPS) schedule is presented in **Figure 3.6**. The samples of 15 mm in diameter and thickness of 3–4 mm were prepared with the SPS.

The preliminary SPS experiments revealed that the measured experimental density of ZS-2.5SN increased from 5.31 to 5.37 g/cc with increasing SPS temperature from 1800 to 1900 °C. Hence, the other ZrB_2 composites were also processed at 1900 °C with a view to achieve high density.

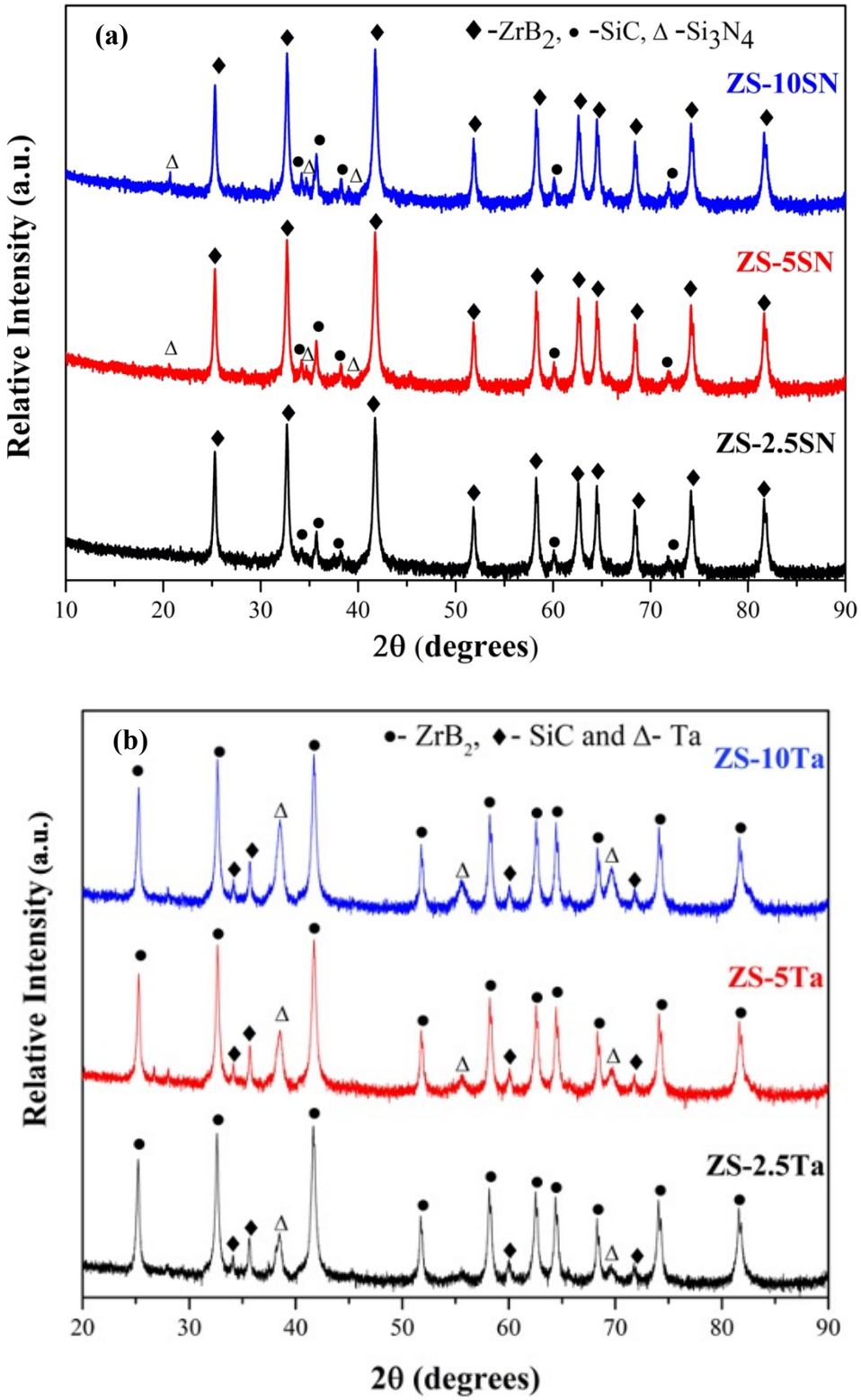

Figure 3.4 XRD patterns of ball-milled (a) ZrB_2-20vol.% SiC-Si_3N_4 and (b) ZrB_2-20vol.% SiC-Ta powder compositions.

Figure 3.5 SPS set-up used for the densification of ZrB_2-based composites.

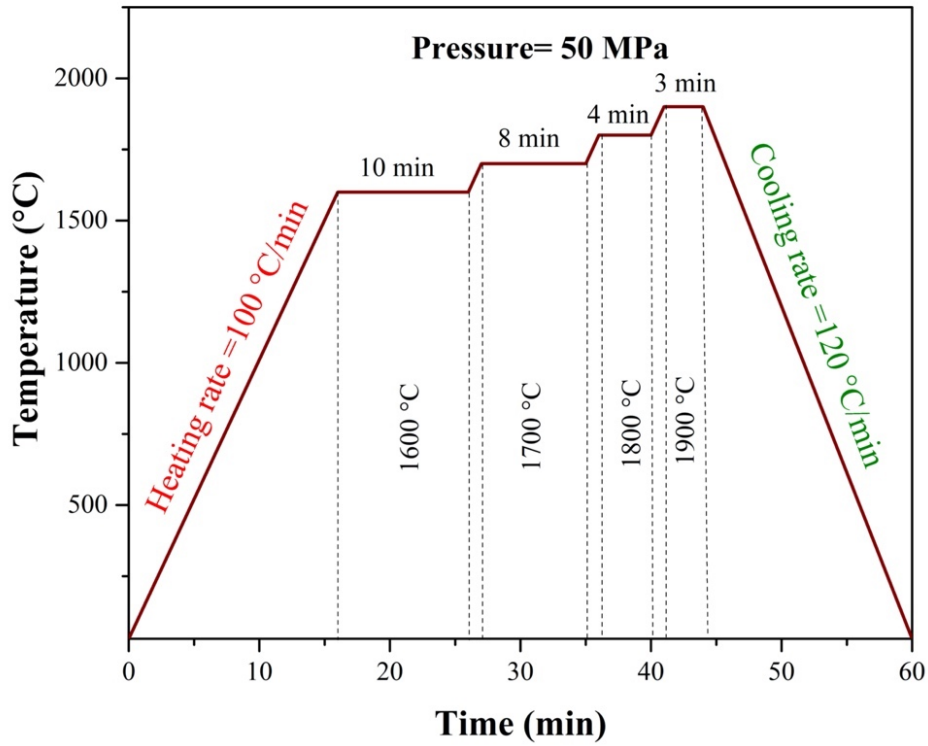

Figure 3.6 A schematic showing heating-cooling cycle followed while using MS-SPS to densify ZrB_2-20vol.% SiC-(2.5-10vol.%) Si_3N_4 and ZrB_2-20vol.% SiC-(2.5-10wt.%) Ta at a pressure of 50 MPa under vacuum.

3.4 Density measurement

After sintering, samples were ejected from graphite dies. The specimens were subjected to belt grinding, polishing and ultrasonic cleaning (using acetone). The final density of samples was measured using Archimedes' method, while the theoretical density of composites was calculated by rule of mixtures. To study the densification response of different composites, the final density was normalized with respect to theoretical density.

3.5 Microstructural characterization

The powders morphology and microstructural analysis of sintered and oxidized samples were carried out using scanning electron microscopy (SEM: TESCAN VEGA 3 LMU). The elemental analysis of ZrB_2-based composites was accomplished by energy dispersive spectroscopy (EDS: Oxford Instruments) attached to SEM. The ZrB_2 samples were polished with diamond paste up to 1 μm surface finish. The microstructure of samples was revealed by chemical etching of the samples using 10 HCl-1 HNO_3 solution at room temperature for 40 s. The average grain size of ZrB_2 was measured on multiple SEM images with ImageJ software package (ImageJ 1.51j8, National Institute of Health, USA). Further the phases formed during sintering (in ZrB_2-SiC-Si_3N_4 composites) were confirmed using Thermo-Calc (2017b) software. The Gibbs free energies of different chemical reactions in processing of ZrB_2-SiC-Si_3N_4 composites was calculated using HSC chemistry 6.1 software. The crystalline phases in the starting powders, ball milled compositions and MS-SPS samples were characterized by X-ray diffraction (XRD, PANalytical X'Pert Pro, Holland, CuKα=1.5405 Aº).

3.6 Vickers hardness measurement

The Vickers hardness of all the ZrB_2 samples was measured under 2 kg load at dwell time of 15 s using Vickers hardness tester (M/s. Shimadzu, HMV, Japan). At least 5 hardness measurements were taken for each individual sample.

3.7 Nano-indentation test

The nanoindentation experiments (Model: Nano Test Ventage, Microsoft Materials, UK) was used to evaluate the hardness and elastic modulus of the ZrB_2-20vol.% SiC-(0-10wt.%) Ta composites. The experiment was performed at a maximum load of 450 mN at loading rate of 40 mN/s. During the tests, the depth of penetration increased during loading and it reached the maximum depth of penetration at maximum load. On the other hand, during unloading the depth of penetration reduced due to elastic recovery. A permanent impression always observed after withdrawal of indenter and confirming the plastic deformation of the indented material. The difference in depth of penetration at maximum load was used for hardness measurement [279]. The sample elastic modulus (E_s) was measured by reduced modulus (E_r) using Eq. (37), and E_r was directly obtained from nano-indentation test by Eq. (38)

$$\frac{1}{E_r} = \frac{(1-\nu_s^2)}{E_s} + \frac{(1-\nu_i^2)}{E_i} \qquad (37)$$

$$E_r = \frac{dp}{dh}\left(\frac{1}{2\beta}\sqrt{\frac{\pi}{A}}\right) \qquad (38)$$

ν_s (0.13) and ν_i (0.07) indicates the poison ratio of sample and indenter; E_s and E_i (1141 GPa) indicates the elastic modulus of sample and indenter.

A = Indenter area β = Berkovich tip shape constant (1.034).

p = Load applied by indenter on the surface of sample

h = displacement during loading.

3.8 Oxidation studies

Oxidation studies of sintered ZrB_2-based composites were carried out in a box type furnace (Nabertherm, $MoSi_2$ heating element) under stagnant air. The rectangular samples for oxidation studies were prepared from bulk sintered samples using wire EDM. Prior to oxidation, the specimens were thoroughly cleaned using acetone in an ultrasonic bath. The cleaned specimens

were placed in a pure alumina crucible with minimal contact area and then the crucible was inserted at the center portion of furnace. Then, the samples were heated at 10 °C/min and isothermally held at different oxidation temperatures (1500 and 1600 °C) for 10 h. The weight of the sample before and after oxidation was measured. Further, the specific weight changes (in mg/cm^2) were evaluated by weight change divided by the total surface area of the sample. The oxide layer thickness of the samples was calculated from the cross-sectional SEM images. Detailed microstructural characterization of oxidized samples (both surface and cross-section) were evaluated using XRD and SEM- EDS.

Chapter 4

Effect of Si_3N_4 addition on ZrB_2-20SiC composite

The present chapter discusses the effect of Si_3N_4 addition on densification, microstructure and mechanical properties of ZrB_2-20SiC ceramics. ZrB_2-20vol.% SiC was processed via MS-SPS with the addition of 2.5, 5 and 10vol.% Si_3N_4 at 1900 °C, 50 MPa for 3 min.

4.1 Densification

Table 4.1 records the processing conditions together with density and hardness measurements of sintered ZrB_2 composites. It should be noted here that the presented ρ_{th} (based on initial powder compositions) of the ZrB_2 composites was estimated using rule of mixture by considering theoretical density of each individual phase. To calculate theoretical density of ZrB_2 composites, the densities of ZrB_2, SiC and Si_3N_4 were taken as 6.08 g/cc [102], 3.21 g/cc [233] and 3.2 g/cc [280], respectively. In the literature, most commonly the researchers presented densification of ZrB_2 materials based on the initial powder compositions despite the variation in phases of sintered samples final microstructure. It is supposed that such measurements may not be true representation of densification, if new phases are involved in the sintered samples. Hence, the relative density of ZrB_2-20SiC-(2.5-10)Si_3N_4 composites were alternatively estimated by determining the porosity of the samples from the SEM micrographs of sintered samples using ImageJ software. A common observation is that the density of ZrB_2 composites decreased (5.37–5.11 g/cc) with increasing addition of Si_3N_4, since its density is considerably low compared to ZrB_2. Almost full density (>98%ρ_{th}) of ZrB_2 composites was achieved when Si_3N_4 content was more than or equal to 2.5vol.%. The relative density was slightly lowered when higher amount (≥5vol.%) of Si_3N_4 was added to ZrB_2. It may be due to the formation of more amounts of secondary phases in the ZrB_2 composites. Bellosi and Monteverde studied the effect of different additives (Ni, SiC, Si_3N_4, AlN) on the densification, mechanical and oxidation properties of hot pressed ZrB_2 [281]. The hot press experiments were

performed over a range of temperature (1700–1870 °C), for 10–30 min under 30 MPa pressure. In case of monolithic ZrB_2, a maximum density of 87%ρ_{th} was obtained even after HP at 1870 °C. On the other hand, the ZrB_2-5vol.% Si_3N_4 and ZrB_2-19vol.% SiC composites could be densified to 98%ρ_{th}. Ahmadi et al. reported obtainment of 95%ρ_{th} for ZrB_2-30vol.% SiC after HP at 1900 °C under 10 MPa for 120 min. The ZrB_2-30vol.% SiC composite could be fully densified with the addition of Si_3N_4 (up to 5vol.%) [78].

Table 4.1 Densification and grain sizes of sintered ZrB_2-20SiC-(2.5-10)Si_3N_4 composites (RD: Relative density)

Composition	Sintering conditions (°C, MPa, min)	ρ_{th} g/cc (using starting powders)	Experimental Density (g/cc)	RD (from starting powders)	RD (from SEM images)
ZS20-2.5SN	1800, 50, 3	5.43	5.31	97.8	97.92
ZS20-2.5SN	1850, 50, 3	5.43	5.33	98.2	98.56
ZS20-2.5SN	1900, 50, 3	5.43	5.37	98.8	98.79
ZS20-5SN	1900, 50, 3	5.36	5.28	98.5	98.29
ZS20-10SN	1900, 50, 3	5.21	5.11	98.0	98.73

4.2 Phase and microstructural analysis

In all the sintered ZrB_2-20vol.%SiC-Si_3N_4 composites, ZrB_2 and SiC phases exist along with new phases (BN, ZrO_2 and ZrN) without any hint of Si_3N_4 (see **Figure 4.1**). Presence of such new phases in the sintered ZrB_2 composites clearly indicate involvement of sintering reactions. A careful look at XRD patterns reveals that the peak intensity of BN and ZrO_2 phases decreases, while the ZrN peak intensity increases with increasing the addition of Si_3N_4 to ZrB_2-20vol.% SiC. It is interesting to note that the crystalline ZrO_2 phase could not be identified in the starting or ball milled powders, however, the phase is noticed in sintered (SPS processed) ZrB_2 composites. Similar kind of observations (i.e. absence of ZrO_2 phase in powders and its presence in sintered samples) was also reported for hot pressed ZrB_2-$MoSi_2$ and ZrB_2-NdB_6 composites [83], [128]. In the following, more details will be discussed.

The back scattered electron (BSE)-SEM images indicate presence of different contrasting (bright, grey and dark) phases in ZrB_2-20SiC-(2.5-10)Si_3N_4 composites (**Figure 4.2**). The SEM-EDS confirms bright contrasting phase as ZrB_2, the grey phase as SiC and the dark phase as ZrN. The SiC and ZrN phases were well dispersed within the microstructure. The grain size of ZrB_2 varied narrowly between 3.37 and 3.61 μm and it slightly increased with increasing addition of Si_3N_4. In fact, the grain size of sintered ZrB_2 is very much comparable with initial ZrB_2 powders particle size and clearly indicate insignificant grain growth for the SPS ZrB_2 composites. The densification of SPS ZrB_2-20SiC-Si_3N_4 composites occurred mainly by Si_3N_4 addition, sintering reactions and liquid phase sintering. The presence of oxide impurity reportedly hinders the densification of borides due to evaporation-condensation and grain growth mechanisms. Since Si_3N_4 addition led to sintering reactions, it is consumed either due to its decomposition at high temperature or via sintering reactions in eliminating the oxide impurity of ZrB_2. The addition of Si_3N_4 not only removes the oxide impurities from the surface of ZrB_2 and it controls the grain growth of ZrB_2 by forming nitride phases (ZrN, BN) which hinders the grain growth of ZrB_2. Hence, Si_3N_4 is an effective sintering additive in enhancing densification with uniform fine microstructure of SPS ZrB_2 composites.

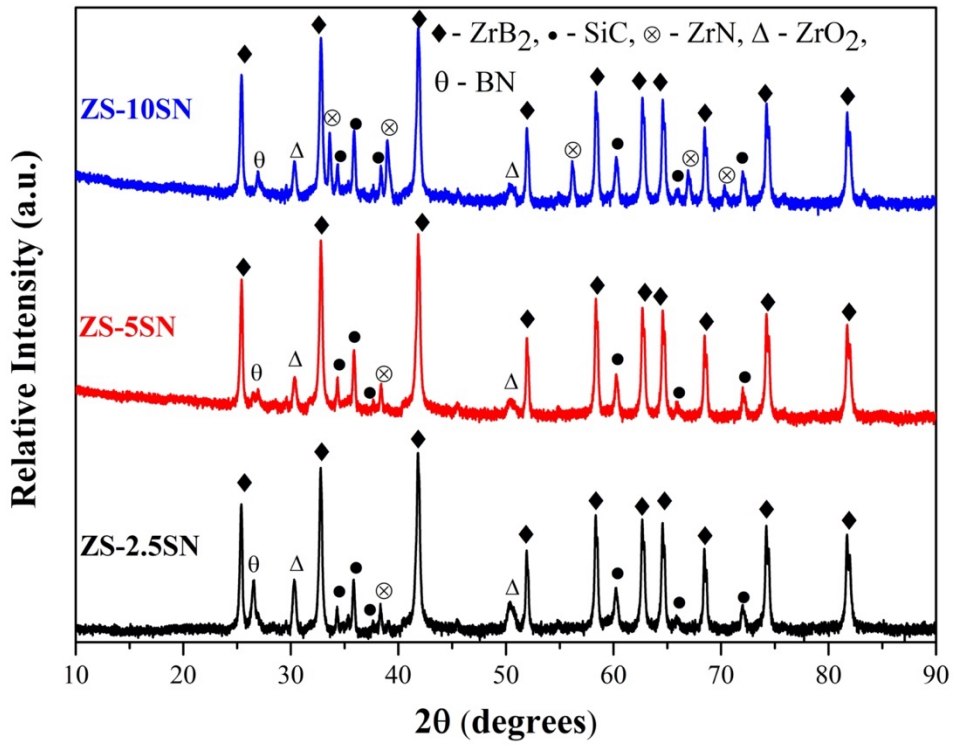

Figure 4.1 XRD phase analysis of ZrB_2-20SiC-Xvol.% Si_3N_4 (X= 2.5, 5 and 10) after multi stage SPS at 1900 °C, 50 MPa for 3 min.

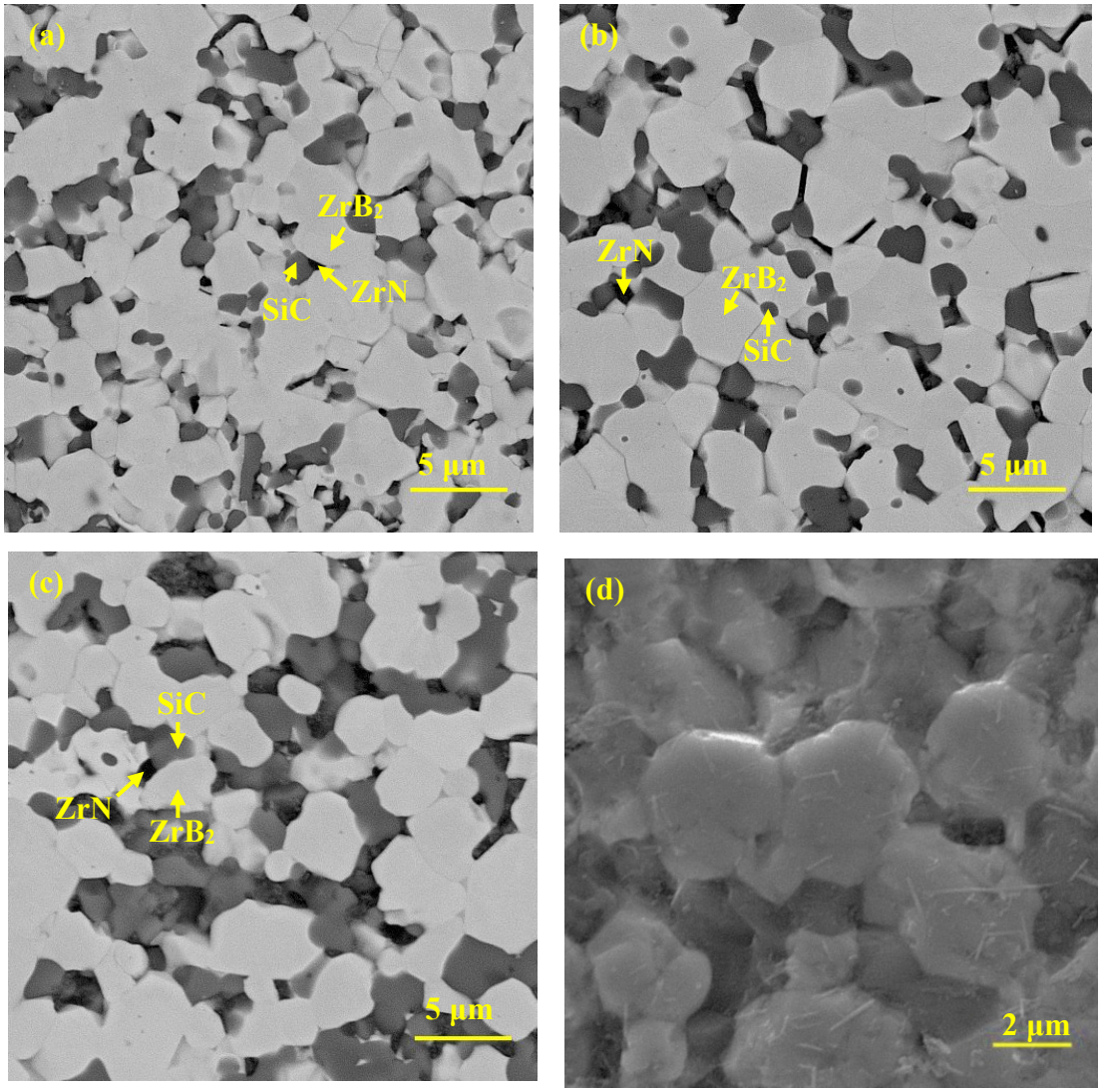

Figure 4.2 Microstructures of (a) ZS-2.5SN, (b) ZS-5SN, (c) ZS-10SN and (d) showing high magnification SE images of ZS-10SN sample, showing growth of BN platelets on the surface.

The secondary electron image of ZS-10SN composite is presented in **Figure 4.2 (d)**. The presence of needle like BN whiskers can be noticed from the micrographs. It is possible that BN whiskers grow during sintering. Similarly, the presence of BN platelets was also observed for hot pressed ZrB_2-30vol.% SiC-(1-5vol.%) Si_3N_4 and SPS TiB_2-5wt.% Si_3N_4

systems. [78], [282]. Ahmadi et al. reported that the BN platelets resemble like graphene structure, which formed due to 2D hexagonal growth of BN [78] .

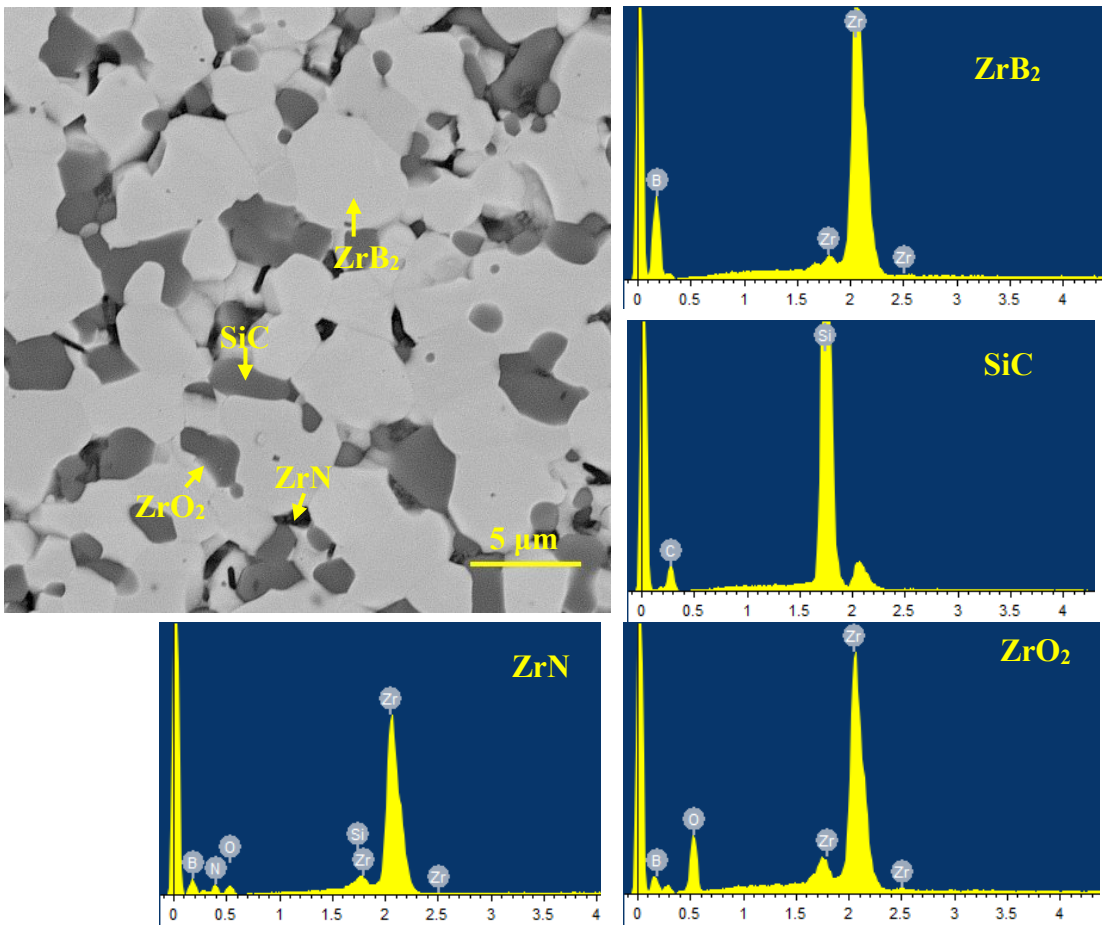

Figure 4.3 Microstructures of ZS-5SN and EDS elemental analysis of different phases observed in the microstructure.

The SEM image indicates presence of different contrasting phases in the SPS ZS-5SN (**Figure 4.3**). The SEM-EDS confirms bright contrasting grains as ZrB_2, the grey phase as SiC and the dark phase as ZrN. The irregular bright contrasting phase (small size) at the grain boundaries was identified as ZrO_2. All the secondary phases were well dispersed in the ZrB_2 matrix.

4.3 Sintering reactions

From the XRD patterns, it is clear that the SPS ZrB_2 composites consist peaks of ZrN, BN and ZrO_2 along with the ZrB_2 and SiC phases (**Figure 4.1**). No traces of Si_3N_4 could be observed in the XRD of as-sintered ZrB_2-SiC-Si_3N_4 composites. It might be due to complete consumption

of Si_3N_4 while it's reaction with the other phases during the SPS process. It was reported that the oxide impurities (B_2O_3 and ZrO_2) present as a thin layer on the outer surface of ZrB_2 powder particles [25]. At high temperatures it is possible that the Si_3N_4 ceramic can decompose into Si and N_2 [18]. The sintering reactions are possible to take place due to the presence of impurities in the powders, decomposition of Si_3N_4 and presence of carbonaceous medium during SPS. In fact, the SPS of ZrB_2 composites was carried using graphite dies. Hence, the ZrN and BN phases might have formed through the chemical reactions between the oxide impurities present on the surface of ZrB_2 powders and Si_3N_4 or Si, N_2 and C etc. according to following reactions.

$$2B_2O_3 + Si_3N_4 = 4BN + 3SiO_2 \quad (39)$$

$$3ZrO_2 + Si_3N_4 = 3ZrN + 3SiO_2 + 0.5N_2 \quad (40)$$

$$Si_3N_4 = 3Si + 2N_2 \quad (41)$$

$$2ZrB_2 + 3\ Si + 3N_2 + 3C = 2ZrN + 4BN + 3SiC \quad (42)$$

$$3ZrB_2 + 2Si + 4N_2 = 2ZrN + 6BN + ZrSi_2 \quad (43)$$

$$ZrB_2 + 1.5N_2 = ZrN + 2BN \quad (44)$$

To understand the thermodynamic feasibility of the above reactions, the free energy (ΔG) formation of the reactions (39–44) as a function of temperature is presented in **Figure 4.4**. It can be observed that reactions 39, 41, 42 and 44 are thermodynamically feasible as the free energy of these reactions are negative and the other reactions (40 and 43) do not take place as they exhibit positive free energy of formation. From **Figure 4.4**, it can be observed that reaction (39) is strongly negative at the sintering temperature of 1900 °C. So, the BN formation may be possible by reaction (39). Monteverde et al. also reported BN formation for ZrB_2-2.5wt.% Si_3N_4, which was consolidated via hot press at 1700 °C [52]. By closely observing **Figure 4.4**, it can be realized that reaction 39, 41 and 42 are more favorable during SPS process due to its strong negative free energy at 1900 °C. These sintering reactions indicate consumption of Si_3N_4 by forming new phases ZrN, BN, SiC and SiO_2. However, SiO_2 phase could not be observed from XRD or SEM analysis of the samples.

Figure 4.5 shows the isothermal section of Zr-N-B ternary phase diagram at 1900 °C, that is constructed using Thermo-Calc software. The phase diagram shows that ZrB_2, BN and ZrN phases are thermodynamically compatible. Based on this ternary phase diagram and proposed sintering reactions, it is very clear that formation of ZrN and BN phases are likely in ZrB_2-SiC-Si_3N_4 composites at a sintering temperature of 1900 °C. As explained earlier, the XRD results also corroborate the presence of ZrN and BN phases. Talmy et al. reported the formation of BN, $ZrSi_2$, ZrN phases along with ZrB_2 in ZrB_2-(5–35)vol.% Si_3N_4 composite (hot press:1850 °C, 20 MPa, 1 h) [200]. Bellosi and Monteverde observed BN, ZrO_2 and glassy phase (B-N-O-Zr-Si) for hot pressed ZrB_2-5vol.% Si_3N_4 composite [281]. The formation of such phases was due to the reaction between Si_3N_4 and (ZrO_2 and B_2O_3) present on ZrB_2 starting powders. In another work, Monteverde et al. proved the presence of grain boundary phases (BN, ZrO_2, $ZrSi_2$ and B-N-O-Zr-Si glassy phase) with thermodynamic calculations for ZrB_2-2.5wt.% Si_3N_4 composites [52]. Similarly, Park et al. observed TiN, BN and amorphous SiO_2 for hot pressed TiB_2-Si_3N_4 ceramics due the sintering reaction between the Si_3N_4 and TiO_2 that was present on the surface of TiB_2 powders [283]. Guo et al. reported the formation of ZrN, BN, $ZrSi_2$, SiC or Si phases for Si_3N_4-30wt.% ZrB_2 composite that were hot pressed at 1700 °C under Ar or N_2 atmosphere [18]. Interestingly, presence of BN nano-platelets, TiN and crystalline SiO_2 phases were reported for SPS TiB_2-Si_3N_4 due to the reaction between Si_3N_4 and TiO_2 and B_2O_3 oxides that were present on TiB_2 powders [282].

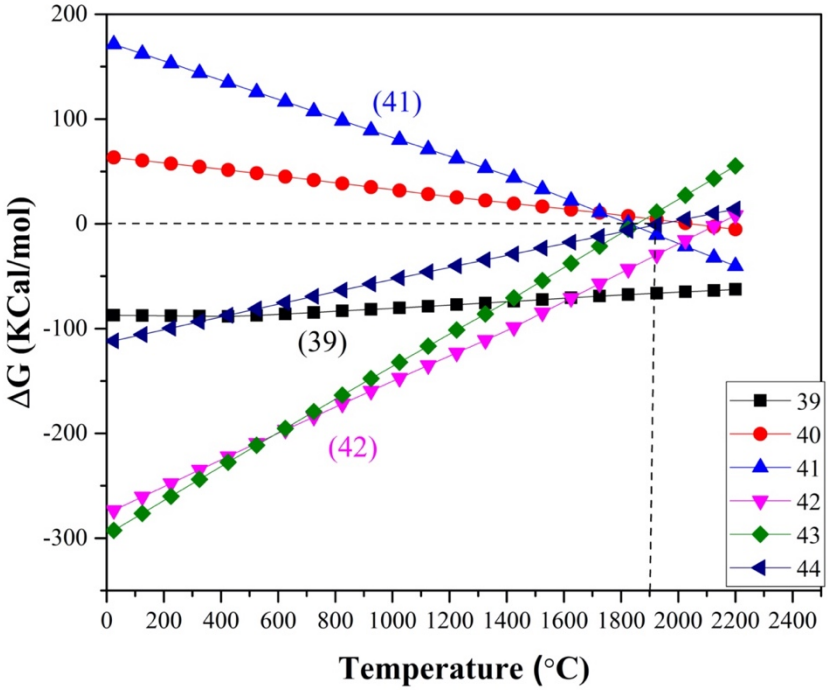

Figure 4.4 Gibbs free energy change of proposed sintering reactions (39–44) as a function of temperature, constructed using HSC chemistry.

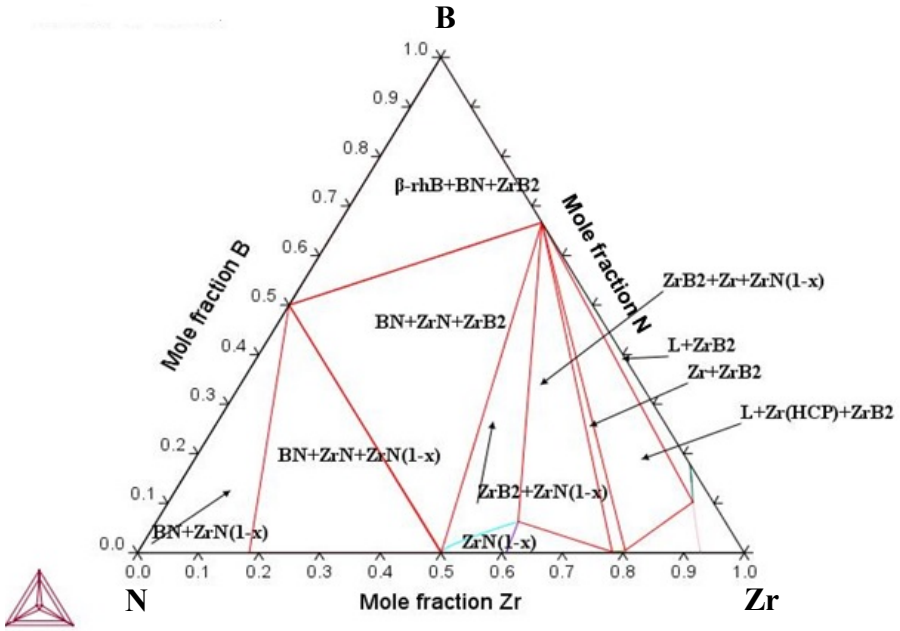

Figure 4.5 Isothermal section of Zr-N-B ternary phase diagram (at 1900 °C) constructed using Thermo-Calc software.

4.4 Fractography

The microstructure of fracture surfaces of SPS ZrB_2-based composites is shown in **Figure 4.6**. Mixed mode (transgranular and intergranular) of fracture without any indication of pores was noticed for ZS with 2.5, 5 and 10vol.% Si_3N_4 composites. The grains in the fracture surface were completely connected together, which signifies good densification of samples. A close observation of **Figure 4.6** clearly indicates the presence of nano sized needle shaped platelets (represented by circles). Germi et al. also observed BN nano-platelets in the fractured surface of TiB_2-20vol.% SiC-5wt.% Si_3N_4, which is sintered using SPS at 1900 °C, 40 MPa for 7 min [284].

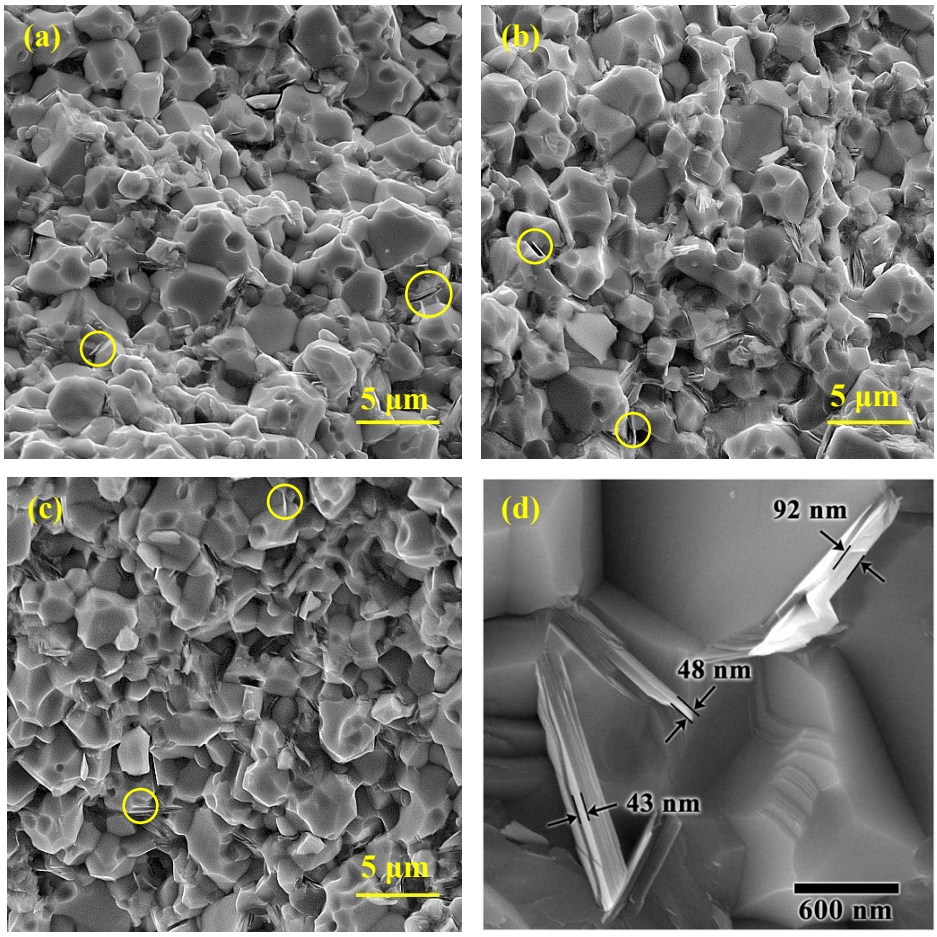

Figure 4.6 SEM micrographs of fracture surfaces of (a) ZS-2.5SN, (b) ZS-5SN and (c) ZS-10SN, the presence of nano sized needle shaped platelets were represented by circles. (d)

Fracture surface of TiB_2-20vol.% SiC-5wt.% Si_3N_4 (sintered at 1900 °C, 40 MPa for 7 min) showing in-situ formed BN nano-platelets [284].

4.5 Hardness

The hardness of ZS-2.5SN improved significantly from 20.61 to 25.59 GPa with increasing sintering temperature from 1800 to 1850 °C. Such improvement in hardness can be attributed to enhanced densification of the sample. Nevertheless, the enhancement in densification is not as drastic as the hardness of the ZS-2.5SN composite. On the other hand, further increasing the sintering temperature (up to 1900 °C) did not yield any notable improvement in the hardness or density of the composite. Interestingly, further increasing the amount Si_3N_4 (up to 5vol.%) resulted outstanding enhancement of hardness (30.56 GPa) and densification (more than 98%ρ_{th}). However, the hardness was reduced to 25.49 GPa with ZS-10SN due to its relatively low density and more amount of secondary grain boundary phases. Bellosi and Monteverde reported maximum hardness of 13.4 GPa for the hot pressed ZrB_2-5vol.% Si_3N_4 composites, which was densified to 98%ρth [281]. A slight increase in hardness of 14.2 GPa was noticed for ZrB_2-19vol.% SiC. Gupta et al. reported that ZrB_2-SiC-$TiSi_2$ could exhibit high hardness (27 GPa) for samples subjected to multi stage SPS when compared to single step conventional SPS due to its refined microstructure [102]. Hence, in multi-stage SPS the composites would achieve homogeneous microstructure and high density with fine grain size, which intended to enhance the mechanical properties.

The grain size of ZrB_2 slightly increased from 3.37 to 3.61 μm with increasing addition of Si_3N_4. Since the densification and grain size of all the ZrB_2 composites (SPS at 1900 °C for 3 min) are almost in the same range, the difference in hardness of the samples can be mainly attributed to the amount of the phases that are present in it and its distribution. It reflects that when higher amount of secondary phases present, the hardness of ZrB_2 decreases. Park et al. also observed similar kind of behavior for TiB_2-Si_3N_4 composites [283]. Based on the present results, it can be realized that ZS-5SN is optimal composition among all as it exhibited

maximum hardness and density. The hardness of ZS with 5vol.% of Si_3N_4 was improved due to enhancement in density and uniform distribution of secondary phases.

4.6 Summary

ZrB_2-20vol.% SiC (ZS) ceramics with varying amounts of Si_3N_4 (2.5, 5 and 10vol.%) were processed by multi stage Spark Plasma Sintering (SPS) over a range of temperature (1800–1900 °C) for 3 min under 50 MPa. All the ZS-Si_3N_4 composites could be densified to more than 98%ρ_{th} after SPS at 1900 °C. The XRD, SEM-EDS analysis of the ZS-Si_3N_4 composites revealed the presence of reaction product phases (ZrO_2, BN, ZrN) along with SiC and ZrB_2 major phases. Sintering reactions were proposed to explain the existence of such new phases and extinction of Si_3N_4. Thermo-Calc software was also used to further confirm the formation of these new phases in the ZS-Si_3N_4 samples. The hardness of ZS-Si_3N_4 composites varied between 25.50 and 30.56 GPa, in particular, ZrB_2-20vol.% SiC-5vol%. Si_3N_4 measured with the maximum hardness.

Chapter 5

Oxidation studies of ZrB_2-20SiC-(2.5-10)Si_3N_4 composites

The present chapter discusses the oxidation behavior of ZrB_2-20SiC-Si_3N_4 composites at different oxidation temperatures of 1500 and 1600 °C for 10 h.

5.1 Oxidation behavior at 1500 °C

Figure 5.1 presents the specific weight gain and oxide layer thickness of ZrB_2-20vol.% SiC-Xvol.% Si_3N_4 (X=2.5, 5.0 and 10.0) composites after oxidation at 1500 °C for 10 h. As the amount of Si_3N_4 increased, the weight gain of ZrB_2-20vol.% SiC composites decreased (from 13.84 to 9.84 mg/cm^2) and oxide layer thickness increased (64–128 μm). The weight change of the ZrB_2 composites is mainly due to the involvement of different reactions during oxidation (see **Table 5.1**). From **Table 5.1**, it is clear that the reactions (45), (47), (49) and (50) would be resulting for the increase in weight of ZrB_2 composites and reactions (46) and (48) would be leading in weight loss of the samples. The following are the oxidation reactions that are possible at the oxidation test conditions (see **Table 5.1**)

$$ZrB_2 + 5/2O_2\,(g) = ZrO_2\,(s) + B_2O_3\,(l) \quad (45)$$

$$B_2O_3\,(l) = B_2O_3\,(g) \quad (46)$$

$$SiC + 3/2O_2\,(g) = SiO_2\,(l) + CO\,(g) \quad (47)$$

$$SiC + O_2\,(g) = SiO\,(g) + CO\,(g) \quad (48)$$

$$2ZrN + 2O_2\,(g) = 2ZrO_2 + N_2(g) \quad (49)$$

$$4BN + 3O_2\,(g) = 2B_2O_3\,(l) + 2N_2\,(g) \quad (50)$$

From **Table 5.1**, except reaction (46) all the other reactions are thermodynamically feasible as they exhibit strong negative free energy. However, thermodynamic models that employ volatility diagrams and kinetic models support evaporation of B_2O_3 at 1500 °C in air [285]. It is well known that the oxidation of ZrB_2 phase led to the formation of ZrO_2 and B_2O_3. At high temperatures (>1400 °C), the vaporization of B_2O_3 takes place and left the porous and non-protective ZrO_2 on the surface of ZrB_2 [285], [286]. In case of ZrB_2 composites, the

presence of Si containing reinforcements (SiC) helps to form SiO_2 and CO. The reaction (47) signifies passive oxidation of SiC and at low oxidation potentials or elevated temperatures the active oxidation of SiC (reaction (48)) takes place. The viscous glassy silica oxide layer shields the surface and limits the inward diffusion of oxygen into the surface of the sample [220], [254], [287]. The formation of dense SiO_2 layer realized to be beneficial for mechanical properties as well [220]. The other ZrN and BN phases of ZS-SN composites also takes place in its oxidation (as per reactions (49&50)). For comparison purpose the oxidation characteristics in terms of weight gain, oxide layer thickness of various ZrB_2 composites is presented in **Table 5.2** [86], [199], [200], [205], [208], [225], [288]–[292]. Talmy et al. studied the effect of addition of SiC, Si_3N_4, Ta_5Si_3 and $TaSi_2$ on the oxidation behavior of ZrB_2 over a range of temperature 1200–1500 °C [200]. In case of pure ZrB_2, low weight loss (6 mg/cm^2) and maximum oxide layer thickness (160 μm) was noticed after oxidation at 1300 °C for 2 h (**Table 5.2**). Under similar oxidation conditions, increase in weight gain (14 mg/cm^2) and reduction in oxide layer thickness (140 μm) was noticed when ZrB_2 reinforced with 5vol.% Si_3N_4. The less weight gain for pure ZrB_2 when compared to ZrB_2-5vol.% Si_3N_4 was attributed to the more weight loss due to evaporation of B_2O_3 in pure ZrB_2 than the composite. On the other hand, significant increase in weight gain of 25 and 28 mg/cm^2 was reported for pure ZrB_2 and ZrB_2-5vol.% Si_3N_4, respectively when the materials were oxidized at higher temperatures (1500 °C, 2 h). Excellent oxidation resistance or very minimal weight gain (5 mg/cm^2) was reported for ZrB_2-25vol.% SiC composite [200]. Similarly, very minimal weight gain (5 mg/cm^2) was reported for ZrB_2-20vol.% SiC-40vol.% $MoSi_2$ even after oxidation at 1500 °C for longer duration of 10 h due to the formation of dense rich SiO_2 glassy oxide layers [205]. In a different work, the oxidation behavior of textured and untextured ZrB_2-20vol.% $MoSi_2$ composites was investigated [290], [291]. It was reported that the textured ZrB_2 composites exhibited better oxidation resistance (weight gain of 7 mg/cm^2 after oxidation at 1500 °C for 12 h) than the untextured composites, however, the oxide layer thickness was quite high (155 μm). Moderate weight gain (12.7

mg/cm^2) and oxide layer thickness (65 μm) was reported for ZrB_2-10SiC_f-10$ZrSi_2$ after oxidation at 1500 °C for 10 h [199]. In case of oxidation of pure ZrB_2, Fahrenholtz and Hilmas reported formation of small oxide layer thickness of 10 μm (at 900 °C for 8 h) and a very larger oxide layer thickness of 400 μm (1500 °C for 2 h) [236]. By a careful look at **Table 5.2**, it can be realized that the oxidation characteristics (weight gain varied from 9.84 to 13.84 mg/cm^2 and oxide layer thickness between 64 and 128 μm) of SPS ZS-SN composites is comparable with other ZrB_2 composites and exhibiting better oxidation resistance.

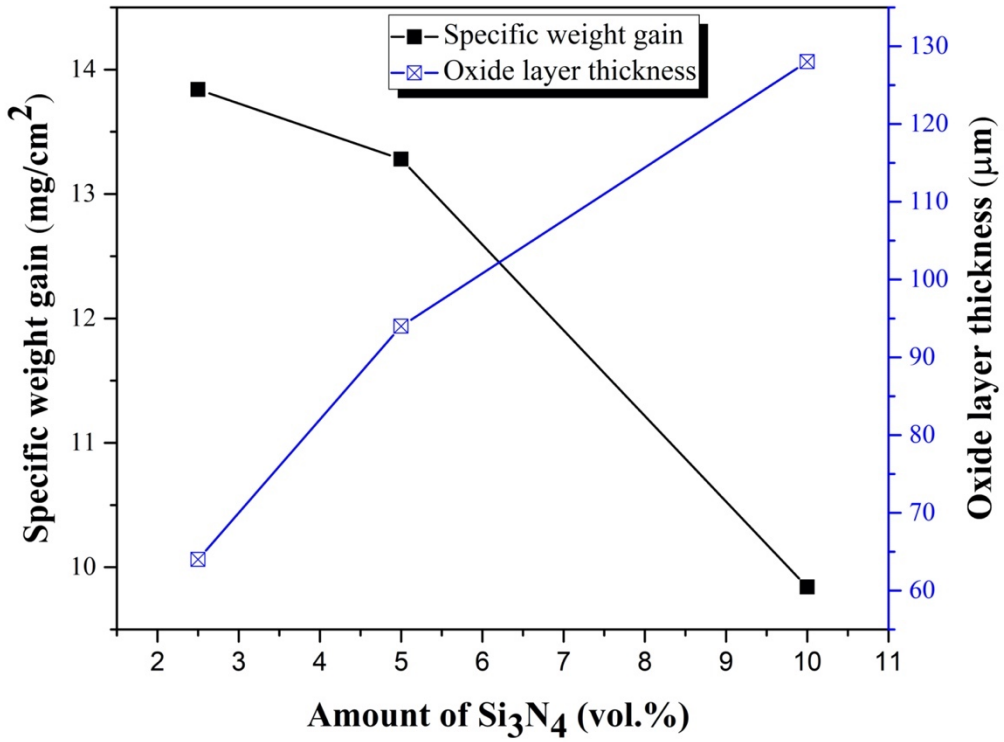

Figure 5.1 Weight gain and oxide layer thickness as a function of Si_3N_4 amount after oxidation of ZrB_2-20SiC composites at 1500 °C for 10 h.

Table 5.1 Weight change and free energy formation (ΔG) of ZrB_2-20SiC-(2.5-10)Si_3N_4 composites with different oxidation reactions

S. No.	Oxidation Reactions	Mass per mole of	Δw, g	ΔG (KCal/mol) at oxidation Temp. (1500 °C)
1	$ZrB_{2(s)}+5/2O_{2(g)} = ZrO_{2(s)}+B_2O_{3(l)}$ (45)	ZrB_2	80	-320.07
2	$B_2O_{3(l)}= B_2O_{3(g)}$ (46)	B_2O_3	-69.6	22.11
3	$SiC_{(s)}+3/2O_{2(g)}= SiO_{2(l)}+CO_{(g)}$ (47)	SiC	20	-192.82
4	$SiC_{(s)}+O_{2(g)}= SiO_{(g)}+CO_{(g)}$ (48)	SiC	-40	-109.19
5	$2ZrN_{(s)}+2O_{2(g)}= 2ZrO_{2(s)}+N_{2(g)}$ (49)	ZrN	36	-272.40
6	$4BN_{(s)}+3O_{2(g)}= 2B_2O_{3(l)}+2N_{2(g)}$ (50)	BN	40	-318.69

A thorough microstructural investigation of cross-section and surface of the oxidized ZrB_2-20SiC-Si_3N_4 composites were carried out to understand the oxidation behavior. **Figure 5.2** shows the cross-sectional SEM images of oxidized ZrB_2 samples after oxidation at 1500 °C for 10 h. It was observed that all the samples composed of stacking of three different layers, but the thickness of the layers were varying. The ZrB_2 composites consist of top silica rich layer, intermediate SiO_2-ZrO_2 layer and base material (unreacted). From **Figure 5.2**, it can be noticed that the thickness of outer SiO_2 layer and intermediate SiO_2-ZrO_2 layers varying considerably and in particular, its size increased with increasing Si_3N_4 amount. In the intermediate layer, the ZrO_2 content is observed to be more with more amount of Si_3N_4 addition to ZS (see **Figure 5.2 d, f** and **h**). The unreacted beneath layer composed of ZrB_2 and SiC (**Figure 5.2 e, g** and **i**).

Figure 5.3 shows representative SEM-EDS of cross-sectional microstructure of ZS-2.5SN after oxidation. The microstructure consists of thick dense outer layer of SiO_2,

intermediate (ZrO_2-SiO_2) layer and unreacted bulk. The corresponding EDS spectra also confirmed the presence of ZrO_2 and SiO_2 phases in the intermediate layer, ZrB_2 and SiC phases in the beneath unreacted bulk. In most of the cases, presence of SiC depleted layer along with SiO_2 and unreacted base material has been reported for the oxidation of ZrB_2-SiC composites [25], [192], [236], [285], [286]. The SiC depleted layer lowers the oxidation resistance of ZrB_2 composites. However, in the present SPS ZS-SN samples, SiC depleted layer was not observed. These observations clearly indicate good oxidation resistance of the ZS-SN composites. Zhang and Padture have observed improved oxidation resistance for borosilicate glass coated ZrB_2-20vol.% SiC composite after oxidation at 1500 °C for up to 20 h duration in air [287]. They also did not report any SiC depleted layer for the composite. In another work, Seong et al. studied the effect of partial pressure of oxygen on SiC (up to 30vol.%) reinforced ZrB_2 [254]. Presence of top SiO_2 layer and ZrO_2-SiO_2 mixed layer along with base material (without any SiC depletion layer) were observed after oxidation at 1500 °C for different time durations (up to 10 h).

The microstructure of oxidized samples surfaces after oxidation (at 1500 °C for 10 h) were shown in **Figure 5.4**. ZrO_2 (grey) and SiO_2 (dark) phases were noticed in all samples. The presence these phases were confirmed by EDS analysis as well. The formation of these phases can be understood from the oxidation reactions as presented in **Table 5.1**. The oxidation of ZrB_2 and ZrN phases results in the formation of ZrO_2. From **Figure 5.4**, it is evident the grain size of ZrO_2 significantly reduced with increasing Si_3N_4 content. The grain size of ZrO_2 was reduced considerably (from 3.04 μm to 1.91 μm) with the addition of 10vol.% Si_3N_4 to ZS. It reflects that the growth of ZrO_2 was hindered in ZS-10SN due to high amount of silica layer, which retards the growth of ZrO_2. Zhang et al. reported that ZrO_2 particle size increases in ZrB_2-SiC-ZrC with increasing oxidation temperature and time [293].

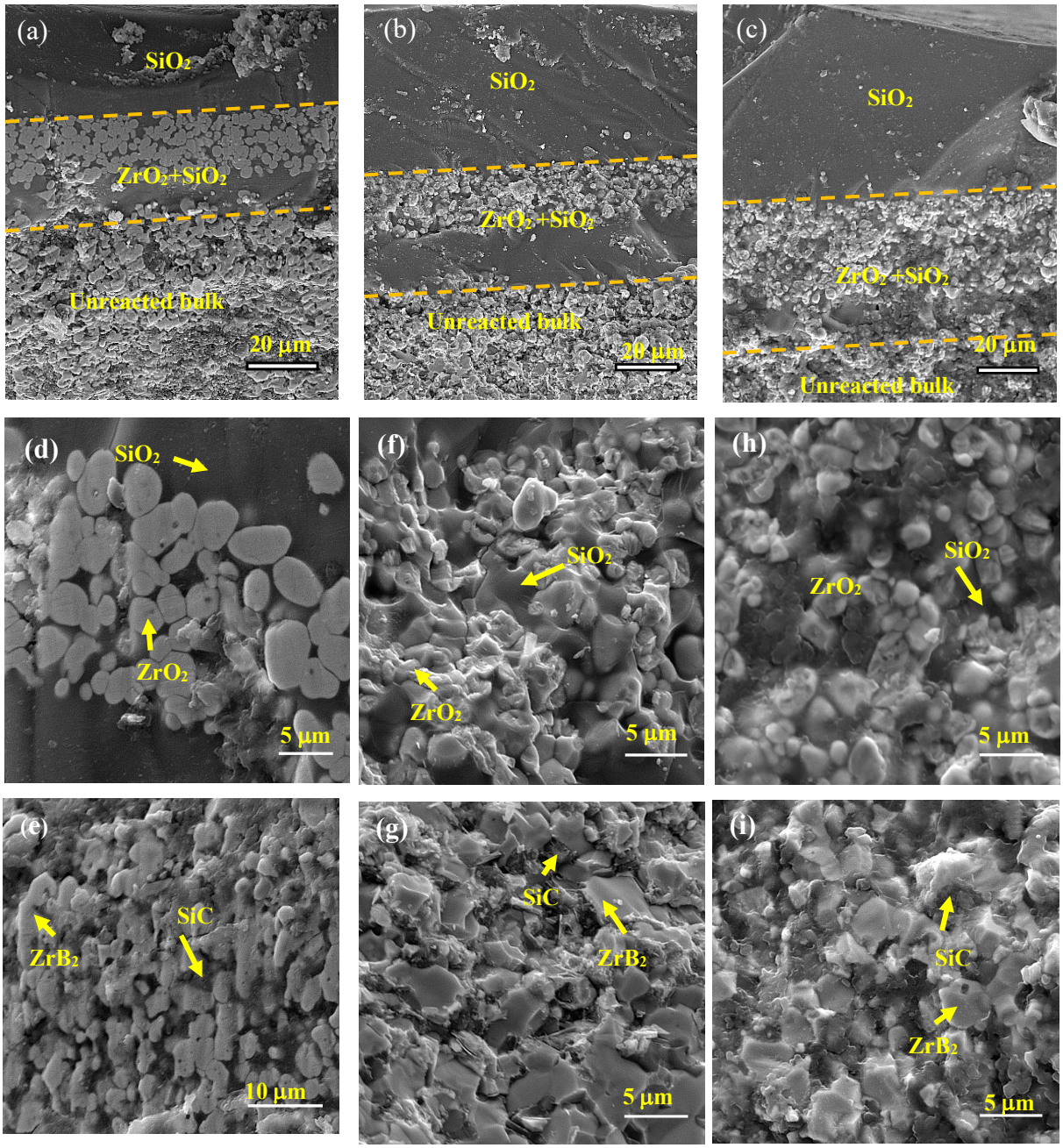

Figure 5.2 Cross sectional SEM micrographs of oxidized (a, d, e) ZS-2.5SN, (b, f, g) ZS-5SN and (c, h, i) ZS-10SN and its high magnification images of ZrO_2-SiO_2 layer (d, f and h) and unreacted bulk (e, g and i).

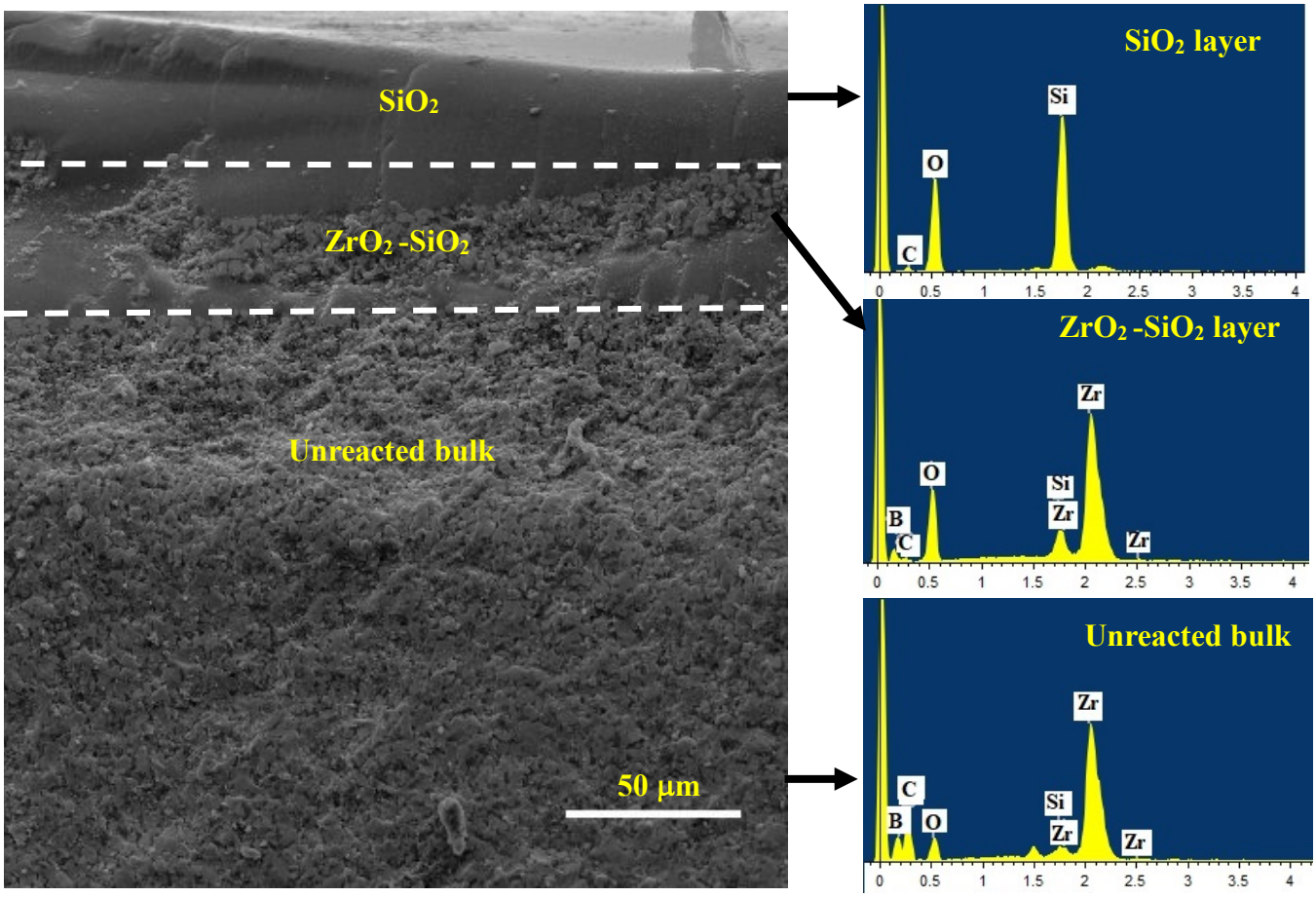

Figure 5.3 SE micrographs of cross-sectional surface of ZS-2.5SN after oxidation at 1500 °C for 10 h and its respective layers EDS elemental map.

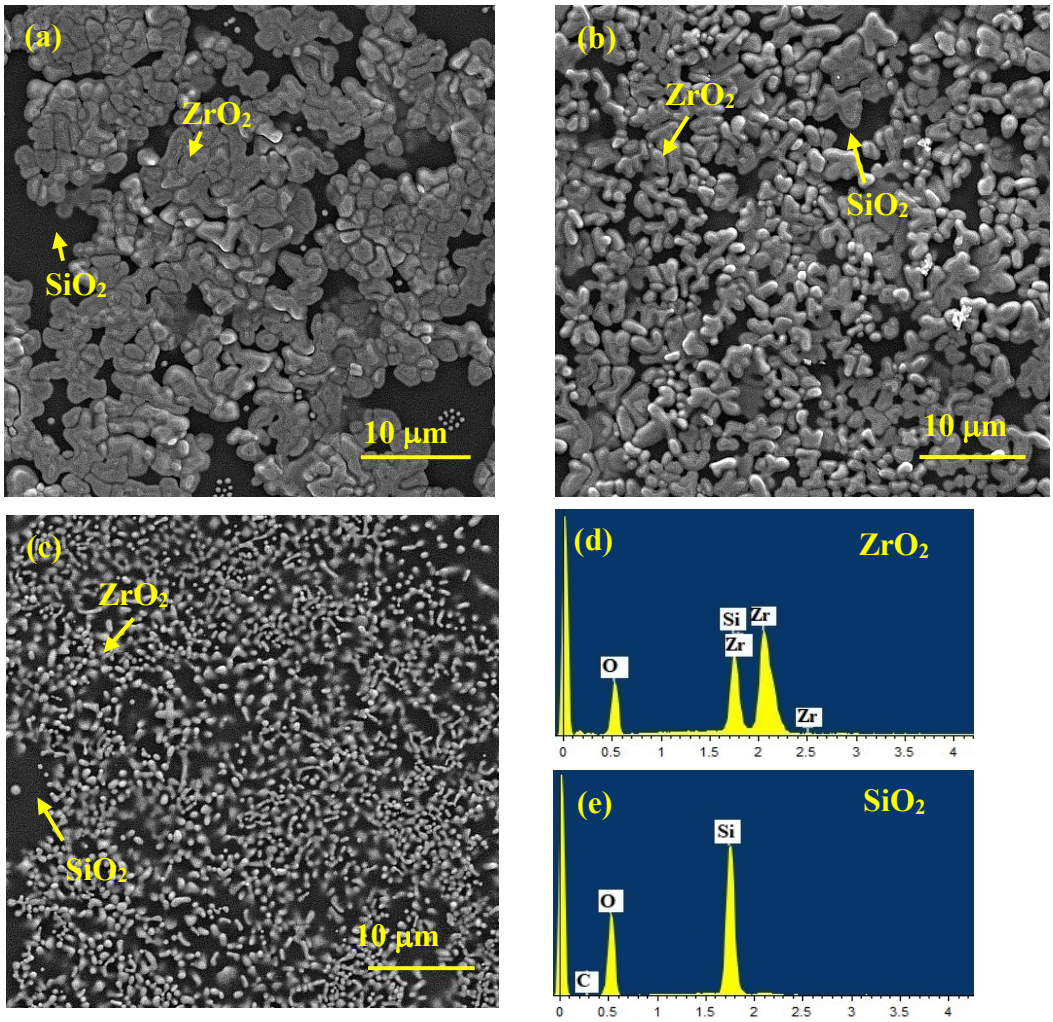

Figure 5.4 Surface morphology of (a) ZS-2.5SN, (b) ZS-5SN and (c) ZS-10SN after oxidation at 1500 °C for 10 h, it shows two distinct oxide phases (d) ZrO_2 and (e) SiO_2.

Figure 5.5 (a) shows XRD pattern of ZrB_2-20SiC-(2.5-10)Si_3N_4 composites oxidized surfaces (at 1500 °C). The oxidized ZS-SN composed of m-ZrO_2 and t- ZrO_2 phases. In particular, amount of t-ZrO_2 phase increased with increasing the Si_3N_4 content. The ZS-10SN composite shows more peak broadening background in the range of 20–30° (diffraction angle), which indicates presence of an amorphous phase. This type of patterns depends on two factors. Firstly, Zr is having a higher atomic number (Z=40) compared to Si (Z=14), due to this ZrO_2 is having higher atomic scattering which renders to stronger X-ray intensities. The second factor

is that relative amount of ZrO_2 at the surface exposed to X-ray is higher in ZS-2.5SN and ZS-5SN compared to ZS-10SN. On the other hand, intensity of zirconia peaks diminishes as the amount of Si_3N_4 increases, which confirms that amount of silica is high on the surface. The cross-sectional XRD of oxidized samples is presented in **Figure 5.5 (b)**. The presence of ZrB_2, SiC and ZrO_2 was noticed and the secondary phases were more prominent in ZS-10SN.

Coming to oxidation mechanisms of ZS-SN, the oxidation of ZrB_2 and ZrN phases lead to the formation of porous ZrO_2. However, the viscous liquid silica that was formed during oxidation of SiC subsequently fills the pores of ZrO_2 and thus presence of continuous layer without any pores and cracks can be observed. In ZS-10SN, relatively large amount of ZrN present along with ZrB_2 major phase when compared to other ZS composites. Therefore, more porous ZrO_2 expected for ZS-10SN and these pores subsequently filled by the liquid SiO_2. Hence, the thickness of oxide layer was high for ZS-10SN composite than ZS-2.5SN and ZS-5SN. The thickness of silica layer increases with increasing amount of Si_3N_4 without any spallation/discontinuity, which reduces oxygen diffusion. In fact, the oxygen diffusion coefficient in ZrO_2 ($\sim 10^{-10}$ m^2/s) is several orders higher in magnitude than SiO_2 ($\sim 10^{-21}$ m^2/s) at 1550 °C [287]. Hence, SiO_2 expected to show more inhibition to the oxygen diffusion when compared to ZrO_2. Overall it is noticeable that the ZS-SN composites exhibited good oxidation resistance as there is no evidence of SiC depleted layer. In the applications point of view, mechanical properties of UHTCs are also need to be considered. As the ZS-5SN measured with highest hardness, it is expected to be better choice material.

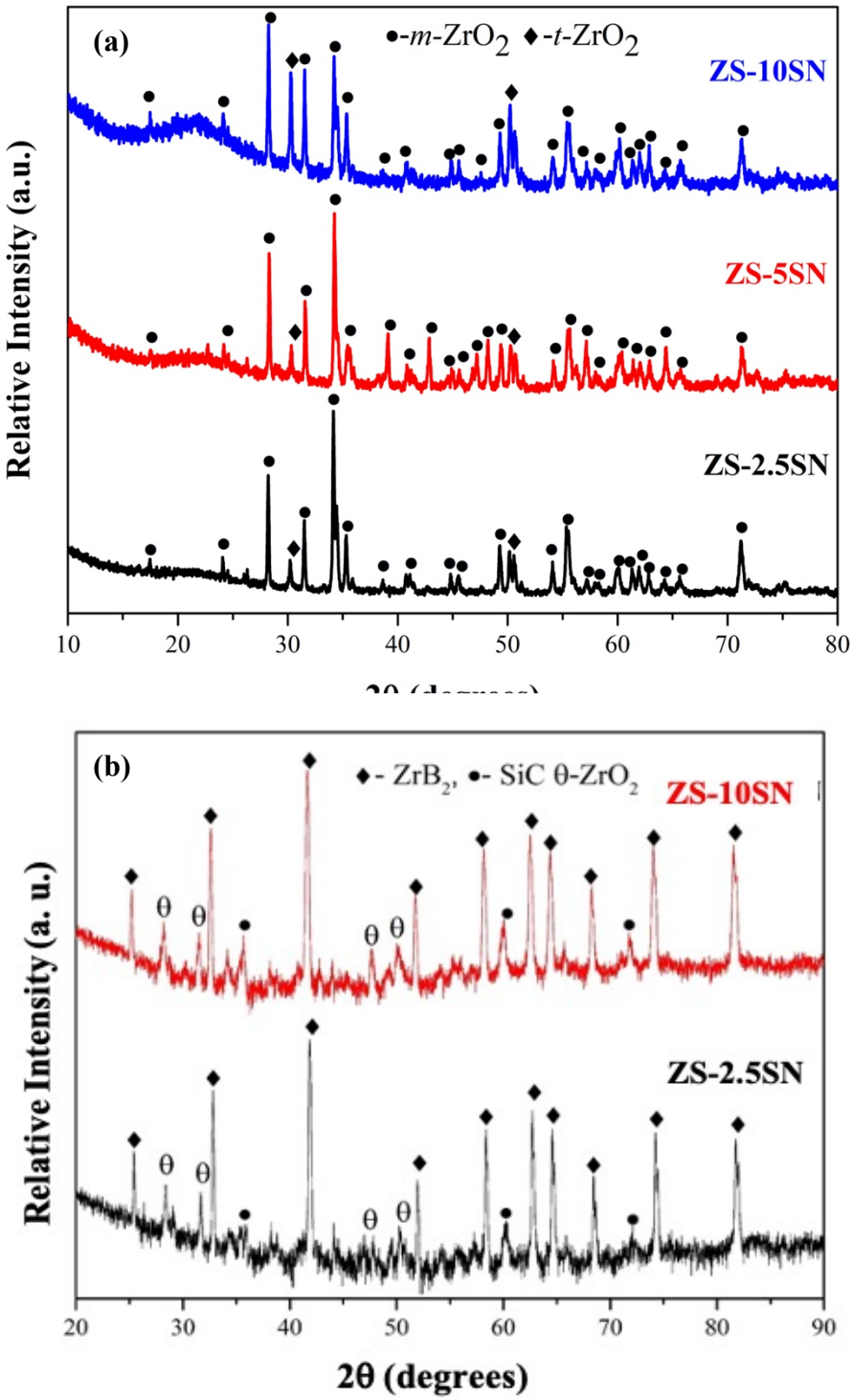

Figure 5.5 XRD of (a) Surface and (b) cross sectional oxidized ZrB_2-20SiC-(2.5-10)Si_3N_4 composites at 1500 °C for 10 h.

5.2 Oxidation behavior at 1600 °C

Further, the ZrB_2-20SiC-(2.5-10)Si_3N_4 composites were exposed to air at temperature of 1600 °C for 10 h. It is observed that ZS-2.5SN showed pores in the cross-sectional microstructure as shown in the **Figure 5.6**. It is observed that similar to previous oxidation studies ZrO_2 and SiO_2 phases were observed in the surface microstructure and in cross-section top SiO_2 layer, intermediate ZrO_2-SiO_2 layer and unreacted composite was observed. But, ZS-5SN was completely sticked to alumina boat after oxidation tests and it was difficult to evaluate weight measurements and oxide layer thickness.

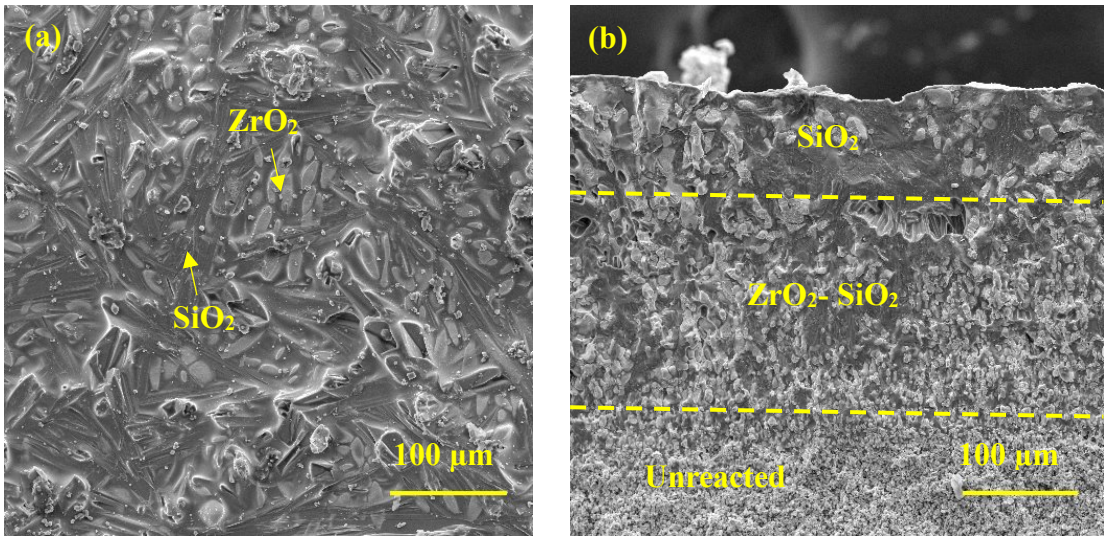

Figure 5.6 (a) surface (b) cross-sectional microstructure of ZS-2.5SN after oxidation at 1600 °C for 10 h.

On the other hand, for ZS-10SN sample weight gain was 15.25 mg/cm^2 and oxide layer thickness of 476 µm. The samples were oxidized according to the reactions from (45) to (50). The oxide layer consists of dense outer thick layer of SiO_2, ZrO_2-SiO_2 intermediate layer and unreacted bulk. The surface morphology of oxidized sample shows the phase of SiO_2 (dark) and ZrO_2 (bright) phases (**Figure 5.7**). The oxidation resistance of ZS-10SN is lower at 1600 °C compared to 1500 °C temperature conditions. The activity of the phases was higher at high temperature, due to that weight gain and oxide layer thickness was higher compared to ZS-10SN sample oxidized at 1500 °C.

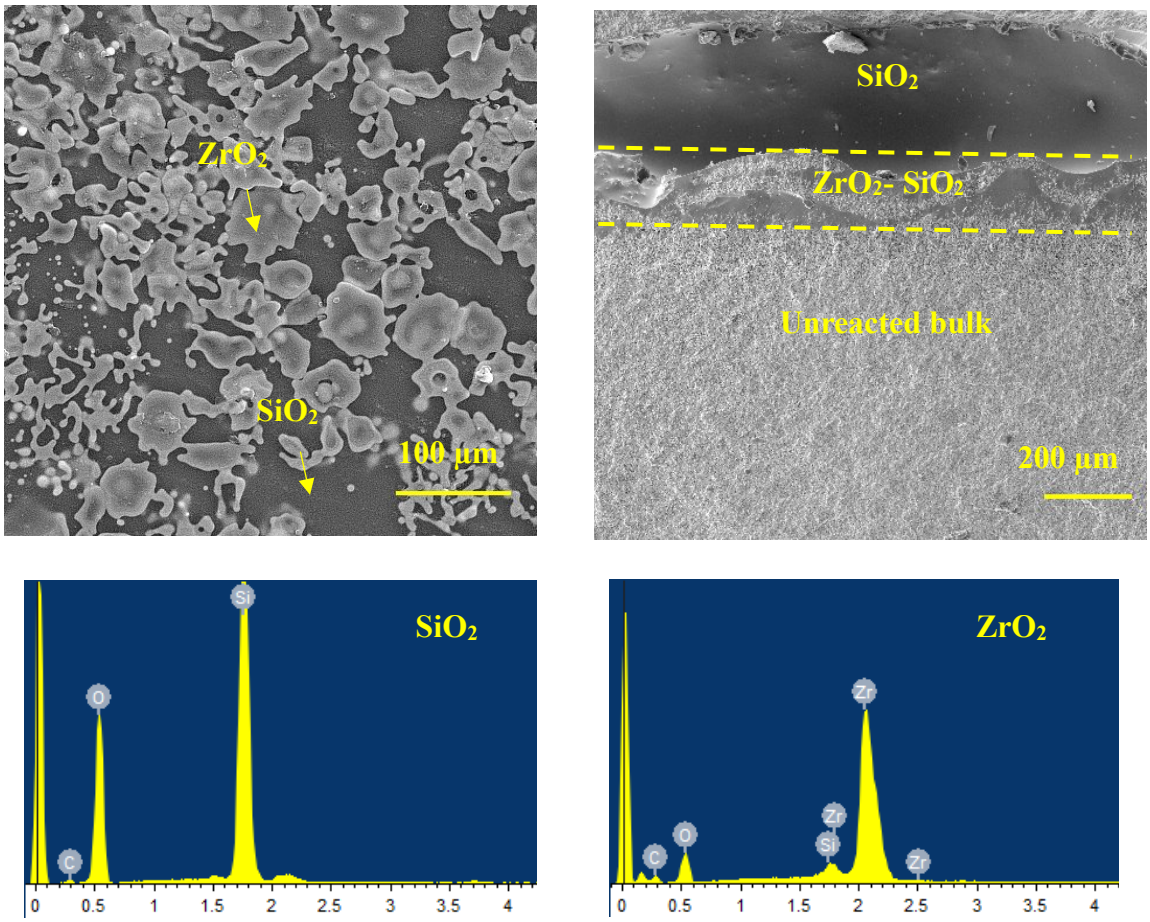

Figure 5.7 (a) surface (b) cross-sectional microstructure of ZS-10SN after oxidation at 1600 °C for 10 h.

Table 5.2 Comparison of processing conditions, microstructure and oxidation characteristics of different ZrB_2-based composites.

Composition (vol.%)	Sintered phases in ZrB_2 composites	Oxidation conditions (Temp.°C, Time h)	Weight gain (mg/cm^2)	Oxide layer thickness (µm)	Oxide phases	Ref.
ZS-2.5SN	ZrB_2, SiC, BN, ZrO_2	1500, 10	13.84	64	SiO_2, ZrO_2	pw
ZS-5SN	ZrB_2, SiC, BN, ZrO_2, ZrN	1500, 10	13.28	94	SiO_2, ZrO_2	pw
ZS-10SN	ZrB_2, SiC, BN, ZrO_2, ZrN	1500, 10	9.84	128	SiO_2, ZrO_2	pw
ZS-10SN	"	1600, 10	15.25	476	SiO_2, ZrO_2	pw
ZrB_2	ZrB_2	1300, 2	6.0	160	ZrO_2, B_2O_3	[200]
ZrB_2	ZrB_2	1500, 2	25.0	-	ZrO_2	"

ZrB_2-5 Si_3N_4	ZrB_2, $ZrSi_2$, BN, ZrN	1300, 2	14.0	140	ZrO_2	"
ZrB_2-5 Si_3N_4	ZrB_2, $ZrSi_2$, BN, ZrN	1500, 2	28.0	-	ZrO_2	"
ZrB_2-25 SiC	ZrB_2, SiC	1500, 2	5.0	-	SiO_2, ZrO_2	"
ZrB_2-20 SiC-15 Graphite	ZrB_2, SiC, C, ZrC	1800, 0.5, 2000 Pa (P_{O2})	22.0	-	m-ZrO_2, t-ZrO_2	[233]
ZrB_2-20SiC-40$MoSi_2$	ZrB_2, SiC, $MoSi_2$	1500, 10	3.0		SiO_2, ZrO_2, MoB, $ZrSiO_4$	[205]
ZS	ZrB_2, SiC	2200, 20 S in (30 vol.% H_2O+ 70 vol.% Ar)	-	291	SiO_2, ZrO_2	[255]
ZrB_2-5wt.% B_4C	ZrB_2, B_4C	1500, 5	16.2	775	ZrO_2	[86]
ZS	ZrB_2, SiC	1800, 1	15.0	-	SiO_2, ZrO_2	[289]
ZrB_2- 20SiC-5AlN	-	1800, 1	57.0	-	-	“
ZrB_2-20 $MoSi_2$	ZrB_2, $MoSi_2$	1500, 12	7.0	155	SiO_2, ZrO_2, MoB	[291]
ZrB_2-30 SiC	ZrB_2, SiC	1500, 0.5	0.5	13	ZrO_2, SiO_2	[225]
ZrB_2-30 SiC	ZrB_2, SiC	2000, 0.00277	-	30	m- ZrO_2	[208]
ZrB_2-20 SiC-20 ZrC	ZrB_2, SiC, ZrC	1600, 4	55.0	65	SiO_2, ZrO_2, ZrC_xO_y	[292]
Laminated BN/ZrB_2-SiC	ZrB_2, SiC, BN	1500, 10	10.0	-	SiO_2, ZrO_2	[288]
ZrB_2-10SiC_f-10$ZrSi_2$	ZrB_2, SiC, SiO_2, ZrO_2, $ZrSi_2$	1500, 10	12.7	65	SiO_2, ZrO_2	[199]

5.3 Summary

The weight gain of ZrB_2-20vol.% SiC composites decreased (from 13.84 to 9.84 mg/cm^2) and oxide layer thickness increased (64–128 μm) with increasing amount of Si_3N_4 from 2.5 to 10 vol.%. It is obvious that the oxidation resistance of ZrB_2-20vol.% SiC composites increased with the addition of Si_3N_4. The microstructure of oxidized samples surfaces after oxidation (at

1500 and 1600 °C for 10 h) consists of ZrO_2 and SiO_2 phases in all samples. The cross-sectional microstructure of oxidized ZS-Si_3N_4 composites consists of thick dense outer layer of SiO_2, intermediate (ZrO_2-SiO_2) layer and unreacted bulk.

Chapter 6

Effect of Ta addition on ZrB_2-20SiC composite

The present chapter discusses the effect of Ta addition on densification and microstructure and mechanical properties of ZrB_2-20vol.% SiC ceramic composite. ZrB_2-20vol.% SiC was MS-SPS with the addition of 2.5, 5 and 10wt.% Ta at 1900 °C, 50 MPa for 3 min.

6.1 Densification

Table 6.1 shows the densification and grain size of SPS ZrB_2-20vol.% SiC-(2.5-10)wt.% Ta composites. The sintered density of ZrB_2-20SiC-Ta composites increased from 5.56 to 5.87 g/cc, it was mainly due to the increasing addition of high-density Ta to ZrB_2-20vol% SiC (ZS). Irrespective of the amount of Ta addition, all the samples could be densified to more than 99%ρ_{th} or relative density. It shows that the selected SPS parameters are suitable sintering conditions for obtaining full density of ZS-Ta composites. The RD of samples were estimated by measuring the residual porosity from the SEM micrographs using ImageJ software. The low magnification SEM images show hardly any traces of porosity and indicates its full density.

Table 6.1 Relative density, grain size and lattice parameters of ZrB_2 and $(Zr,Ta)B_2$ solid solution with varying amount of tantalum addition.

Sample Id	RD	Core size (μm)	Rim size (μm)	ZrB_2		$(Zr,Ta)B_2$	
				c (A°)	a (A°)	c (A°)	a (A°)
ZS-2.5Ta	99.11	2.76±0.11	4.17±0.10	3.5314	3.1523	-	-
ZS-5Ta	99.11	2.84±0.08	4.13±0.14	3.5299	3.1655	3.3386	3.2075
ZS-10Ta	99.63	2.65±0.09	3.61±0.11	3.5304	3.1612	3.4640	3.1494

6.2 Phase and microstructure evolution

It is noticed that the dark contrasting phase (SiC) uniformly dispersed in the matrix phase. A closer look at the microstructure reveals core and rim structure of the matrix phase. As it was recorded in **Table 6.1**, the size of ZrB_2 core (2.65–2.84 μm) and $(Zr,Ta)B_2$ rim (3.61–4.17 μm) varied narrowly. At the sintering temperature, Ta dissolves into ZrB_2 matrix and forms the

$(Zr,Ta)B_2$ solid solution rim phase. As the amount of Ta increases, the amount of solid solution phase increases, which controls the growth of ZrB_2 grains. The ZrB_2 grain size after sintering remains more or less similar to that of starting ZrB_2 powders size (avg. particle ZrB_2 size ~2.5 μm). From **Table 6.1**, it also should be clear that the lattice spacing of the ZrB_2 core and $(Zr,Ta)B_2$ rim were varying and is due to the elastic and thermal mismatch during cooling from the sintering temperature.

ZS with varying amounts of Ta show microstructural phases such as ZrB_2, $(Zr,Ta)B_2$ and SiC; and the boride matrix exists as "core-rim" structure, in which grains are comprised of ZrB_2 core surrounded by an isostructural $(Zr,Ta)B_2$ rim solid solution phase (**Figure 6.1**). **Figure 6.1 (d)** shows high magnification image of ZS-5Ta sample with EDS elemental analysis. It depicts ZrB_2, $(Zr, Ta)B_2$, SiC and small fraction of bright (Zr,Ta)C phases, which was confirmed by EDS. The X-ray diffraction pattern of the as-sintered ZrB_2-based composites is shown in **Figure 6.2**. The XRD revealed the presence of ZrB_2, $(Zr,Ta)B_2$, SiC major crystalline phases along with minor amounts of ZrO_2 and (Zr,Ta)C phases. In ZS-5Ta and ZS-10Ta samples, some peaks of monoclinic ZrO_2 were observed which were formed due to pickup of oxygen during handling. In fact, similar observation of ZrO_2 phase formation was reported by other researchers as well [158], [294]. In case of ZS-5Ta and ZS- 10Ta samples, other phase was clearly observable at the right side of ZrB_2 peaks, which was identified as hexagonal $(Zr,Ta)B_2$ solid solution phase with reduced unit cell parameters. This phase was observed in ZS-2.5Ta sample at higher diffraction angle of 80°. The lattice parameters of ZrB_2 and $(Zr,Ta)B_2$ solid solution are reported in **Table 6.1**. The c/a ratio of the solid solution was smaller than ZrB_2. It indicates the contraction of the unit cell, due to the smaller atomic radius of tantalum (0.143 nm) compared to zirconium (0.160 nm). So, according to the Bragg's law, the diffraction peaks of solid solution phase shifted towards higher angles (right side), as is shown in **Figure 6.2 (b)**.

Monteverde also reported change in the lattice parameters of core and rim structure of ZrB_2-2.3$MoSi_2$ and ZrB_2-15SiC-2$MoSi_2$ (vol.%) [295]. The core-rim structure in those composites was observed due to the reaction between $MoSi_2$ and surface oxides of ZrB_2. The rim was composed of (Zr,Mo)B_2 solid solution phase. The ZrB_2 core and (Zr,Ta)B_2 rim structure was also reported for ZrB_2-15vol.% $TaSi_2$ and ZrB_2-20SiC-(0–10)$TaSi_2$ (vol.%) composites [158], [251]. In another work, Hu et al. studied the microstructure and properties of spark plasma sintered ZrB_2-(10–30)SiC-(10–20)$TaSi_2$ (vol.%) [294]. Interestingly, the core-rim structure was observed for the ZrB_2-based composites that were SPS at 1600 °C and no such structure was present when the SPS was carried out at higher temperature of 1800 °C [294]. The formation of core-rim structure was also evidenced for WSi_2, however, no such core-rim structure was observed for ZrB_2-15vol.% $ZrSi_2$ [240]. Only the presence of (Zr, TM)B_2 solid solution phase was noticed when ZrB_2 was added with small amount (1-1.2wt.%) of transition metals after hot pressing at 2150 °C, 32 MPa for 10 min [296]. It is mainly because of dissolution of the transition metals (Hf, Nb, W, Ti, Y) in to ZrB_2. Recently, Dorner et al. also observed (Zr,Ta)B_2 solid solution phase in ZrB_2-3at.% Ta and ZrB_2-6at.% Ta after hot pressing at 2200 °C, 32 MPa for 30 min [297]. From this discussion it should be clear that the type of additive, its amount and processing conditions influence the microstructure of ZrB_2-based composites.

The fracture surfaces of SPS ZrB_2-SiC-Ta composites is presented in **Figure 6.3**. It shows a combination of intergranular and transgranular fracture mode with good bonding between the grains without any hint of pores.

6.3 Mechanical properties

ZrB_2-20SiC-(2.5-10)Ta composites mechanical properties were evaluated using Vickers hardness at 2 Kg load and nano-indentation hardness test as well (at 450 mN). **Table 6.2** shows the nanoindentation results and it is also compared with literature. The nano-indentation hardness of 16.81, 15.23 and 18.62 GPa was measured for ZS-2.5Ta, ZS-5Ta and ZS-10Ta

samples, respectively. Additionally, the bulk hardness of ZrB_2 composites was measured using the Vickers hardness and almost similar trend and hardness of 16.62, 15.59 and 17.75 GPa was measured for ZS-2.5Ta, ZS-5Ta and ZS-10Ta samples, respectively. It indicates that both the nanoindentation results and Vickers hardness values are more or less the same. The hardness values were relatively high for ZS-10Ta composition due to core-rim structure and presence of (Zr,Ta)C phase. On the other hand, ZS-5Ta composition achieved lower hardness due to the presence of ZrO_2 phase. Dorner et al. also observed that ZrB_2-3at.% Ta composite achieved lower hardness due to the presence of ZrO_2, which is having lower hardness of 12 GPa [297]. Interestingly, the ZrB_2-6at.% Ta exhibited higher hardness than ZrB_2-3at.% Ta. **Table 6.2** shows the densification and mechanical properties of different ZrB_2-based composites. In case of Ni (up to 8 mol.%) added ZrB_2-25mol.% SiC, there was tendency of slight decrease in hardness and hardness [298]. The elastic modulus of ZrB_2-20SiC-(2.5-10)Ta composites varied between 341.1 and 451.6 GPa and exhibited similar trend as that of hardness. In particular, the ZS-10Ta composite exhibited maximum elastic modulus value. From the **Table 6.2**, phase pure ZrB_2 reported with maximum hardness (30.2 GPa) and elastic modulus (582 GPa) and is attributed to its fine grain structure [299]. It was observed that the addition of Ta lowered the elastic modulus of ZrB_2 [297]. In case of ZrB_2 composites (without addition of any transition metal), the hardness and elastic modulus varied in the range of 14.73-20.2 GPa and 295-373 GPa, respectively. However, the transition metal added ZrB_2-SiC composites reportedly varied hardness between 18.6 and 19.4 GPa and elastic modulus between 440 and 453 GPa. It infers that addition of additives significantly affecting the mechanical properties of ZrB_2.

Figure 6.4 (a) shows the indentation force vs displacement curves for ZrB_2-20SiC-(2.5-10)Ta samples. The indentation depth is increased with decreasing amount of tantalum. The indentation depth of ZS-5Ta and ZS-10Ta samples were similar (~671 nm), but ZS-2.5Ta have the indentation depth of 721 nm. **Figure 6.4 (b)** shows the variation of hardness and elastic modulus as a function of amount of Ta addition to ZrB_2-20vol.% SiC. It is observed that with

10wt.% tantalum addition ZrB_2-20vol.% SiC achieved highest hardness and elastic modulus due to core-rim structure in microstructure. With ZS-5Ta, it is observed that lowest hardness and elastic modulus due to presence residual oxide phase (ZrO_2) and conversely even though there is presence of ZrO_2 phase in ZS-10Ta, the presence of additional (Zr,Ta)C phase in the microstructure resulted in highest hardness and elastic modulus values. It is to be noted that ZrO_2 (12 GPa) [23] shows less hardness compared to (Zr,Ta)C (~26 GPa) [300] phases. The relative amount of (Zr,Ta)C phase in ZS-5Ta and ZS-10Ta samples were calculated using ImageJ software from the microstructures. It is observed that ~0.11vol.% and ~2.2vol.% amounts of (Zr,Ta)C phase was observed in ZS-5Ta and ZS-10Ta samples, respectively. Hence ZS-10Ta composite exhibited relatively high hardness and elastic modulus values due to the presence of hard (Zr,Ta)C phase. It is observed that ZrB_2-20SiC-Si_3N_4 showed good hardness compared to ZrB_2-20SiC-Ta due to the formation of high hardness secondary phases.

Table 6.2 Comparison of densification and mechanical properties of ZrB_2-20SiC-(2.5-10)Ta composites with the other ZrB_2 composites reported in the literature. (pw: represents present work)

Composition	**Sintering conditions (°C, MPa, min)**	**Relative density**	**Hardness (GPa)**	**Elastic modulus (GPa)**	**Ref.**
ZS-2.5Ta	SPS, 1900, 50, 3	99.11	16.81±1.95	445.5±82.0	pw
ZS-5Ta	SPS, 1900, 50, 3	99.11	15.23±0.95	341.1±18.2	pw
ZS-10Ta	SPS, 1900, 50, 3	99.63	18.62±1.36	451.6±24.2	pw
ZrB_2-25vol.%SiC-5wt.% graphite	SPS, 1800, 35, 8	100	14.73	295	[301]
ZrB_2-25mol.% SiC	SPS, 1700, 40, ~7	92.4	~20.2	~453	[298]

ZrB_2-25mol.% SiC–2mol.% Ni	SPS, 1700, 40, ~7	92.7	~19.4	~440	“
ZrB_2-25mol.% SiC–4mol.% Ni	SPS, 1700, 40, ~7	93.3	~18.7	~447	“
ZrB_2-25mol.% SiC–6mol.% Ni	SPS, 1700, 40, ~7	94.1	~18.6	~443	“
ZrB_2-25mol.% SiC–8mol.% Ni	SPS, 1700, 40, ~7	94.7	~18.6	~440	“
ZrB_2-0.5vol.%SiC	SPS, 1500, 40, 10	90	16.79	373.29	[197]
ZrB_2	RSPS, 1200, 100, 10	98.4	30.2	582	[299]
ZrB_2-3at. % Ta	RHP, 2200, 32, 30	99.2	-	510.4	[297]
ZrB_2-6at. % Ta	RHP, 2200, 32, 30	99.0	-	531	“

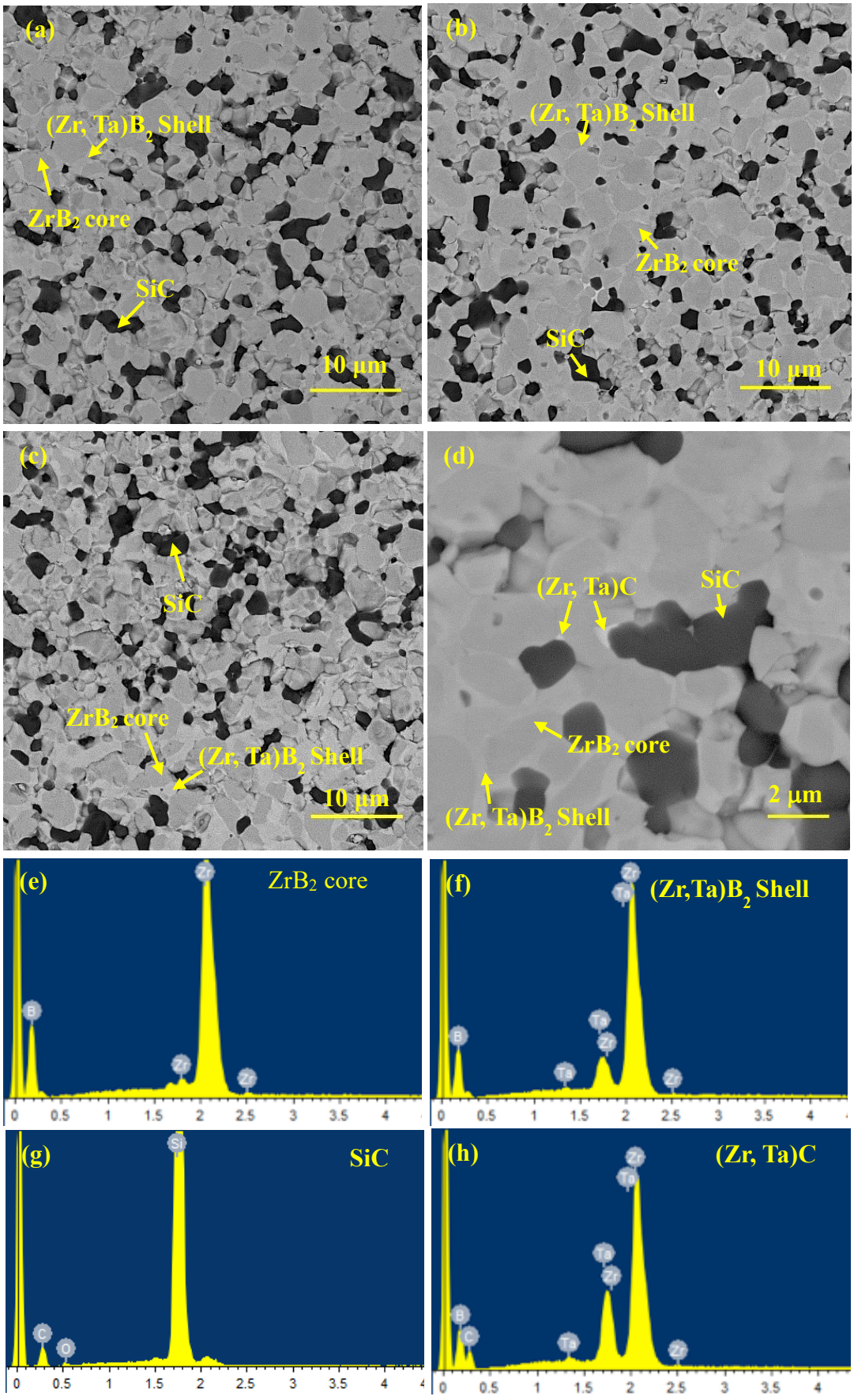
(a)
(Zr, Ta)B2 Shell
ZrB2 core
SiC
10 μm
(b)
(Zr, Ta)B2 Shell
ZrB2 core
SiC
10 μm
(c)
SiC
ZrB2 core
(Zr, Ta)B2 Shell
10 μm
(d)
(Zr, Ta)C
SiC
ZrB2 core
(Zr, Ta)B2 Shell
2 μm
(e)
ZrB2 core
(f)
(Zr,Ta)B2 Shell
(g)
SiC
(h)
(Zr, Ta)C

Figure 6.1 Microstructures of multi-stage spark plasma sintered (a) ZS-2.5Ta, (b) ZS-5Ta, (c) ZS-10Ta and (d) ZS-5Ta at high magnification showing the different phases with EDS elemental analysis (e, f, g and h).

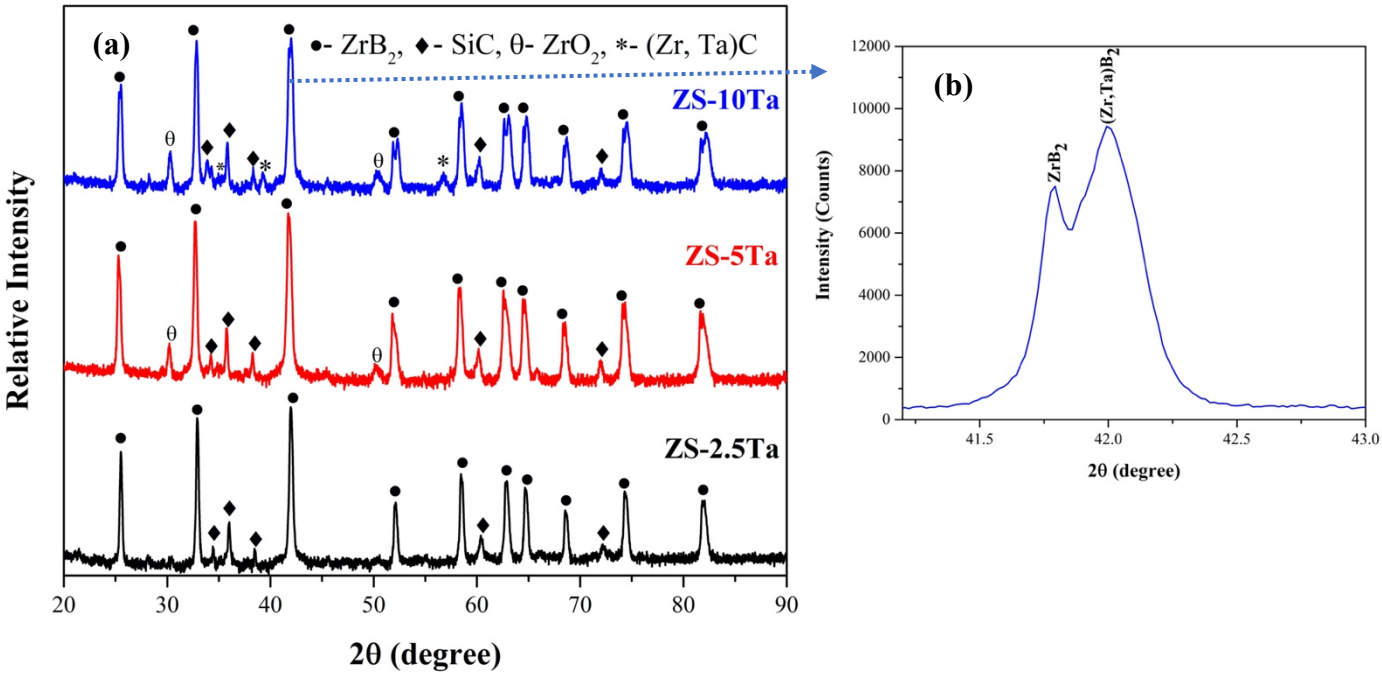

Figure 6.2 XRD patterns of spark plasma sintered (a) ZrB_2-20SiC-(2.5-10)Ta composites (b) showing peak shifts, which confirms the solid solution formation (example: ZS-10Ta).

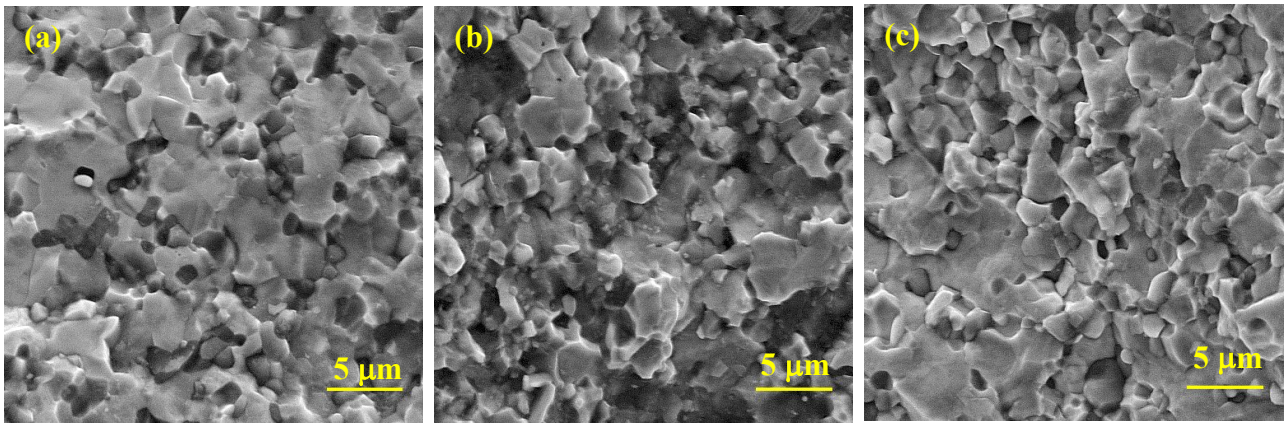

Figure 6.3 SE images of fracture surfaces of (a) ZS-2.5Ta, (b) ZS-5Ta and (c) ZS-10Ta sample.

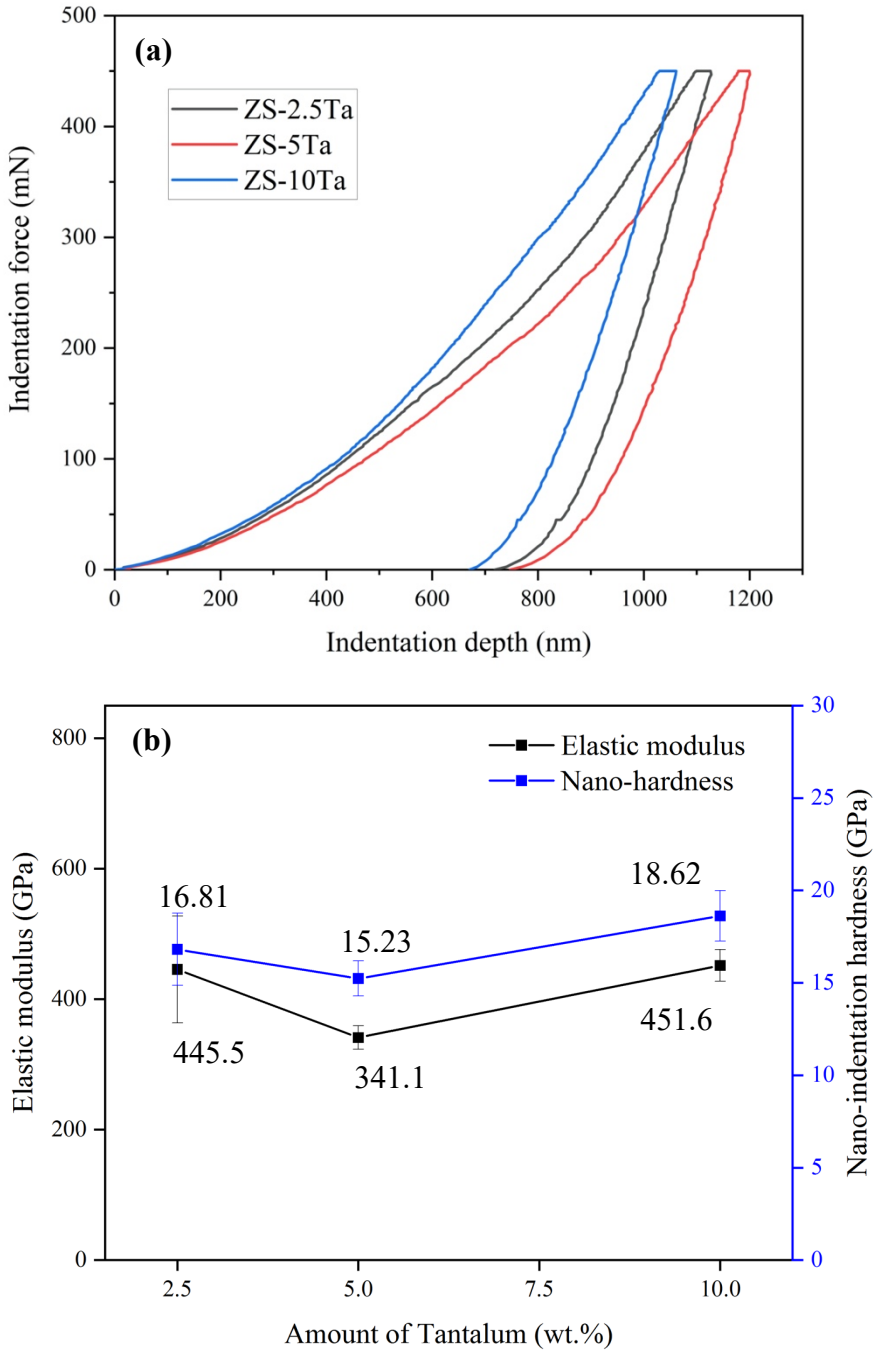

Figure 6.4 (a) Indentation force vs depth curves obtained from nano-indentation instrument and (b) the variation of nano-indentation hardness and elastic modulus of ZrB_2-20SiC-(2.5-10)Ta composites.

6.4 Summary

More than 99% theoretical density was achieved for ZrB_2-20vol.% SiC-Xwt.% Ta (X=2,5, 5 and 10) composites after spark plasma sintering at 1900 °C, 50 MPa for 3 min. The microstructure of sintered samples consists of ZrB_2 core, (Zr,Ta) B_2 rim, SiC as major

crystalline phases and minor amounts of ZrO_2 and (Zr,Ta)C phases. The highest nano-indentation hardness (18.62 GPa) and elastic modulus (451.60 GPa) was achieved for ZS-10Ta composition.

Chapter 7

Oxidation studies of ZrB_2-20SiC-(2.5-10)Ta composites

The present chapter discusses the oxidation behavior of ZrB_2-20SiC-(2.5-10)Ta composites at different oxidation temperatures of 1500 and 1600 °C for 10 h.

7.1 Oxidation behavior at 1500 °C

The weight gain and oxide layer thickness of the samples with respect to the amount of tantalum addition after oxidation at a temperature of 1500 °C for 10 h are presented in **Table 7.1**. The oxidation properties of different ZrB_2-based composites reinforced with transition metal silicides, carbides or transition metals are also included for comparison purpose in the **Table 7.1** [195], [200], [247], [249], [257], [302]. The weight gain and oxide layer thickness were reduced with increasing amount of tantalum. The total oxide layer thickness of the composites was measured using cross-sectional SEM images of oxidized samples. From **Table 7.1** it can be realized that the weight of Ta added ZrB_2-20vol.% SiC composites decreased from 22.91 to 18.77 mg/cm^2 after isothermal oxidation at 1500 °C. Likewise, the oxide layer thickness (based on the SEM of the cross-sectional oxidation samples) of the ZrB_2-SiC composites also decreased considerably from 401 to 195 μm with the addition of Ta. It indicates the usefulness of Ta in improving the oxidation resistance of ZS.

The reduction in the weight of oxidized samples with increasing amount of tantalum is due to either evaporation of gaseous phases at the oxidation temperature or less diffusion of oxygen into the surface of the sample. The Ta addition to ZrB_2-SiC composite may help to develop immiscibility in the top passive layer, which has a higher melting point and retards the diffusion of oxygen and thereby no chance of evaporation of silica at 1500 °C. The oxide layer thickness also decreases with increasing amount of tantalum due to passive behavior of the top silica layer, which retards the diffusion of oxygen further into the surface. It also observed that as the amount of tantalum increases the thickness of the middle layer decreases due to the protective nature of the top silica layer.

Figure 7.1 shows the XRD of the ZrB_2 sample surfaces after oxidation at 1500 °C for 10 h. The presence of monoclinic ZrO_2 and orthorhombic $TaZr_{2.75}O_8$ crystalline phases on the ZrB_2 samples. It is evident that $TaZr_{2.75}O_8$ phase in ZrB_2 samples increased with more amount of Ta addition. Peak broadening at about 22° indicate presence of amorphous SiO_2. The SEM-EDS oxidized ZrB_2 samples can be seen in **Figure 7.2**. Spherical and dendritic ZrO_2, dark SiO_2 matrix phase and coarse spherical $TaZr_{2.75}O_8$ were noticeable on the oxidized ZrB_2-based composites. It is also observed that as the amount of Ta increases, ZrO_2 grains transformed from spherical to dendritic shape. The presence of ZrO_2, SiO_2 and $TaZr_{2.75}O_8$ phases were confirmed by EDS. The formation of $TaZr_{2.75}O_8$ phase can be attributed to oxidation reactions (51) and (52). The thermodynamic feasibility of these reactions was possible at the temperature of 1500 °C [240], [303], [304].

Further the cross-sectional SEM of ZrB_2-20SiC-(2.5-10)Ta composites was carried out to understand the oxide layer presence in the samples (**Figure 7.3**). It is evident that all the ZrB_2 samples consists of three different layers: thick and dense outer SiO_2 layer, intermediate SiC depleted layer and unreacted bulk. The thickness of oxide layer decreased considerably with higher amount of Ta addition to ZrB_2-20vol.% SiC. The SEM-EDS of cross-sectional SEM-EDS of ZS-10Ta sample after oxidation is presented in **Figure 7.4**. The EDS analysis from all the three layers clearly confirms the presence of SiO_2, SiC-depleted layer and unreacted bulk in the oxidized samples. It is interesting to note the presence of SiC depleted layer even though there is no indication of any defect presence at or near the external SiO_2 layer.

During oxidation, initially ZrO_2 and B_2O_3 forms due to the oxidation of ZrB_2 in the temperature range of 800–1200 °C. In particular, B_2O_3 is protective at low temperatures and the evaporation of B_2O_3 starts at temperatures higher than 1100 °C and left porous ZrO_2.

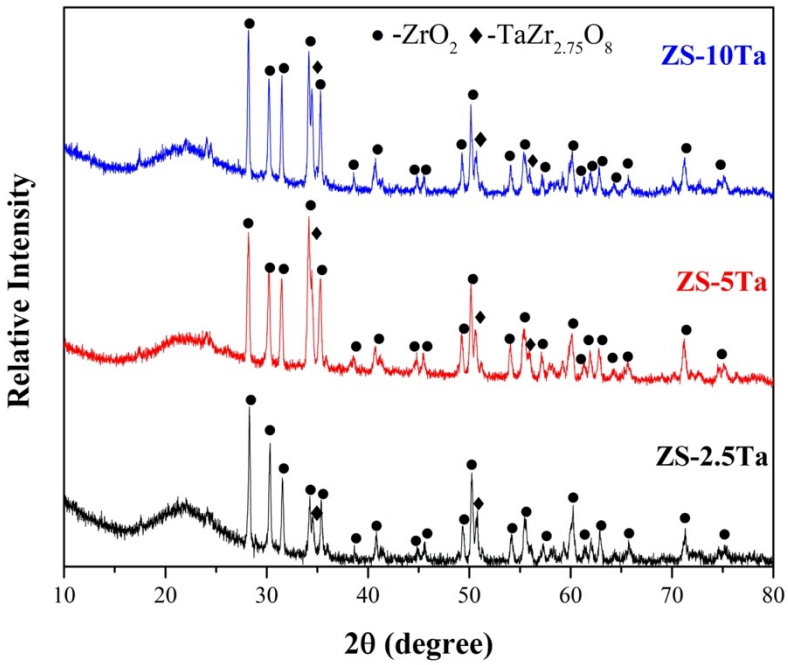

Figure 7.1 XRD patterns of tantalum (2.5, 5 and 10wt.%) added ZrB_2-20vol.% SiC composites after oxidation at 1500 °C for 10 h.

When temperature reaches to 1500 °C, the outer oxide scale composition changes significantly. Due to high vapor pressure, B_2O_3 evaporates and SiC oxidized to form SiO_2, which protects the composite from further oxidation. The SiO_2 scale formed on ZrB_2-SiC composite, which is stable at high temperatures than the boria layer formed because of low volatility of liquid silica glass compared to boria at these conditions. The overall oxidation of ZrB_2-SiC composites takes place by the oxidation reactions (45) to (48).

$$SiC\ (s) + 2SiO_2\ (l) = 3SiO\ (g) + CO(g) \qquad (51)$$

During prolonged holding (10 h) at the oxidation temperature of 1500 °C, SiO (g) forms by the oxidation (via reaction 48 and 51) and thus it leads to the formation of SiC depleted layer. The observation of SiC depleted layer has been reported by several researchers for ZrB_2-SiC composites [237]. Interestingly, the presence of SiC depleted layer was evidenced for graphite, $TaSi_2$, TaB, TiB_2 reinforced ZrB_2-SiC composites [193], [237], [251], [254], [257], [289], [305]. However, the La_2O_3, LaB_6, WC and Si_3N_4 added ZrB_2-SiC composites did not show any indication of SiC depleted layer [220], [289], [306], [307]. Depending on the

oxidation conditions the SiC-depletion was reported for ZrB_2-SiC-LaB_6 conditions [289], [308].

As mentioned above, the SiO_2 layer thickness decreased with increasing the amount of tantalum to ZrB_2-SiC. The possible reason for decreasing the SiO_2 layer thickness due to glass immiscibility developed by Ta cations in liquid silica. Silvestroni and Kleebe proposed the Ta presence improves efficacy of oxidation resistance of ZrB_2-15$TaSi_2$ due to increased cation field strength by promoting glass immiscibility and retards the diffusion of oxygen [251]. In case of ZrB_2-15vol.% $TaSi_2$ composites, it was reported that ZrO_2, $TaZr_{2.75}O_8$ and TaB_2 phases present after oxidation at 1500 °C and ZrO_2, $TaZr_{2.75}O_8$ and Ta_2O_5 phases at oxidation temperature of 1650 °C for 15 min in air [251]. The formation of Ta_2O_5 phase inside ZrO_2 grains develops the cracks and spallation of the oxide layer from the inner bulk, which reduces the oxidation resistance at above 1650 °C. Nevertheless, TaB_2 and Ta_2O_5 phases were not detected in this current work, instead of that $TaZr_{2.75}O_8$ was observed due to continuous oxidation for 10 h.

In a different work, presence of ZrO_2 and $TaZr_{2.75}O_8$ phases were observed in oxidized ZrC-$TaSi_2$ composites [303], [304]. However, Levine et al. observed only ZrO_2 and SiO_2 phases in oxidized (at 1627 °C for 10 min) ZrB_2-20vol.% $TaSi_2$ composite without any traces of tantalum containing phases [305]. He et al. studied the effect of Yttrium (Y) addition on the oxidation behavior of ZrB_2-SiC composite [195]. The Y dissolved in the silica layer, thereby it has improved oxidation resistance of the ZrB_2-based composites by forming $Y_2Si_2O_7$ phase. Dehdashti et al. studied the effect of Mo, W and Nb addition on the oxidation behavior of monolithic ZrB_2 ceramic [309]. The thickness of oxide layer is above 300 μm for Mo, W and Nb reinforced ZrB_2 after oxidation at 1600 °C for 3 h.

The oxidation properties of different ZrB_2-based composites are compared in the **Table 7.1**. The weight (4.3–0.8 mg/cm^2) and oxide layer thickness (52.98–5.97 μm) of $TaSi_2$ reinforced ZrB_2-20SiC decreased after oxidation at 1627 °C for 1.6 h [257]. The improvement

in the oxidation resistance was attributed to glass immiscibility and high viscosity of glass with Ta. Similarly, the addition of $TaSi_2$ also considerably lowered the weight (44–9 mg/cm^2) and oxide layer thickness (300–60 μm) of ZrB_2 after oxidation at 1400/1500 °C for 2 h [200]. The addition of Yttrium to ZrB_2-30SiC also reduced its weight (32.5–24.5 mg/cm^2) and oxide layer thickness (500–200 μm) after oxidation at 1700 °C for 1 h [195]. A comparison of present work results with the literature data indicates the usefulness of Ta in improving oxidation resistance of ZrB_2-20SiC. Since the oxidation test conditions and materials compositions are different, the underlying oxidation mechanisms will be different.

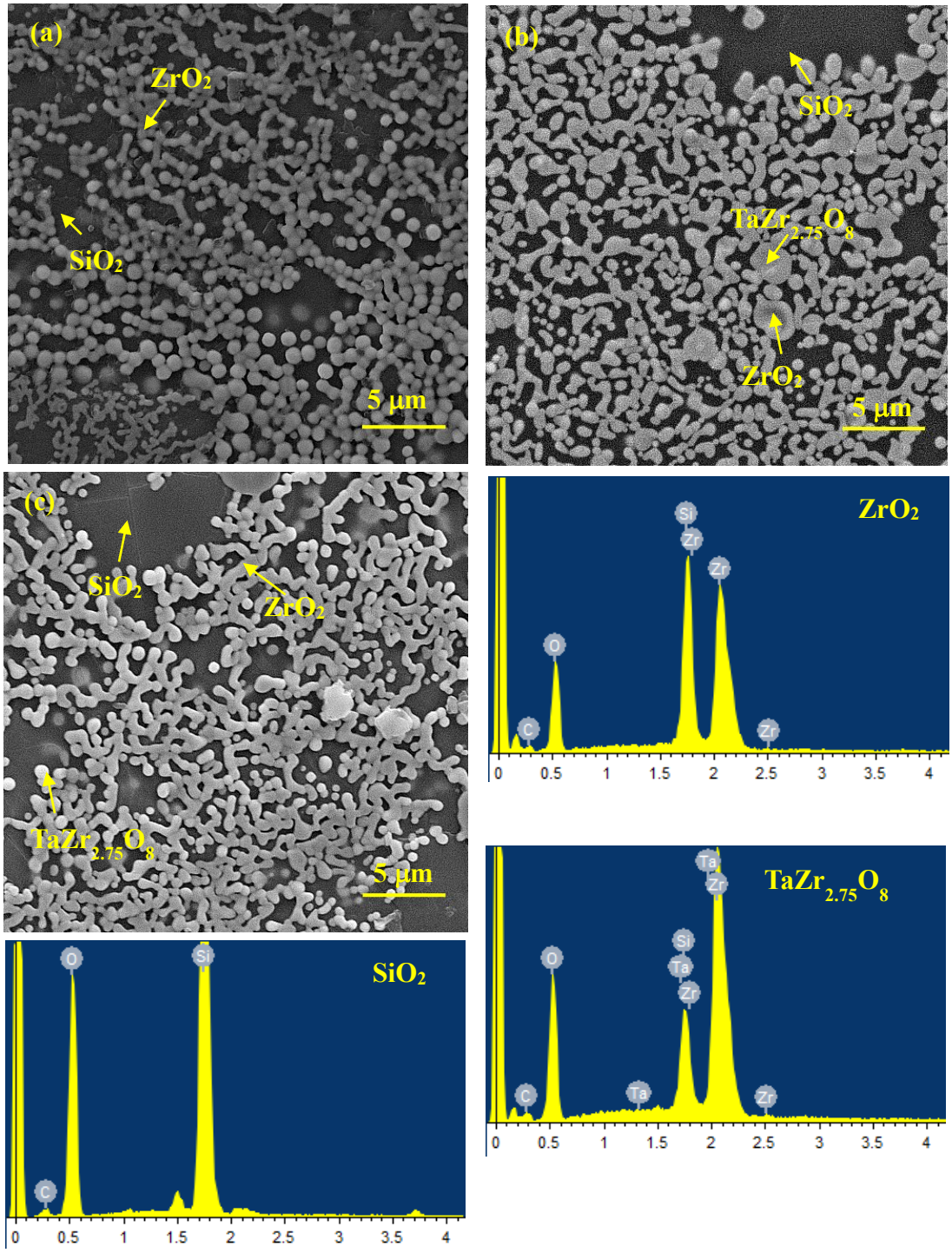

Figure 7.2 Surface morphology of (a) ZS-2.5Ta, (b) ZS-5Ta and (c) ZS-10Ta samples after oxidation at 1500 °C for 10 h.

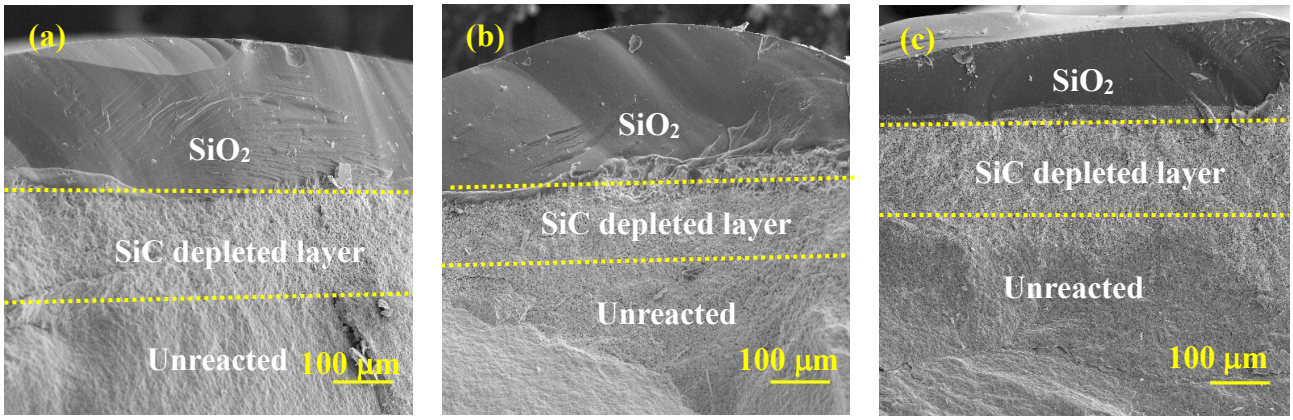

Figure 7.3 Cross-sectional SEM of (a) ZS-2.5Ta, (b) ZS-5Ta and (c) ZS-10Ta samples after oxidation at 1500 °C for 10 h.

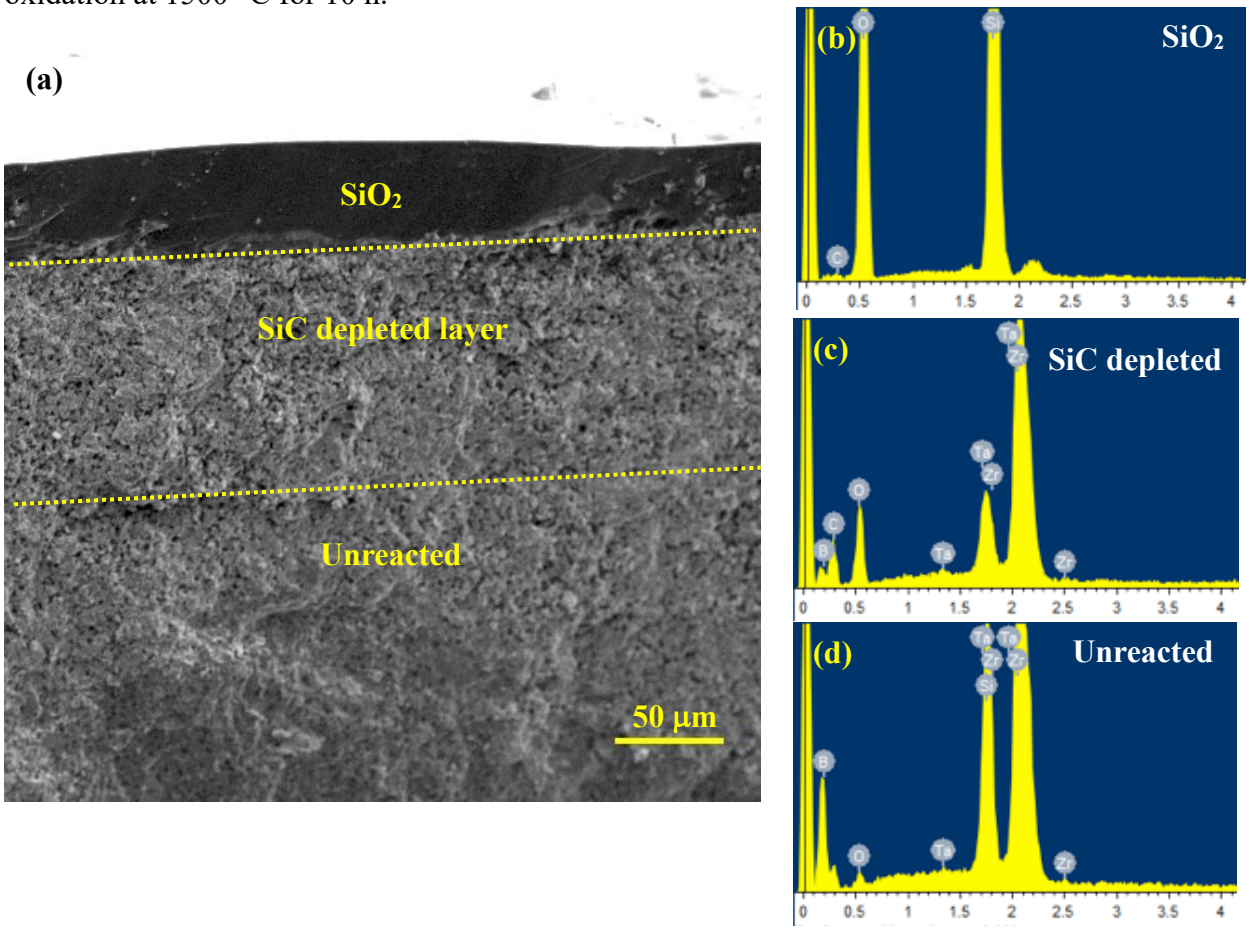

Figure 7.4 (a) Cross-sectional SEM-EDS of ZS-10Ta sample after oxidation at and 1500 °C for 10 h and (b), (c) and (d) showing EDS spectra of top (SiO_2), middle (SiC-depleted layer) and unreacted bulk.

Table 7.1 Specific weight gain and oxide layer thickness of ZrB_2-20SiC-(2.5-10)Ta composites and its comparison with the literature data. (pw: represents present work)

Composition	**Oxidation conditions (°C, h)**	**Mass gain (mg/cm^2)**	**Oxide layer thickness (μm)**	**Oxide phases**	**Ref**
ZS-2.5Ta	1500, 10	22.91	401	SiO_2, ZrO_2, $TaZr_{2.75}O_8$	pw
ZS-5Ta	1500, 10	19.15	384	″	pw
ZS-10Ta	1500, 10	18.77	195	″	pw
ZS-2.5Ta	1600, 10	21.04	320	″	pw
ZS-5Ta	1600, 10	17.45	303	″	pw
ZS-10Ta	1600, 10	16.65	255	″	pw
ZrB_2-6mol.% Nb	1500, 3	-	79	ZrO_2, $Nb_2Zr_6O_7$	[258]
ZrB_2-4mol.% W	1600, 5 min	2.0	30	ZrO_2	[247]
ZrB_2-6mol.% W	1600, 5 min	1.9	28	ZrO_2	″
ZrB_2-8mol.% W	1600, 5 min	2.3	26	ZrO_2	″
ZrB_2-30vol.% SiC-2wt.% Y	1700, 1	32.5	500	ZrO_2, SiO_2	[195]
ZrB_2-30vol.% SiC-7wt.% Y	1700, 1	24.5	200	ZrO_2, SiO_2, $Y_2Si_2O_7$	″
ZrB_2-20vol.% SiC	1627, 1.66	4.3	53	ZrO_2, SiO_2	[257]
ZrB_2-15vol.% $TaSi_2$	1500, 0.25	-	68	ZrO_2, SiO_2, $TaZr_{2.75}O_8$	[251]
ZrB_2-15vol.% $TaSi_2$	1600, 0.25	-	500	ZrO_2, Ta_2O_5, $TaZr_{2.75}O_8$	″
ZrB_2-10vol.% $TaSi_2$	1500, 2	44	-	ZrO_2, $TaZr_{2.75}O_8$	[200]

7.2 Oxidation behavior at 1600 °C

The oxidation behavior of the ZrB_2-20SiC-(2.5-10)Ta composites were evaluated at 1600 °C for 10 h. **Figure 7.5** shows the phases (ZrO_2 and $TaZr_{2.75}O_8$) formed during oxidation on the surface of oxidized samples.

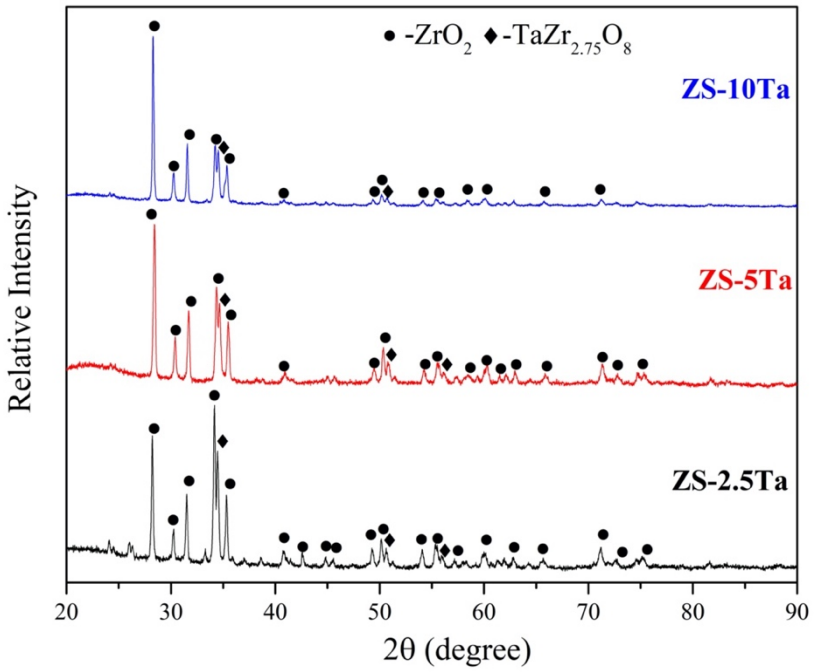

Figure 7.5 XRD phase analysis of ZrB_2-20SiC-(2.5-10)Ta composites after oxidation at 1600 °C for 10 h.

Table 7.1 shows the variation of specific weight gain and oxide layer thickness as a function of tantalum amount in ZrB_2-20SiC composite. The specific weight gain and oxide layer thickness was lowered with increasing Ta amount. The oxide layer thickness of the samples was calculated by using cross-sectional images of oxidized samples. The specific weight gain reduced from 21.04 to 16.65 mg/cm^2 with increasing amount of tantalum. Similarly, the oxide layer thickness was reduced from 320 to 255 μm with increasing amount of tantalum and this data is compared with the literature in **Table 7.1**. **Figure 7.6** shows the surface (a, b and c) morphology of oxidized samples. It shows the dark SiO_2 phase and ZrO_2 grains surrounded by $TaZr_{2.75}O_8$ phase. As the amount of tantalum increases the $TaZr_{2.75}O_8$ phase increases, which improves the viscosity of liquid silica layer and improve the oxidation resistance. **Figure 7.6**

(d, e and f) shows representative EDS analysis of phases observed in the surface microstructure of oxidized sample for ZS-5Ta sample. The oxidized composites contain of three distinct layers such as top dense passive SiO_2 layer, intermediate SiC-depleted layer and unreacted bulk composite (**Figure 7.7**). In the SiC-depleted layer, from the EDS elemental analysis it is observed that the Si element is absent in the layer.

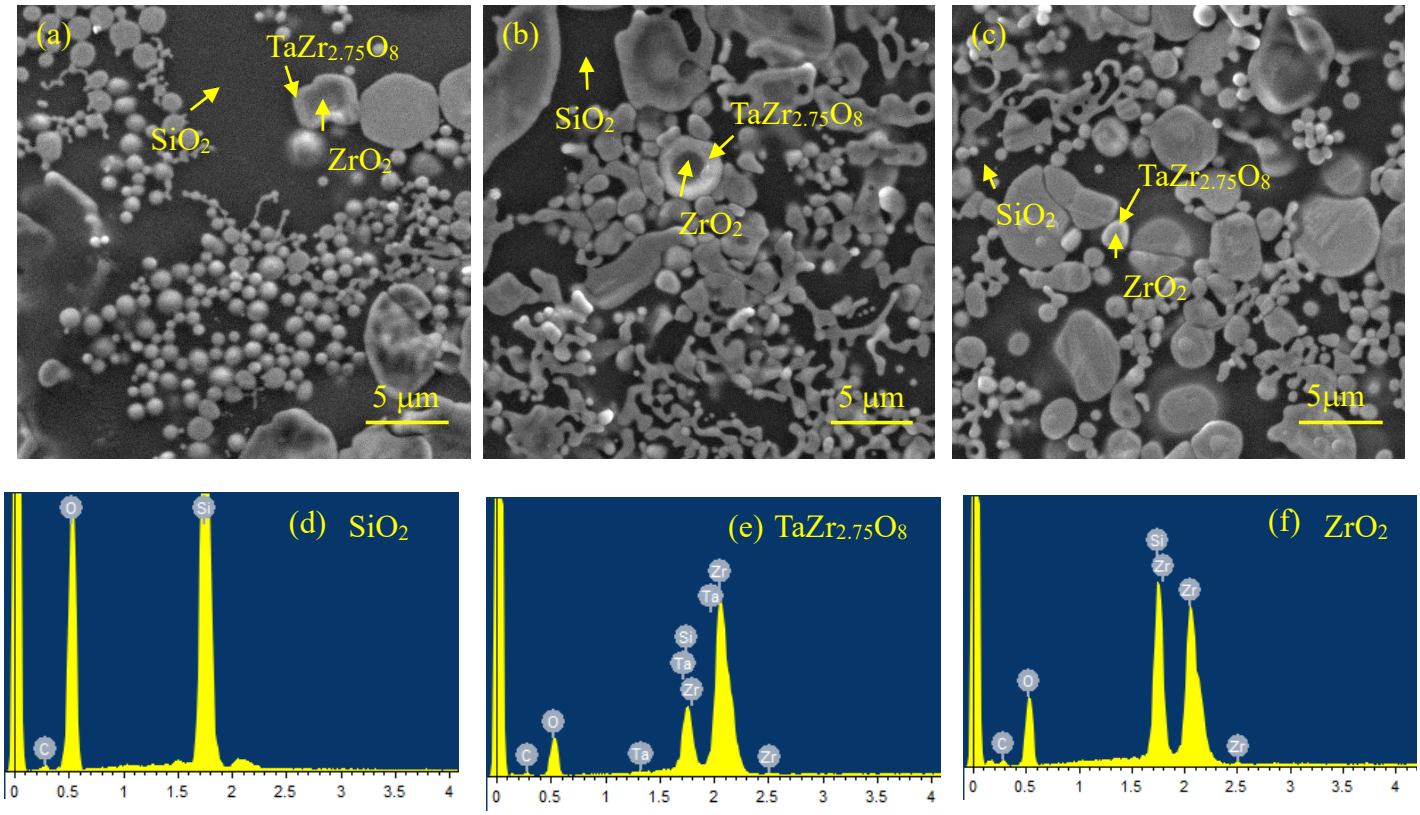

Figure 7.6 Morphology of oxidation tested (a) ZS-2.5Ta, (b) ZS-5Ta and (c) ZS-10Ta samples; corresponding EDS elemental maps of phases (d) SiO_2, (e) $TaZr_{2.75}O_8$ and (f) ZrO_2 for ZS-5Ta composition after oxidation at 1600 °C for 10 h.

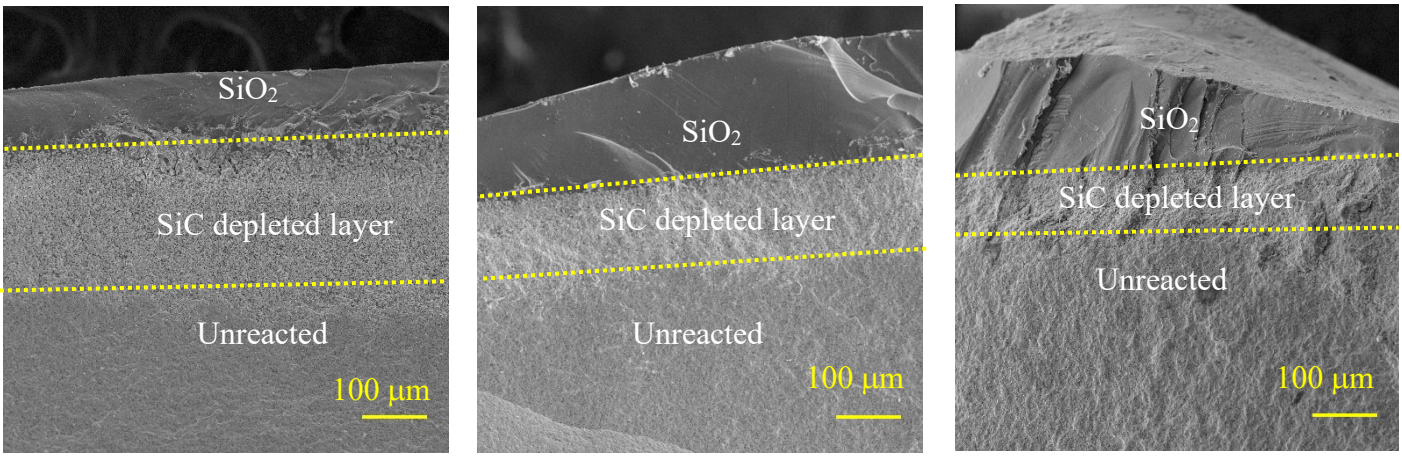

Figure 7.7 Cross-sectional SEM images of (a) ZS-2.5Ta, (b) ZS-5Ta and (c) ZS-10Ta samples and (d), (e) and (f) shows representative EDS elemental mapping of SiO_2, SiC-depleted layer and unreacted bulk sample after oxidation at 1600 °C for 10 h.

The thickness of oxide layer reduced with increasing amount of tantalum. It is also observed that as the amount of tantalum increases the thickness of SiC-depleted layer reduces, which is due to protective behaviour of top passive SiO_2 layer. Hence, the addition of tantalum will be helpful to improve the oxidation resistance of ZrB_2-based composites.

7.3 Summary

The ZrB_2-SiC-Ta composites composed of crystalline ZrO_2, $TaZr_{2.75}O_8$ and amorphous SiO_2 phases after isothermal oxidation at 1500 and 1600 °C for 10 h. The cross-sectional SEM-EDS of oxidized samples revealed three-layered architecture: the top passive SiO_2 layer, intermediate SiC depleted layer and bottom unreacted bulk.

Chapter 8

Conclusions and future scope of the work

8.1 Conclusions

This chapter brings out the conclusions that emerge out of this dissertation.

- The ZrB_2-20vol.% SiC-(2.5-10)Si_3N_4 composites could be densified to more than 98% theoretical density after multi stage SPS at 1900 °C for 3 min under 50 MPa.
- It has to be noted that even with the use of SPS and Si_3N_4 a higher sintering temperature of 1900 °C was required to densify ZrB_2-20SiC composites. However, the ZrB_2-20vol.% SiC-(0-10)vol.% Si_3N_4 composites were characterized with uniform microstructure and the grain size of ZrB_2 varied narrowly between 3.37 and 3.61 μm and it slightly increased with increasing addition of Si_3N_4.
- The microstructural analysis of the ZrB_2-20vol.% SiC- Si_3N_4 composites composed of secondary phases (ZrO_2, BN, ZrN) along with ZrB_2 and SiC major phases. The formation of such new phases indicate involvement of sintering reactions during SPS. All the secondary phases were well dispersed in ZrB_2 matrix.
- The ZrB_2-20vol.% SiC-5vol.% Si_3N_4 composite measured with the maximum hardness of 30.56 GPa.
- The weight gain of ZrB_2-20vol.% SiC composites decreased (from 13.84 to 9.84 mg/cm^2) and oxide layer thickness increased (64–128 μm) with increasing amount of Si_3N_4 from 2.5 to 10vol.%. It is obvious that the oxidation resistance of ZrB_2-20 vol% SiC composites increased with the addition of Si_3N_4.
- The microstructure of oxidized samples surfaces after oxidation (at 1500 and 1600 °C for 10 h) consists of ZrO_2 and SiO_2 phases in all samples. The cross-sectional microstructure of oxidized ZrB_2-20SiC-(2.5-10)Si_3N_4 composites consists of thick dense outer layer of SiO_2, intermediate (ZrO_2-SiO_2) layer and unreacted bulk.

- More than 99% theoretical density was achieved for ZrB_2-20vol.% SiC-(0-10)wt.% Ta composites after MS SPS at 1900 °C, 50 MPa for 3 min.
- The microstructure of sintered samples consists of ZrB_2 core, (Zr, Ta)B_2 rim, SiC as major crystalline phases and minor amounts of ZrO_2 and (Zr, Ta)C phases.
- The ZrB_2-SiC-Ta composites composed of crystalline ZrO_2, $TaZr_{2.75}O_8$ and amorphous SiO_2 phases after isothermal oxidation at 1500 and 1600 °C for 10 h.
- The cross-sectional SEM-EDS of oxidized samples revealed three-layered architecture: the top passive SiO_2 layer, intermediate SiC-depleted layer and bottom unreacted bulk.
- The decrease in weight and oxide layer thickness of ZrB_2-20vol% SiC with increasing amounts of tantalum confirm its improved oxidation resistance.
- However, ZrB_2-20SiC-(2.5-10)Si_3N_4 exhibited much better oxidation resistance than Ta reinforced ZrB_2-20SiC ceramics as the ZrB_2-20SiC-(2.5-10)Si_3N_4 composites characterised with no SiC depleted layer and exhibited relatively better oxidation resistance than ZrB_2-SiC-Ta composites.

8.2 Future scope of the work

The list below considered as the future research work to further understanding of ZrB_2-20SiC-(2.5-10)Si_3N_4/Ta composites for high-temperature applications.

- Detailed microstructural characterization using TEM and EBSD will give better understanding of these materials at fine scale level.
- High temperature (above 2000 °C) oxidation/ablation studies of these composites gives the idea about its performance.
- Measurements of high temperature mechanical and wear properties of ZrB_2-20SiC-(2.5-10)Si_3N_4/Ta composites provide knowledge of failure/damage analysis.
- High temperature thermal and electrical conductivity measurements along with optical properties will enable to assess potential of these materials for energy absorption applications.

References

[1] A. Wang, H. Liao, T. Zhang, M. Jiang, F. Guo, and Y. Wang, "Study on the effect of sample shapes on the thermal shock behavior of ZrB_2-SiC-Graphite sharp leading edge," *Int. J. Ceram. Eng. Sci.*, vol. 2, no. 2, pp. 101–109, 2020.

[2] N. P. Padture, "Advanced structural ceramics in aerospace propulsion," *Nat. Mater.*, vol. 15, no. 8, pp. 804–809, 2016.

[3] T. H. Squire and J. Marschall, "Material property requirements for analysis and design of UHTC components in hypersonic applications," *J. Eur. Ceram. Soc.*, vol. 30, no. 11, pp. 2239–2251, 2010.

[4] R. Savino, S. Mungiguerra, and G. D. Di Martino, "Testing ultra-high-temperature ceramics for thermal protection and rocket applications," *Adv. Appl. Ceram.*, vol. 117, no. sup1, pp. s9–s18, 2018.

[5] J. Reuther, D. Kinney, S. Smith, and D. A. Kontinos, "A Reusable space vehicle design study exploring sharp leading edges," in *35th AIAA Thermophysics Conference*, 2001.

[6] A. Purwar and B. Basu, "Thermo-structural design of ZrB_2–SiC-based thermal protection system for hypersonic space vehicles," *J. Am. Ceram. Soc.*, vol. 100, no. 4, pp. 1618–1633, 2017.

[7] R. Borrelli, A. Riccio, D. Tescione, R. Gardi, and G. Marino, "Thermo-structural behaviour of an UHTC made nose cap of a reentry vehicle," *Acta Astronaut.*, vol. 65, no. 3–4, pp. 442–456, 2009.

[8] T. Cheng, W. Li, and D. Fang, "Thermal shock resistance of ultra-high-temperature ceramics under aerodynamic thermal environments," *AIAA J.*, vol. 51, no. 4, pp. 840–848, 2013.

[9] W. G. Fahrenholtz and G. E. Hilmas, "Ultra-high temperature ceramics: Materials for extreme environments," *Scr. Mater.*, vol. 129, pp. 94–99, 2017.

[10] S. P. Walker and B. J. Sullivan, "Sharp Refractory Composite Leading Edges on Hypersonic Vehicles," *Am. Inst. Aeronaut. Astronaut.*, no. December, pp. 1–9, 2003.

[11] C. Blanco, E. Casal, M. Granda, and R. Menéndez, "Influence of fibre-matrix interface on the fracture behaviour of carbon-carbon composites," *J. Eur. Ceram. Soc.*, vol. 23, no. 15, pp. 2857–2866, 2003.

[12] R. Luo, T. Liu, J. Li, H. Zhang, Z. Chen, and G. Tian, "Thermophysical properties of carbon/carbon composites and physical mechanism of thermal expansion and thermal conductivity," *Carbon N. Y.*, vol. 42, no. 14, pp. 2887–2895, 2004.

[13] K. Upadhya, J.-M. Yang, and W. P. Hoffman, “Advanced Materials for Ultrahigh Temperature Structural Applications above 2000°C,” *Am. Ceram. Soc. Bull.*, vol. 76, pp. 51–56, 1997.

[14] M. M. Opeka, I. G. Talmy, and J. Zaykoski, “Oxidation-based materials selection for 2000°C+ hypersonic aerosurfaces : Theoretical considerations and historical experience,” *J. Mater. Sci.*, vol. 39. pp. 5887–5904, 2004.

[15] L. Pienti, L. Silvestroni, E. Landi, C. Melandri, and D. Sciti, “Microstructure, mechanical properties and oxidation behavior of TaC- and HfC-based materials containing short SiC fiber,” *Ceram. Int.*, vol. 41, no. 1, pp. 1367–1377, 2015.

[16] C. W. Ohlhorst, D.E. Glass, W. E. Bruce, M. C. Lindell, W. L. Vaughn, R. W. Smith, R. B. Dirling, P. A. Hogenson, D. R. Thompson, W. Kowbel, B. J. Sullivan, J. R. Koenig, “Development of X-43A mach 10 leading edges,” *Int. Astronaut. Fed. - 56th Int. Astronaut. Congr. 2005*, vol. 8, pp. 5290–5298, 2005.

[17] Y. Morisada, Y. Miyamoto, Y. Takaura, K. Hirota, and N. Tamari, “Mechanical properties of SiC composites incorporating SiC-coated multi-walled carbon nanotubes,” *Int. J. Refract. Met. Hard Mater.*, vol. 25, no. 4, pp. 322–327, 2007.

[18] W.-M. Guo, L.-X. Wu, T. Ma, S.-X. Gu, Y. You, H.-T. Lin, S.-H. Wu, G.-J. Zhang, “Chemical reactivity of hot-pressed Si_3N_4–ZrB_2 ceramics at 1500–1700°C,” *J. Eur. Ceram. Soc.*, vol. 35, no. 11, pp. 2973–2979, 2015.

[19] Y. Kim, M. Mimoto, and T. Nishimura, “High-Temperature Strength of Liquid-Phase-Sintered SiC with AlN and Re_2O_3 (RE= Y, Yb),” *J. Am. Ceram. Soc.*, vol. 85, no. 4. pp. 1007–1009, 2002.

[20] M. Khodaei, O. Yaghobizadeh, H. R. Baharvandi, and A. Dashti, “Effects of different sintering methods on the properties of SiC-TiC, SiC-TiB_2 composites,” *Int. J. Refract. Met. Hard Mater.*, vol. 70, no. August 2017, pp. 19–31, 2018.

[21] C. Carney, M. Cinibulk, and T. Parthasarathy, “Processing and Evaluation of UHTC Loaded Composites,” in *Ultra-High Temperature Ceramics: Materials for Extreme Environment Applications IV*, 2017.

[22] B. Basu, “Toughening of yttria-stabilised tetragonal zirconia ceramics,” *Int. Mater. Rev.*, vol. 50, no. 4, pp. 239–256, 2005.

[23] C. Tian, D. Gao, Y. Zhang, C. Xu, Y. Song, and X. Shi, “Oxidation behaviour of zirconium diboride-silicon carbide ceramic composites under low oxygen partial pressure,” *Corros. Sci.*, vol. 53, no. 11, pp. 3742–3746, 2011.

[24] A. Mukhopadhyay, G. B. Raju, and B. Basu, “Ultra High Temperature Ceramics: Processing, Properties, and Applications,” in *MAX Phases and Ultra-High Temperature*

Ceramics for Extreme Environments, I. M. Low, Y. Sakka, and C. F. Hu, Eds. IGI Global, USA, 2013, pp. 100–124.

[25] W. G. Fahrenholtz, G. E. Hilmas, I. G. Talmy, and J. A. Zaykoski, "Refractory diborides of zirconium and hafnium," *J. Am. Ceram. Soc.*, vol. 90, no. 5, pp. 1347–1364, 2007.

[26] B. Basu, G. B. Raju, and A. K. Suri, "Processing and properties of monolithic TiB_2 based materials," *Int. Mater. Rev.*, vol. 51, no. 6, pp. 352–374, 2006.

[27] A. Bellosi and F. Monteverde, "Ultra High Temperature Ceramics: Microstructure Control and Properties Improvement Related to Materials Design and Processing Procedures," in *5th European Workshop on Thermal Protection Systems and Hot Structures*, 2006, pp. 1–8.

[28] S. M. Johnson, "Ultra High Temperature Ceramics Application: Issues and Prospects," *2nd Ceram. Leadersh. Summit*, pp. 4–8, 2011.

[29] E. Wuchina, E. Opila, M. Opeka, W. Fahrenholtz, and I. Talmy, "UHTCs: Ultra-High Temperature Ceramic Materials for Extreme Environment Applications," *Electrochem. Soc. Interface*, pp. 30–36, 2007.

[30] J. Binner *et al.*, "Selection, processing, properties and applications of ultra-high temperature ceramic matrix composites, UHTCMCs – a review," *Int. Mater. Rev.*, vol. 0, no. 0, pp. 1–56, Sep. 2019.

[31] G. Brahma Raju, T. Bhandari, A. Mukhopadhyay, and B. Basu, "Titanium Diboride," in *Ultra-High Temperature Ceramics: Materials for ExtremeEnvironment Applications*, W. G. Fahrenholtz, E. J. Wuchina, W. E. Lee, and Y. Zhou, Eds. New Jersey: John Wiley & Sons, 2014, pp. 316–360.

[32] C. Musa, R. Orrù, D. Sciti, L. Silvestroni, and G. Cao, "Synthesis, consolidation and characterization of monolithic and SiC whiskers reinforced HfB_2 ceramics," *J. Eur. Ceram. Soc.*, vol. 33, no. 3, pp. 603–614, 2013.

[33] G. B. Raju and B. Basu, "Development of High Temperature TiB_2-Based Ceramics," *Key Eng. Mater.*, vol. 395, pp. 89–124, 2009.

[34] W. W. Wu, M. Estili, T. Nishimura, G. J. Zhang, and Y. Sakka, "Machinable ZrB_2-SiC-BN composites fabricated by reactive spark plasma sintering," *Mater. Sci. Eng. A*, vol. 582, pp. 41–46, 2013.

[35] E. Sani, E. Landi, D. Sciti, and V. Medri, "Optical properties of ZrB_2 porous architectures," *Sol. Energy Mater. Sol. Cells*, vol. 144, pp. 608–615, 2016.

[36] J. F. Justin and A. Jankowiak, "Ultra High Temperature Ceramics: Densification, Properties and Thermal Stability," *AerospaceLab J.*, vol. 3, no. 3, pp. 3–8, 2011.

[37] L. Silvestroni and D. Sciti, "Densification of ZrB_2-$TaSi_2$ and HfB_2-$TaSi_2$ Ultra-High-

Temperature Ceramic Composites," *J. Am. Ceram. Soc.*, vol. 94, no. 6, pp. 1920–1930, 2011.

[38] J. K. Sonber and A. K. Suri, "Synthesis and consolidation of zirconium diboride: review," *Adv. Appl. Ceram.*, vol. 110, no. 6, pp. 321–334, 2011.

[39] S. Q. Guo, "Densification of ZrB_2-based composites and their mechanical and physical properties: A review," *J. Eur. Ceram. Soc.*, vol. 29, no. 6, pp. 995–1011, 2009.

[40] Y. Feng, Y. Guo, Z. Ling, and X. Zhang, "Investigation on machining performance of micro-holes EDM in ZrB_2-SiC ceramics using a magnetic suspension spindle system," *Int. J. Adv. Manuf. Technol.*, pp. 1–13, 2018.

[41] T. N. Maity, N. K. Gopinath, K. Biswas, and B. Basu, "Spark Plasma Sintering of Ultrahigh Temperature Ceramics," in *Spark Plasma Sintering of Materials*, P. Cavaliere, Ed. Switzerland: Springer, 2019, pp. 369–440.

[42] X. Zhang, X. Luo, J. Li, J. Han, W. Han, and C. Hong, "Structure and bonding features of ZrB_2(0 0 0 1) surface," *Comput. Mater. Sci.*, vol. 46, no. 1, pp. 1–6, 2009.

[43] B. Yang, J. Li, B. Zhao, Y. Hu, T. Wang, D. Sun, R. Li, S. Yin, Z. Feng, Q. Tang, T. Sato, "Synthesis of hexagonal-prism-like ZrB_2 by a sol-gel route," *Powder Technol.*, vol. 256, pp. 522–528, 2014.

[44] J. F. Guria, A. Bansal, and V. Kumar, "Effect of additives on the thermal conductivity of zirconium diboride based composites – A review," *J. Eur. Ceram. Soc.*, vol. 41, no. 1, pp. 1–23, 2021.

[45] S. Zhu, "Densification, microstructure, and mechanical properties of zirconium diboride based ultra-high temperature ceramics," Missouri University of Science and Technology, 2008.

[46] M. Miller-Oana, "Oxidation behavior of Carbon and ultra-high temperature ceramics," University of Arizona, 2016.

[47] R. Li, Y. Zhang, H. Lou, J. Li, and Z. Feng, "Synthesis of ZrB_2 nanoparticles by sol-gel method," *J. Sol-Gel Sci. Technol.*, vol. 58, no. 2, pp. 580–585, 2011.

[48] Y. Zhang, R. Li, Y. Jiang, B. Zhao, H. Duan, J. Li, Z. Feng, "Morphology evolution of ZrB_2 nanoparticles synthesized by solgel method," *J. Solid State Chem.*, vol. 184, no. 8, pp. 2047–2052, 2011.

[49] R. V. Krishnarao, "Preparation of ZrB_2 and ZrB_2-SiC powders in a single step reduction of zircon ($ZrSiO_4$) with B_4C," *Ceram. Int.*, vol. 43, no. 1, pp. 1205–1209, 2017.

[50] S. K. Mishra, S. Das, and L. C. Pathak, "Defect structures in zirconium diboride powder prepared by self-propagating high-tempeture synthesis," *Mater. Sci. Eng. A*, vol. 364, no. 1–2, pp. 249–255, 2004.

[51] J. Zou, H. Bin Ma, A. D'Angio, and G. J. Zhang, "Tungsten carbide: A versatile additive to get trace alkaline-earth oxide impurities out of ZrB_2 based ceramics," *Scr. Mater.*, vol. 147, pp. 40–44, 2018.

[52] F. Monteverde and A. Bellosi, "Effect of the addition of silicon nitride on sintering behaviour and microstructure of zirconium diboride," *Scr. Mater.*, vol. 46, no. 3, pp. 223–228, 2002.

[53] R. Telle, "Boride and carbide ceramics," in *Structure and properties of ceramics*, S. M., Ed. Germany: Wiley, 1996, pp. 175–258.

[54] L. Rangaraj, C. Divakar, and V. Jayaram, "Processing of Refractory Metal Borides, Carbides and Nitrides," *Key Eng. Mater.*, vol. 395, pp. 69–88, 2009.

[55] S. K. Mishra and L. C. Pathak, "Self-Propagating High-Temperature Synthesis (SHS) of Advanced High-Temperature Ceramics," *Key Eng. Mater.*, vol. 395, pp. 15–38, 2009.

[56] E. D. Case, J. R. Smyth, and O. Hunter, "Grain-size dependence of microcrack initiation in brittle materials," *J. Mater. Sci.*, vol. 15, no. 1, pp. 149–153, 1980.

[57] W. Wang, Z. Fu, H. Wang, and R. Yuan, "Influence of hot pressing sintering temperature and time on microstructure and mechanical properties of TiB_2 ceramics," *J. Eur. Ceram. Soc.*, vol. 22, no. 7, pp. 1045–1049, 2002.

[58] V. Zamora, A. L. Ortiz, F. Guiberteau, and M. Nygren, "Spark-plasma sintering of ZrB_2 ultra-high-temperature ceramics at lower temperature via nanoscale crystal refinement," *J. Eur. Ceram. Soc.*, vol. 32, no. 10, pp. 2529–2536, 2012.

[59] J. Zou, S. K. Sun, G. J. Zhang, Y. M. Kan, P. L. Wang, and T. Ohji, "Chemical reactions, anisotropic grain growth and sintering mechanisms of self-reinforced ZrB_2-SiC doped with WC," *J. Am. Ceram. Soc.*, vol. 94, no. 5, pp. 1575–1583, 2011.

[60] X. G. Wang, W. M. Guo, and G. J. Zhang, "Pressureless sintering mechanism and microstructure of ZrB_2-SiC ceramics doped with boron," *Scr. Mater.*, vol. 61, no. 2, pp. 177–180, 2009.

[61] C. A. Galán, A. L. Ortiz, F. Guiberteau, and L. L. Shaw, "Crystallite size refinement of ZrB_2 by high-energy ball milling," *J. Am. Ceram. Soc.*, vol. 92, no. 12, pp. 3114–3117, 2009.

[62] A. L. Chamberlain, W. G. Fahrenholtz, and G. E. Hilmas, "Reactive hot pressing of zirconium diboride," *J. Eur. Ceram. Soc.*, vol. 29, no. 16, pp. 3401–3408, 2009.

[63] M. S. Asl, B. Nayebi, Z. Ahmadi, M. J. Zamharir, and M. Shokouhimehr, "Effects of carbon additives on the properties of ZrB_2–based composites: A review," *Ceram. Int.*, vol. 44, no. 7, pp. 7334–7348, 2018.

[64] J. K. Sonber, T. S. R. C. Murthy, K. Sairam, A. Nagaraj, S. Majumdar, and V. Kain,

"ZrB_2 based novel composite with NiAl as reinforcement phase," *Int. J. Refract. Met. Hard Mater.*, vol. 70, no. September 2017, pp. 56–65, 2018.

[65] A. K. Khanra, B. R. Sarkar, B. Bhattacharya, L. C. Pathak, and M. M. Godkhindi, "Performance of ZrB_2-Cu composite as an EDM electrode," *J. Mater. Process. Technol.*, vol. 183, no. 1, pp. 122–126, 2007.

[66] S. C. Zhang, G. E. Hilmas, and W. G. Fahrenholtz, "Pressureless sintering of ZrB_2-SiC ceramics," *J. Am. Ceram. Soc.*, vol. 91, no. 1, pp. 26–32, 2008.

[67] V. H. Nguyen *et al.*, "TEM characterization of hot-pressed ZrB_2-SiC-AlN composites," *Results Phys.*, vol. 19, no. May, 2020.

[68] M. Shahedi Asl, B. Nayebi, Z. Ahmadi, P. Pirmohammadi, and M. Ghassemi Kakroudi, "Fractographical characterization of hot pressed and pressureless sintered SiAlON-doped ZrB_2-SiC composites," *Mater. Charact.*, vol. 102, pp. 137–145, 2015.

[69] L. Silvestroni, S. Failla, V. Vinokurov, I. Neshpor, and O. Grigoriev, "Core-shell structure: An effective feature for strengthening ZrB_2 ceramics," *Scr. Mater.*, vol. 160, pp. 1–4, Feb. 2019.

[70] T. Zhu, L. Xu, X. Zhang, W. Han, P. Hu, and L. Weng, "Densification, microstructure and mechanical properties of ZrB_2-SiC_w ceramic composites," *J. Eur. Ceram. Soc.*, vol. 29, no. 13, pp. 2893–2901, 2009.

[71] W. G. Fahrenholtz, G. E. Hilmas, and R. Li, "Densification of Ultra-Refractory Transition Metal Diboride Ceramics," *Sci. Sinter.*, vol. 52, no. 1, pp. 1–14, 2020.

[72] V. H. Nguyen, S. A. Delbari, M. S. Asl, A. S. Namini, M. G. Kakroudi, Y. Azizin-Kalandaragh, Q. V. Le, M. Mohammadi, M. Shokouhimehr, "Role of hot-pressing temperature on densification and microstructure of ZrB_2–SiC ultrahigh temperature ceramics," *Int. J. Refract. Met. Hard Mater.*, vol. 93, no. August, 2020.

[73] M. Khoeini, A. Nemati, M. Zakeri, M. Tamizifar, and H. Samadi, "Comprehensive study on the effect of SiC and carbon additives on the pressureless sintering and microstructural and mechanical characteristics of new ultra-high temperature ZrB_2 ceramics," *Ceram. Int.*, vol. 41, no. 9, pp. 11456–11463, 2015.

[74] M. Khoeini, A. Nemati, M. Zakeri, and M. Shahedi Asl, "Pressureless sintering of ZrB_2 ceramics codoped with TiC and graphite," *Int. J. Refract. Met. Hard Mater.*, vol. 81, no. February, pp. 189–195, 2019.

[75] H.-B. Ma, H.-L. Liu, J. Zhao, F.-F. Xu, and G.-J. Zhang, "Pressureless sintering, mechanical properties and oxidation behavior of ZrB_2 ceramics doped with B_4C," *J. Eur. Ceram. Soc.*, vol. 35, no. 10, pp. 2699–2705, 2015.

[76] A. L. Chamberlain, W. G. Fahrenholtz, and G. E. Hilmas, "Pressureless sintering of

zirconium diboride," *J. Am. Ceram. Soc.*, vol. 89, no. 2, pp. 450–456, 2006.

[77] M. Mashhadi, M. Shambuli, and S. Safi, "Effect of $MoSi_2$ addition and particle size of SiC on pressureless sintering behavior and mechanical properties of ZrB_2-SiC-$MoSi_2$ composites," *J. Mater. Res. Technol.*, vol. 5, no. 3, pp. 200–205, 2016.

[78] Z. Ahmadi, B. Nayebi, M. Shahedi Asl, M. G. Kakroudi, and I. Farahbakhsh, "Sintering behavior of ZrB_2–SiC composites doped with Si_3N_4: A fractographical approach," *Ceram. Int.*, vol. 43, no. 13, pp. 9699–9708, 2017.

[79] S. Q. Guo, J. M. Yang, H. Tanaka, and Y. Kagawa, "Effect of thermal exposure on strength of ZrB_2-based composites with nano-sized SiC particles," *Compos. Sci. Technol.*, vol. 68, no. 14, pp. 3033–3040, 2008.

[80] E. W. Neuman, G. E. Hilmas, and W. G. Fahrenholtz, "Processing, microstructure, and mechanical properties of large-grained zirconium diboride ceramics," *Mater. Sci. Eng. A*, vol. 670, pp. 196–204, 2016.

[81] C. Xia, S. A. Delbari, Z. Ahmadi, M. S. Asl, M. G. Kakroudi, Q. V. Le, A. S. Namini, M. Mohammadi, M. Shokouhimehr, "Electron microscopy study of ZrB_2–SiC–AlN composites: Hot-pressing vs. pressureless sintering," *Ceram. Int.*, vol. 46, no. August, pp. 29334–29338, 2020.

[82] W. M. Guo, Z. G. Yang, and G. J. Zhang, "Comparison of ZrB_2-SiC ceramics with Yb_2O_3 additive prepared by hot pressing and spark plasma sintering," *Int. J. Refract. Met. Hard Mater.*, vol. 29, no. 4, pp. 452–455, 2011.

[83] J. K. Sonber, T. S. R. C. Murthy, K. Sairam, and J. K. Chakravartty, "Effect of NdB_6 addition on densification and properties of ZrB_2," *Ceram. - Silikaty*, vol. 60, no. 2, pp. 41–47, 2016.

[84] F. Monteverde, S. Guicciardi, and A. Bellosi, "Advances in microstructure and mechanical properties of zirconium diboride based ceramics," *Mater. Sci. Eng. A*, vol. 346, no. 1–2, pp. 310–319, 2003.

[85] E. W. Neuman, G. E. Hilmas, and W. G. Fahrenholtz, "Processing, microstructure, and mechanical properties of zirconium diboride-boron carbide ceramics," *Ceram. Int.*, vol. 43, no. 9, pp. 6942–6948, 2017.

[86] M. Patel, J. J. Reddy, V. V. Bhanu Prasad, J. Subrahmanyam, and V. Jayaram, "Residual strength of hot pressed zirconium diboride (ZrB_2) after exposure to high temperatures," *Mater. Sci. Eng. A*, vol. 535, pp. 189–196, 2012.

[87] A. L. Chamberlain, W. G. Fahrenholtz, G. E. Hilmas, and D. T. Ellerby, "High-strength zirconium diboride-based ceramics," *J. Am. Ceram. Soc.*, vol. 87, no. 6, pp. 1170–1172, 2004.

[88] B. R. Golla and B. Basu, “Spark Plasma Sintering of Nanoceramic Composites,” in *Comprehensive Hard Materials*, vol. 2, Elsevier Ltd, 2014, pp. 177–205.

[89] A. Mukhopadhyay and B. Basu, “Consolidation–microstructure–property relationships in bulk nanoceramics and ceramic nanocomposites: a review,” *Int. Mater. Rev.*, vol. 52, no. 5, pp. 257–288, 2007.

[90] R. Raj, M. Cologna, and J. S. C. Francis, “Influence of externally imposed and internally generated electrical fields on grain growth, diffusional creep, sintering and related phenomena in ceramics,” *J. Am. Ceram. Soc.*, vol. 94, no. 7, pp. 1941–1965, 2011.

[91] Z. A. Munir, D. V. Quach, and M. Ohyanagi, “Electric current activation of sintering: A review of the pulsed electric current sintering process,” *J. Am. Ceram. Soc.*, vol. 94, no. 1, pp. 1–19, 2011.

[92] T. Nishimura, X. Xu, K. Kimoto, N. Hirosaki, and H. Tanaka, “Fabrication of silicon nitride nanoceramics — Powder preparation and sintering: A review,” *Sci. Technol. Adv. Mater.*, vol. 8, pp. 635–643, 2007.

[93] R. Orrù, R. Licheri, A. M. Locci, A. Cincotti, and G. Cao, “Consolidation/synthesis of materials by electric current activated/assisted sintering,” *Mater. Sci. Eng. R Reports*, vol. 63, no. 4–6, pp. 127–287, 2009.

[94] D. Demirskyi, H. Borodianska, Y. Sakka, and O. Vasylkiv, “Ultra-high elevated temperature strength of TiB_2-based ceramics consolidated by spark plasma sintering,” *J. Eur. Ceram. Soc.*, vol. 37, no. 1, pp. 393–397, 2017.

[95] R. Eatemadi and Z. Balak, “Investigating the effect of SPS parameters on densification and fracture toughness of ZrB_2-SiC nanocomposite,” *Ceram. Int.*, vol. 45, no. 4, pp. 4763–4770, 2018.

[96] J. Lyu, E. B. Kashkarov, N. Travitzky, M. S. Syrtanov, and A. M. Lider, “Sintering of MAX-phase materials by spark plasma and other methods,” *J. Mater. Sci.*, 2020.

[97] R. Marder, C. Estournès, G. Chevallier, and R. Chaim, “Plasma in spark plasma sintering of ceramic particle compacts,” *Scr. Mater.*, vol. 82, pp. 57–60, 2014.

[98] D. M. Hulbert, A. Anders, J. Andersson, E. J. Lavernia, and A. K. Mukherjee, “A discussion on the absence of plasma in spark plasma sintering,” *Scr. Mater.*, vol. 60, no. 10, pp. 835–838, 2009.

[99] D. Jain, K. M. Reddy, A. Mukhopadhyay, and B. Basu, “Achieving uniform microstructure and superior mechanical properties in ultrafine grained TiB_2-$TiSi_2$ composites using innovative multi stage spark plasma sintering,” *Mater. Sci. Eng. A*, vol. 528, no. 1, pp. 200–207, 2010.

[100] K. Madhav Reddy, N. Kumar, and B. Basu, “Inhibition of grain growth during the final

stage of multi-stage spark plasma sintering of oxide ceramics," *Scr. Mater.*, vol. 63, no. 6, pp. 585–588, 2010.

[101] K. Madhav Reddy, N. Kumar, and B. Basu, "Innovative multi-stage spark plasma sintering to obtain strong and tough ultrafine-grained ceramics," *Scr. Mater.*, vol. 62, no. 7, pp. 435–438, 2010.

[102] N. Gupta, A. Mukhopadhyay, K. Pavani, and B. Basu, "Spark plasma sintering of novel ZrB_2-SiC-$TiSi_2$ composites with better mechanical properties," *Mater. Sci. Eng. A*, vol. 534, pp. 111–118, 2012.

[103] K. M. Reddy, A. Mukhopadhyay, and B. Basu, "Microstructure-mechanical-tribological property correlation of multistage spark plasma sintered tetragonal ZrO_2," *J. Eur. Ceram. Soc.*, vol. 30, no. 16, pp. 3363–3375, 2010.

[104] N. Gupta, V. Parameswaran, and B. Basu, "Microstructure development, nanomechanical, and dynamic compression properties of spark plasma sintered TiB_2-Ti-based homogeneous and Bi-layered composites," *Metall. Mater. Trans. A Phys. Metall. Mater. Sci.*, vol. 45, no. 10, pp. 4646–4664, 2014.

[105] R. I. Todd, E. Zapata-Solvas, R. S. Bonilla, T. Sneddon, and P. R. Wilshaw, "Electrical characteristics of flash sintering: Thermal runaway of Joule heating," *J. Eur. Ceram. Soc.*, vol. 35, no. 6, pp. 1865–1877, 2015.

[106] B. Niu, F. Zhang, J. Zhang, W. Ji, W. Wang, and Z. Fu, "Ultra-fast densification of boron carbide by flash spark plasma sintering," *Scr. Mater.*, vol. 116, pp. 127–130, 2016.

[107] J. Gonzalez-Julian, K. Jahnert, K. Speer, L. Liu, J. Rathel, M. Knapp, H. Ehrenberg, M. Bram, O. Guillon, "Effect of Internal Current Flow during the Sintering of Zirconium Diboride by Field Assisted Sintering Technology," *J. Am. Ceram. Soc.*, vol. 99, no. 1, pp. 35–42, 2016.

[108] S. Grasso, E.-Y. Kim, T. Saunders, M. Yu, S.-H. Choi, A. Tudball, M. Reece, "Ultra-Rapid Crystal Growth of Textured SiC Using Flash Spark Plasma Sintering Route," *Cryst. Growth Des.*, vol. 16, no. 4, pp. 2317–2321, 2016.

[109] M. Cologna, B. Rashkova, and R. Raj, "Flash sintering of nanograin zirconia in <5 s at 850°C," *J. Am. Ceram. Soc.*, vol. 93, no. 11, pp. 3556–3559, 2010.

[110] S. Grasso, T. Saunders, H. Porwal, O. Cedillos-Barraza, D. D. Jayaseelan, W. E. Lee, M. J. Reece, "Flash spark plasma sintering (FSPS) of pure ZrB_2," *J. Am. Ceram. Soc.*, vol. 97, no. 8, pp. 2405–2408, 2014.

[111] J. Wu, B.Niu, F. Zhang, L. Lei, J. Zhang, L. Ren, W. Wang, Z. Fu , "Effect of titanium diboride on the homogeneity of boron carbide ceramic by flash spark plasma sintering," *Ceram. Int.*, vol. 44, no. 13, pp. 15323–15330, 2018.

[112] E. Zapata-Solvas, D. Gómez-García, A. Domínguez-Rodríguez, and R. I. Todd, "Ultra-fast and energy-efficient sintering of ceramics by electric current concentration," *Sci. Rep.*, vol. 5, p. 8513, 2015.

[113] G. J. K. Harrington, G. E. Hilmas, and W. G. Fahrenholtz, "Effect of carbon on the thermal and electrical transport properties of zirconium diboride," *J. Eur. Ceram. Soc.*, vol. 35, no. 3, pp. 887–896, 2015.

[114] A. Khadimallah, X. Li, and K. W. White, "Solubility of tungsten in zirconium diboride solid solution," *J. Eur. Ceram. Soc.*, vol. 37, no. 4, pp. 1195–1203, 2017.

[115] F. Monteverde, A. Bellosi, and S. Guicciardi, "Processing and properties of zirconium diboride-based composites," *J. Eur. Ceram. Soc.*, vol. 22, no. 3, pp. 279–288, 2002.

[116] W. G. Fahrenholtz, G. E. Hilmas, S. C. Zhang, and S. Zhu, "Pressureless sintering of zirconium diboride: Particle size and additive effects," *J. Am. Ceram. Soc.*, vol. 91, no. 5, pp. 1398–1404, 2008.

[117] M. Mashhadi, H. Khaksari, and S. Safi, "Pressureless sintering behavior and mechanical properties of ZrB_2-SiC composites: Effect of SiC content and particle size," *J. Mater. Res. Technol.*, vol. 4, no. 4, pp. 416–422, 2015.

[118] F. Monteverde, "Beneficial effects of an ultra-fine α-SiC incorporation on the sinterability and mechanical properties of ZrB_2," *Appl. Phys. A Mater. Sci. Process.*, vol. 82, no. 2, pp. 329–337, 2006.

[119] H. L. Liu, J. X. Liu, H. T. Liu, and G. J. Zhang, "Contour maps of mechanical properties in ternary ZrB_2-SiC-ZrC ceramic system," *Scr. Mater.*, vol. 107, pp. 140–144, 2015.

[120] F. Monteverde and L. Silvestroni, "Combined effects of WC and SiC on densification and thermo-mechanical stability of ZrB_2 ceramics," *Mater. Des.*, vol. 109, pp. 396–407, 2016.

[121] L. Silvestroni, C. Capiani, D. Dalle Fabbriche, and C. Melandri, "Novel light and tough ZrB_2-based functionally graded ceramics," *Compos. Part B Eng.*, vol. 99, pp. 321–329, 2016.

[122] L. Silvestroni, D. Sciti, C. Melandri, and S. Guicciardi, "Toughened ZrB_2-based ceramics through SiC whisker or SiC chopped fiber additions," *J. Eur. Ceram. Soc.*, vol. 30, no. 11, pp. 2155–2164, 2010.

[123] L. Silvestroni, D. Sciti, G. E. Hilmas, W. G. Fahrenholtz, and J. Watts, "Effect of a weak fiber interface coating in ZrB_2 reinforced with long SiC fibers," *Mater. Des.*, vol. 88, pp. 610–618, 2015.

[124] D. Sciti, L. Silvestroni, G. Celotti, C. Melandri, and S. Guicciardi, "Sintering and Mechanical Properties of ZrB_2-$TaSi_2$ and HfB_2-$TaSi_2$ Ceramic Composites," *J. Am.*

Ceram. Soc., vol. 91, no. 10, pp. 3285–3291, 2008.

[125] D. Sciti, S. Guicciardi, A. Bellosi, and G. Pezzotti, "Properties of a pressureless-sintered ZrB_2-$MoSi_2$ ceramic composite," *J. Am. Ceram. Soc.*, vol. 89, no. 7, pp. 2320–2322, 2006.

[126] S. Guo, T. Nishimura, and Y. Kagawa, "Low-temperature hot pressing of ZrB_2-based ceramics with $ZrSi_2$ additives," *Int. J. Appl. Ceram. Technol.*, vol. 8, no. 6, pp. 1425–1435, 2011.

[127] S. Q. Guo, Y. Kagawa, T. Nishimura, and H. Tanaka, "Pressureless sintering and physical properties of ZrB_2-based composites with $ZrSi_2$ additive," *Scr. Mater.*, vol. 58, no. 7, pp. 579–582, 2008.

[128] D. Sciti, F. Monteverde, S. Guicciardi, G. Pezzotti, and A. Bellosi, "Microstructure and mechanical properties of ZrB_2-$MoSi_2$ ceramic composites produced by different sintering techniques," *Mater. Sci. Eng. A*, vol. 434, no. 1–2, pp. 303–309, 2006.

[129] L. Silvestroni, A. Vinci, S. Failla, L. Zoli, V. Rubio, J. Binner, D. Sciti, "Ablation behaviour of ultra-high temperature ceramic matrix composites: Role of $MeSi_2$ addition," *J. Eur. Ceram. Soc.*, vol. 39, no. 9, pp. 2771–2781, Aug. 2019.

[130] D. Sciti, M. Brach, and A. Bellosi, "Oxidation behavior of a pressureless sintered ZrB_2–$MoSi_2$ ceramic composite," *J. Mater. Res.*, vol. 20, no. 04, pp. 922–930, 2005.

[131] E. W. Neuman, G. E. Hilmas, and W. G. Fahrenholtz, "Strength of zirconium diboride to 2300°C," *J. Am. Ceram. Soc.*, vol. 96, no. 1, pp. 47–50, 2013.

[132] L. Silvestroni, D. Sciti, F. Monteverde, K. Stricker, and H. J. Kleebe, "Microstructure evolution of a W-doped ZrB_2 ceramic upon high-temperature oxidation," *J. Am. Ceram. Soc.*, vol. 100, no. 4, pp. 1760–1772, 2017.

[133] H. Kodama and T. Miyoshi, "Study of Fracture Behavior of Very Fine-Grained Silicon Carbide Ceramics," *J. Am. Ceram. Soc.*, vol. 73, no. 10, pp. 3081–3086, 1990.

[134] S. Maloy, A. H. Heuer, J. Lewandowski, and J. Petrovic, "Carbon Additions to Molybdenum Disilicide: Improved High-Temperature Mechanical Properties," *J. Am. Ceram. Soc.*, vol. 74, no. 10, pp. 2704–2706, 1991.

[135] A. L. Chamberlain, W. G. Fahrenholtz, G. E. Hilmas, and D. T. Ellerby, "Characterization of Zirconium Diboride–Molybdenum Disilicide Ceramic," in *Advances in Ceramic Matrix Composites IX*, N. P. Bansal, J. P. Singh, W. M. Kriven, and H. Schneider, Eds. Westerville, OH: American Ceramic Society, 2003, pp. 299–308.

[136] M. S. Asl, M. G. Kakroudi, and S. Noori, "Hardness and toughness of hot pressed ZrB_2-SiC composites consolidated under relatively low pressure," *J. Alloys Compd.*, vol. 619, pp. 481–487, 2015.

[137] Z. Chlup, L. Baca, M. Halasova, E. Neubauer, H. Hadraba, N. Stelzer, P. Roupcova, "Effect of metallic dopants on the microstructure and mechanical properties of TiB_2," *J. Eur. Ceram. Soc.*, vol. 35, no. 10, pp. 2745–2754, 2015.

[138] J. Marschall, A. Chamberlain, D. Crunkleton, and B. Rogers, "Catalytic Atom Recombination on ZrB_2/SiC and HfB_2/SiC Ultrahigh-Temperature Ceramic Composites," *J. Spacecr. Rockets*, vol. 41, no. 4, pp. 576–581, 2004.

[139] E. Wuchina, M. Opeka, S. Causey, K. Buesking, J. Spain, A. Cull, J. Routbort, F. Guitierrez-Mora, "Designing for ultrahigh-temperature applications: The mechanical and thermal properties of HfB_2, HfC_x, HfN_x and αHf(N)," *Journal of Materials Science*, vol. 39, no. 19. pp. 5939–5949, 2004.

[140] G.-J. Zhang, Z.-Y. Deng, N. Kondo, J.-F. Yang, and T. Ohji, "Reactive Hot Pressing of ZrB_2-SiC Composites," *J. Am. Ceram. Soc.*, vol. 83, no. 9, pp. 2330–2332, 2004.

[141] J. W. Zimmermann, G. E. Hilmas, W. G. Fahrenholtz, R. B. Dinwiddie, W. D. Porter, and H. Wang, "Thermophysical properties of ZrB_2 and ZrB_2-SiC ceramics," *J. Am. Ceram. Soc.*, vol. 91, no. 5, pp. 1405–1411, 2008.

[142] A. Rezaie, W. G. Fahrenholtz, and G. E. Hilmas, "Effect of hot pressing time and temperature on the microstructure and mechanical properties of ZrB_2-SiC," *J. Mater. Sci.*, vol. 42, no. 8, pp. 2735–2744, 2007.

[143] Y. Yan, Z. Huang, S. Dong, and D. Jiang, "Pressureless sintering of high-density ZrB_2-SiC ceramic composites," *J. Am. Ceram. Soc.*, vol. 89, no. 11, pp. 3589–3592, 2006.

[144] W. G. Fahrenholtz, G. E. Hilmas, A. L. Chamberlain, and J. W. Zimmermann, "Processing and characterization of ZrB_2-based ultra-high temperature monolithic and brous monolithic ceramics," *J. Mater. Sci.*, vol. 39, pp. 5951–5957, 2004.

[145] N. Akçamlı, D. Ağaoğulları, Ö. Balcı, M. L. Öveçoğlu, and İ. Duman, "Mechanical activation-assisted autoclave processing and sintering of HfB_2-HfO_2 ceramic powders," *Ceram. Int.*, vol. 42, no. 13, pp. 14642–14655, 2016.

[146] T. R. Paul, M. K. Mondal, and M. Mallik, "Microstructure dependent physical and mechanical properties of spark plasma sintered ZrB_2-$MoSi_2$–SiC_w composites," *Int. J. Refract. Met. Hard Mater.*, vol. 79, pp. 131–137, 2019.

[147] L. Silvestroni and D. Sciti, "Effects of $MoSi_2$ additions on the properties of Hf- and Zr-B_2 composites produced by pressureless sintering," *Scr. Mater.*, vol. 57, no. 2, pp. 165–168, 2007.

[148] W. M. Guo, J. Vleugels, G. J. Zhang, P. L. Wang, and O. Van der Biest, "Effects of Re_2O_3(Re = La, Nd, Y and Yb) addition in hot-pressed ZrB_2-SiC ceramics," *J. Eur. Ceram. Soc.*, vol. 29, no. 14, pp. 3063–3068, 2009.

[149] M. Mallik, P. Mitra, N. Srivastava, A. Narain, S. G. Dastidar, T. R. Paul, "Abrasive wear performance of zirconium diboride based ceramic composite," *Int. J. Refract. Met. Hard Mater.*, vol. 79, no. August 2018, pp. 224–232, 2019.

[150] H. L. Liu, G. J. Zhang, J. X. Liu, and H. Wu, "Synergetic roles of ZrC and SiC in ternary ZrB_2-SiC-ZrC ceramics," *J. Eur. Ceram. Soc.*, vol. 35, no. 16, pp. 4389–4397, 2015.

[151] L. Xu *et al.*, "Improved both mechanical and anti-oxidation performances of ZrB_2-SiC ceramics with molybdenum disilicide addition," *Mater. Chem. Phys.*, vol. 223, no. 72, pp. 53–59, 2019.

[152] S. Zhou, Z. Wang, X. Sun, and J. Han, "Microstructure, mechanical properties and thermal shock resistance of zirconium diboride containing silicon carbide ceramic toughened by carbon black," *Mater. Chem. Phys.*, vol. 122, no. 2–3, pp. 470–473, 2010.

[153] Y. An, X. Xu, and K. Gui, "Effect of SiC whiskers and graphene nanosheets on the mechanical properties of ZrB_2-SiC_w-Graphene ceramic composites," *Ceram. Int.*, vol. 42, no. 12, pp. 14066–14070, 2016.

[154] C. Wei, X. Zhang, and S. Li, "Laminated ZrB_2-SiC/graphite ceramics with simultaneously improved flexural strength and fracture toughness," *Ceram. Int.*, vol. 40, no. 3, pp. 5001–5006, 2014.

[155] M. Shahedi Asl and M. Ghassemi Kakroudi, "Characterization of hot-pressed graphene reinforced ZrB_2-SiC composite," *Mater. Sci. Eng. A*, vol. 625, pp. 385–392, 2015.

[156] W.-M. Guo, Y. You, G.-J. Zhang, S.-H. Wu, and H.-T. Lin, "Improvement of fracture toughness of ZrB_2-SiC composites with carbon interfaces," *J. Eur. Ceram. Soc.*, vol. 35, no. 6, pp. 1985–1989, 2015.

[157] W. Han, G. Li, X. Zhang, and J. Han, "Effect of AlN as sintering aid on hot-pressed ZrB_2-SiC ceramic composite," *J. Alloys Compd.*, vol. 471, no. 1–2, pp. 488–491, 2009.

[158] Y. Yang, Y. hai Qian, J. jun Xu, and M. shuan Li, "Effects of $TaSi_2$ addition on room temperature mechanical properties of ZrB_2-20SiC composites," *Ceram. Int.*, vol. 44, no. 14, pp. 16150–16156, 2018.

[159] J. J. Sha, Z. Q. Wei, J. Li, Z. F. Zhang, X. L. Yang, Y. C. Zhang, J. X. Dai , "Mechanical properties and toughening mechanism of WC-doped ZrB_2-$ZrSi_2$ ceramic composites by hot pressing," *Mater. Des.*, vol. 62, pp. 199–204, 2014.

[160] W. B. Tian, Y. M. Kan, G. J. Zhang, and P. L. Wang, "Effect of carbon nanotubes on the properties of ZrB_2-SiC ceramics," *Mater. Sci. Eng. A*, vol. 487, no. 1–2, pp. 568–573, 2008.

[161] M. Shahedi Asl, I. Farahbakhsh, and B. Nayebi, "Characteristics of multi-walled carbon nanotube toughened ZrB_2-SiC ceramic composite prepared by hot pressing," *Ceram.*

Int., vol. 42, no. 1, pp. 1950–1958, 2016.

[162] X. Zhang, R. Liu, X. Xiong, and Z. Chen, "Mechanical properties and ablation behavior of ZrB_2-SiC ceramics fabricated by spark plasma sintering," *Int. J. Refract. Met. Hard Mater.*, vol. 48, pp. 120–125, 2015.

[163] S. Chakraborty, D. Debnath, A. R. Mallick, R. K. Gupta, A. Ranjan, P. K. Das, D. Ghosh, "Microscopic, mechanical and thermal properties of spark plasma sintered ZrB_2 based composite containing polycarbosilane derived SiC," *Int. J. Refract. Met. Hard Mater.*, vol. 52, pp. 176–182, 2015.

[164] R. Stadelmann, M. Lugovy, N. Orlovskaya, P. Mchaffey, M. Radovic, V. M. Sglavo, S. Grasso, M. J. Reece, "Mechanical properties and residual stresses in ZrB_2–SiC spark plasma sintered ceramic composites," *J. Eur. Ceram. Soc.*, vol. 36, no. 7, pp. 1527–1537, 2016.

[165] J. Zou, G. J. Zhang, Z. J. Shen, and J. Binner, "Ultra-low temperature reactive spark plasma sintering of ZrB_2-hBN ceramics," *J. Eur. Ceram. Soc.*, vol. 36, no. 15, pp. 3637–3645, 2016.

[166] A. Bellosi, F. Monteverde, and D. Sciti, "Fast densification of ultra-high-temperature ceramics by spark plasma sintering," *Int. J. Appl. Ceram. Technol.*, vol. 3, no. 1, pp. 32–40, 2006.

[167] Y. Orooji, M. R. Derakhshandeh, E. Ghasali, M. Alizadeh, M. Shahedi Asl, and T. Ebadzadeh, "Effects of ZrB_2 reinforcement on microstructure and mechanical properties of a spark plasma sintered mullite-CNT composite," *Ceram. Int.*, vol. 45, no. 13, pp. 16015–16021, Sep. 2019.

[168] T. Venkateswaran, B. Basu, G. B. Raju, and D. Y. Kim, "Densification and properties of transition metal borides-based cermets via spark plasma sintering," *J. Eur. Ceram. Soc.*, vol. 26, no. 13, pp. 2431–2440, 2006.

[169] P. Vaziri and Z. Balak, "Improved mechanical properties of ZrB_2-30 vol% SiC using zirconium carbide additive," *Int. J. Refract. Met. Hard Mater.*, vol. 83, no. April, p. 104958, 2019.

[170] B. Nayebi, Z. Ahmadi, M. Shahedi Asl, S. Parvizi, and M. Shokouhimehr, "Influence of vanadium content on the characteristics of spark plasma sintered ZrB_2–SiC–V composites," *J. Alloys Compd.*, vol. 805, pp. 725–732, 2019.

[171] Z. Balak, "Shrinkage, hardness and fracture toughness of ternary ZrB_2–SiC-HfB_2 composite with different amount of HfB_2," *Mater. Chem. Phys.*, vol. 235, no. June, p. 121706, 2019.

[172] K. Kavakeb, Z. Balak, and H. Kafashan, "Densification and flexural strength of ZrB_2–

30 vol% SiC with different amount of HfB_2," *Int. J. Refract. Met. Hard Mater.*, vol. 83, no. May, p. 104971, 2019.

[173] H. Wang, C.-A. Wang, X. Yao, and D. Fang, "Processing and Mechanical Properties of Zirconium Diboride-Based Ceramics Prepared by Spark Plasma Sintering," *J. Am. Ceram. Soc.*, vol. 90, no. 7, pp. 1992–1997, 2007.

[174] D. Medveď, J. Balko, R. Sedlak, A. Kovalcikova, I. Shepa, A. Naughton-Duszova, E. Baczek, M. Podsiadlo, J. Dusza, "Wear resistance of ZrB_2 based ceramic composites," *Int. J. Refract. Met. Hard Mater.*, vol. 81, no. March, pp. 214–224, 2019.

[175] M. Shahedi Asl, B. Nayebi, Z. Ahmadi, S. Parvizi, and M. Shokouhimehr, "A novel ZrB_2–VB_2–ZrC composite fabricated by reactive spark plasma sintering," *Mater. Sci. Eng. A*, vol. 731, no. April, pp. 131–139, 2018.

[176] G. B. Yadhukulakrishnan, A. Rahman, S. Karumuri, M. M. Stackpoole, A. K. Kalkan, R. P. Singh, S. P. Harimkar, "Spark plasma sintering of silicon carbide and multi-walled carbon nanotube reinforced zirconium diboride ceramic composite," *Mater. Sci. Eng. A*, vol. 552, pp. 125–133, 2012.

[177] J. Lin, Y. Huang, H. Zhang, Y. Yang, and N. Li, "Microstructure and mechanical properties of spark plasma sintered ZrB_2–SiC–MWCNT composites," *Ceram. Int.*, vol. 41, pp. 15261–15265, 2015.

[178] S. Parvizi, Z. Ahmadi, M. J. Zamharir, and M. Shahedi Asl, "Synergistic effects of graphite nano-flakes and submicron SiC particles on the characteristics of spark plasma sintered ZrB_2 nanocomposites," *Int. J. Refract. Met. Hard Mater.*, vol. 75, no. March, pp. 10–17, 2018.

[179] F. Monteverde and R. Savino, "Stability of ultra-high-temperature ZrB_2-SiC ceramics under simulated atmospheric re-entry conditions," *J. Eur. Ceram. Soc.*, vol. 27, no. 16, pp. 4797–4805, 2007.

[180] J. W. Zimmermann, G. E. Hilmas, W. G. Fahrenholtz, F. Monteverde, and A. Bellosi, "Fabrication and properties of reactively hot pressed ZrB_2-SiC ceramics," *J. Eur. Ceram. Soc.*, vol. 27, no. 7, pp. 2729–2736, 2007.

[181] I. Akin and G. Goller, "Mechanical and oxidation behavior of spark plasma sintered ZrB_2-ZrC-SiC composites," *J. Ceram. Soc. Japan*, vol. 120, no. 1400, pp. 143–149, 2012.

[182] D. D. Jayaseelan, E. Zapata-Solvas, P. Brown, and W. E. Lee, "In situ formation of oxidation resistant refractory coatings on SiC-reinforced ZrB_2 ultra high temperature ceramics," *J. Am. Ceram. Soc.*, vol. 95, no. 4, pp. 1247–1254, 2012.

[183] C. Wei, S. Li, K. Yin, X. Liu, P. Wang, and L. Zhou, "Fracture behavior of laminated

ZrB_2–SiC ceramics at high temperature in air," *Ceram. Int.*, vol. 44, no. 4, pp. 4385–4391, 2018.

[184] T. A. Parthasarathy, R. A. Rapp, M. Opeka, and R. J. Kerans, "A model for the oxidation of ZrB_2, HfB_2 and TiB_2," *Acta Mater.*, vol. 55, no. 17, pp. 5999–6010, 2007.

[185] W. G. Fahrenholtz, "The ZrB_2 volatility diagram," *J. Am. Ceram. Soc.*, vol. 88, no. 12, pp. 3509–3512, 2005.

[186] J. B. Berkowitz-Mattuck, "High-Temperature Oxidation: III. Zirconium and Hafnium Diborides," *J. Electrochem. Soc.*, vol. 113, no. 9, pp. 908–914, 1966.

[187] T. A. Parthasarathy, R. A. Rapp, M. Opeka, and R. J. Kerans, "A model for transitions in oxidation regimes of ZrB_2," *Mater. Sci. Forum*, vol. 595-598 PA, pp. 823–832, 2008.

[188] J. K. Sonber, T. S. R. C. Murthy, C. Subramanian, S. Kumar, R. K. Fotedar, and A. K. Suri, "Investigations on synthesis of ZrB_2 and development of new composites with HfB_2 and $TiSi_2$," *Int. J. Refract. Met. Hard Mater.*, vol. 29, no. 1, pp. 21–30, 2011.

[189] T. S. R. C. Murthy, J. K. Sonber, B. Vishwanadh, A. Nagraj, K. Sairam, R. D. Bedse, J. K. Chakravartty , "Densification, characterization and oxidation studies of novel TiB_2+EuB_6 compounds," *J. Alloys Compd.*, vol. 670, pp. 85–95, 2016.

[190] F. Monteverde and A. Bellosi, "Oxidation of ZrB[sub2]-Based Ceramics in Dry Air," *J. Electrochem. Soc.*, vol. 150, no. 11, p. B552, 2003.

[191] T. A. Parthasarathy, R. A. Rapp, M. Opeka, and R. J. Kerans, "Effects of phase change and oxygen permeability in oxide scales on oxidation kinetics of ZrB_2 and HfB_2," *J. Am. Ceram. Soc.*, vol. 92, no. 5, pp. 1079–1086, 2009.

[192] P. Hu, W. Guolin, and Z. Wang, "Oxidation mechanism and resistance of ZrB_2-SiC composites," *Corros. Sci.*, vol. 51, no. 11, pp. 2724–2732, 2009.

[193] A. Rezaie, W. G. Fahrenholtz, and G. E. Hilmas, "The effect of a graphite addition on oxidation of ZrB_2–SiC in air at 1500°C," *J. Eur. Ceram. Soc.*, vol. 33, no. 2, pp. 413–421, 2013.

[194] E. Zapata-Solvas, D. D. Jayaseelan, H. T. Lin, P. Brown, and W. E. Lee, "Mechanical properties of ZrB_2- and HfB_2-based ultra-high temperature ceramics fabricated by spark plasma sintering," *J. Eur. Ceram. Soc.*, vol. 33, no. 7, pp. 1373–1386, 2013.

[195] J. He, Y. Wang, L. Luo, and L. An, "Oxidation behaviour of ZrB_2–SiC (Al/Y) ceramics at 1700 °C," *J. Eur. Ceram. Soc.*, vol. 36, no. 15, pp. 3769–3774, 2016.

[196] Y. Yang, M. Li, L. Xu, J. Xu, Y. Qian, J. Zuo, T. Li, "Oxidation behaviours of ZrB_2-SiC-$MoSi_2$ composites at 1800 °C in air with different pressures," *Corros. Sci.*, vol. 157, no. 72, pp. 87–97, Aug. 2019.

[197] X. Jin, P. Li, C. Hou, X. Wang, X. Fan, C. Lu, G. Xiao, X. Shu , "Oxidation behaviors

of ZrB_2 based ultra-high temperature ceramics under compressive stress," *Ceram. Int.*, vol. 45, no. 6, pp. 7278–7285, 2019.

[198] T. Zhu, W. Li, X. Zhang, P. Hu, C. Hong, and L. Weng, "Oxidation behavior of ZrB_2–SiC–ZrO_2 ceramic composites in the temperature range of 800-1200 °C," *Mater. Chem. Phys.*, vol. 116, pp. 593–598, 2009.

[199] L. Silvestroni, E. Landi, K. Bejtka, A. Chiodoni, and D. Sciti, "Oxidation behavior and kinetics of ZrB_2 containing SiC chopped fibers," *J. Eur. Ceram. Soc.*, vol. 35, no. 16, pp. 4377–4387, 2015.

[200] I. G. Talmy, J. A. Zaykoski, and M. M. Opeka, "High-temperature chemistry and oxidation of ZrB2 ceramics containing SiC, Si_3N_4, Ta_5Si_3, and $TaSi_2$," *J. Am. Ceram. Soc.*, vol. 91, no. 7, pp. 2250–2257, 2008.

[201] D. D. Jayaseelan, E. Zapata-Solvas, R. J. Chater, and W. E. Lee, "Structural and compositional analyses of oxidised layers of ZrB_2-based UHTCs," *J. Eur. Ceram. Soc.*, vol. 35, no. 15, pp. 4059–4071, 2015.

[202] Z. Wang, Z. Wu, and G. Shi, "The oxidation behaviors of a ZrB_2-SiC-ZrC ceramic," *Solid State Sci.*, vol. 13, pp. 534–538, 2011.

[203] F. Monteverde and L. Scatteia, "Resistance to thermal shock and to oxidation of metal diborides-SiC ceramics for aerospace application," *J. Am. Ceram. Soc.*, vol. 90, no. 4, pp. 1130–1138, 2007.

[204] S. Guo, "Oxidation and its effect on flexural strength of hot-pressed ZrB_2-SiC composites with VC additives," *J. Asian Ceram. Soc.*, vol. 00, no. 00, pp. 1–10, Nov. 2020.

[205] S. Guo, T. Mizuguchi, M. Ikegami, and Y. Kagawa, "Oxidation behavior of ZrB_2–$MoSi_2$–SiC composites in air at 1500 °C," *Ceram. Int.*, vol. 37, pp. 585–591, 2011.

[206] W. B. Han, P. Hu, X. H. Zhang, J. C. Han, and S. H. Meng, "High-temperature oxidation at 1900°C of ZrB_2-xSiC ultrahigh-temperature ceramic composites," *J. Am. Ceram. Soc.*, vol. 91, no. 10, pp. 3328–3334, 2008.

[207] F. Monteverde, "The thermal stability in air of hot-pressed diboride matrix composites for uses at ultra-high temperatures," *Corros. Sci.*, vol. 47, no. 8, pp. 2020–2033, 2005.

[208] R. Inoue, Y. Arai, and Y. Kubota, "Oxidation behaviors of ZrB_2–SiC binary composites above 2000°C," *Ceram. Int.*, vol. 43, no. 11, pp. 8081–8088, 2017.

[209] J. Han, P. Hu, X. Zhang, and S. Meng, "Oxidation behavior of zirconium diboride-silicon carbide at 1800°C," *Scr. Mater.*, vol. 57, no. 9, pp. 825–828, 2007.

[210] J. Han, P. Hu, X. Zhang, S. Meng, and W. Han, "Oxidation-resistant ZrB_2–SiC composites at 2200 °C," *Compos. Sci. Technol.*, vol. 68, pp. 799–806, 2008.

[211] D. Gao, Y. Zhang, J. Fu, C. Xu, Y. Song, and X. Shi, "Oxidation of zirconium diboride-silicon carbide ceramics under an oxygen partial pressure of 200Pa: Formation of zircon," *Corros. Sci.*, vol. 52, no. 10, pp. 3297–3303, 2010.

[212] Z. Kováčová, L. Bača, E. Neubauer, and M. Kitzmantel, "Influence of sintering temperature, SiC particle size and Y_2O_3 addition on the densification, microstructure and oxidation resistance of ZrB_2-SiC ceramics," *J. Eur. Ceram. Soc.*, vol. 36, no. 12, pp. 3041–3049, 2016.

[213] R. Inoue, Y. Arai, Y. Kubota, Y. Kogo, and K. Goto, "Initial oxidation behaviors of ZrB_2-SiC-ZrC ternary composites above 2000 °C," *J. Alloys Compd.*, vol. 731, pp. 310–317, 2018.

[214] H. Jin, S. Meng, X. Zhang, Q. Zeng, and J. Niu, "Effects of oxidation temperature, time, and ambient pressure on the oxidation of ZrB_2-SiC-graphite composites in atomic oxygen," *J. Eur. Ceram. Soc.*, vol. 36, no. 8, pp. 1855–1861, 2016.

[215] N. Liao, D. Jia, Z. Yang, and Y. Li, "Improved toughness of ZrB_2–SiC composites with nanopowders obtained by mechanical alloying," *J. Phys. Chem. Solids*, vol. 136, no. April 2019, p. 109153, 2020.

[216] S. K. Kashyap, A. Kumar, and R. Mitra, "Kinetics and evolution of oxide scale during various stages of isothermal oxidation at 1300 °C in spark plasma sintered ZrB_2– SiC–LaB_6 composites," *J. Eur. Ceram. Soc.*, vol. 40, no. 15, pp. 4997–5011, 2020.

[217] J. Zhao, H. T. Liu, J. X. Liu, and G. J. Zhang, "ZrB_2 ceramics doped with AlB_2," *Ceram. Int.*, vol. 40, no. 6, pp. 8915–8920, 2014.

[218] Z. Kováčová, L. Orovcik, J. Sedlacek, L. Baca, E. Dobrocka, M. Kitzmantel, E. Neubauer, "The effect of YB_4 addition in ZrB_2-SiC composites on the mechanical properties and oxidation performance tested up to 2000 °C," *J. Eur. Ceram. Soc.*, vol. 40, no. March, pp. 3829–3843, 2020.

[219] S. C. Zhang, G. E. Hilmas, and W. G. Fahrenholtz, "Improved Oxidation Resistance of Zirconium Diboride by Tungsten Carbide Additions," *J. Am. Ceram. Soc.*, vol. 91, no. 11, pp. 3530–3535, 2008.

[220] E. Zapata-Solvas, D. D. Jayaseelan, P. M. Brown, and W. E. Lee, "Effect of La_2O_3 addition on long-term oxidation kinetics of ZrB_2-SiC and HfB_2-SiC ultra-high temperature ceramics," *J. Eur. Ceram. Soc.*, vol. 34, no. 15, pp. 3535–3548, 2014.

[221] K. S. Cissel and E. J. Opila, "Oxygen Diffusion Mechanisms During High Temperature Oxidation of ZrB_2-SiC," *J. Am. Ceram. Soc.*, vol. 101, no. 4, pp. 1765–1779, 2018.

[222] J. Opila and M. C. Halbig, "Oxidation of ZrB_2-SiC," *Ceram. Eng. Sci. Proc.*, vol. 22, pp. 221–228, 2001.

[223] E. Opila, S. Levine, and J. Lorincz, “Oxidation of ZrB_2- and HfB_2-based ultra-high temperature ceramics: Effect of Ta additions,” *J. Mater. Sci.*, vol. 39, pp. 5969–5977, 2004.

[224] A. Rezaie, W. G. Fahrenholtz, and G. E. Hilmas, “Oxidation of zirconium diboride-silicon carbide at 1500°C at a low partial pressure of oxygen,” *J. Am. Ceram. Soc.*, vol. 89, no. 10, pp. 3240–3245, 2006.

[225] A. Rezaie, W. G. Fahrenholtz, and G. E. Hilmas, “Evolution of structure during the oxidation of zirconium diboride-silicon carbide in air up to 1500 °C,” *J. Eur. Ceram. Soc.*, vol. 27, no. 6, pp. 2495–2501, 2007.

[226] W. C. Tripp and H. C. Graham, “Thermogravimetric Study of the Oxidation of ZrB_2 in the Temperature Range of 800 to 1500 °C,” *J. Electrochem. Soc.*, vol. 118, pp. 1195–1199, 1968.

[227] R. Hassan, R. Kundu, and K. Balani, “Oxidation behaviour of coarse and fine SiC reinforced ZrB_2 at re-entry and atmospheric oxygen pressures,” *Ceram. Int.*, vol. 46, no. 8, pp. 11056–11065, 2020.

[228] D. Gao, Y. Zhang, C. Xu, Y. Song, and X. Shi, “Oxidation kinetics of hot-pressed ZrB_2-SiC ceramic matrix composites,” *Ceram. Int.*, vol. 39, no. 3, pp. 3113–3119, 2013.

[229] E. Eakins, D. D. Jayaseelan, and W. E. Lee, “Toward oxidation-resistant ZrB_2-SiC ultra high temperature ceramics,” *Metall. Mater. Trans. A Phys. Metall. Mater. Sci.*, vol. 42, no. 4, pp. 878–887, 2011.

[230] S. R. Levine, E. J. Opila, M. C. Halbig, J. D. Kiser, M. Singh, and J. A. Salem, “Evaluation of ultra-high temperature ceramics for aeropropulsion use,” *J. Eur. Ceram. Soc.*, vol. 22, no. 14–15, pp. 2757–2767, 2002.

[231] K. Shugart and E. Opila, “SiC Depletion in ZrB_2–30 vol% SiC at Ultrahigh Temperatures,” *J. Am. Ceram. Soc.*, vol. 98, no. 5, pp. 1673–1683, 2015.

[232] A. Momozawa, R. Tu, T. Goto, Y. Kubota, H. Hatta, and K. Komurasaki, “Quantitative evaluation of the oxidation behavior of ZrB_2-15vol.% SiC at a low oxygen partial pressure,” *Vacuum*, vol. 88, no. 1, pp. 98–102, 2013.

[233] H. Jin, S. Meng, X. Zhang, Q. Zeng, and J. Niu, “Effects of oxygen partial pressure on the oxidation of ZrB_2-SiC-graphite composites at 1800 °C,” *Ceram. Int.*, vol. 42, no. 5, pp. 6480–6486, 2016.

[234] H. Jin, S. Meng, Z. Xinghong, Z. Qingxuan, and X. Weihua, “Oxidation of ZrB_2–SiC-Graphite Composites Under Low Oxygen Partial Pressures of 500 and 1500 Pa at 1800°C,” *J. Am. Ceram. Soc.*, vol. 99, no. 7, pp. 2474–2480, 2016.

[235] M. Gasch, D. Ellerby, E. Irby, S. Beckman, M. Gusman, and S. Johnson, “Processing,

properties and arc jet oxidation of hafnium diboride/silicon carbide ultra high temperature ceramics," *J. Mater. Sci.*, vol. 39, no. 19, pp. 5925–5937, 2004.

[236] W. G. Fahrenholtz and G. E. Hilmas, "Oxidation of ultra-high temperature transition metal diboride ceramics," *Int. Mater. Rev.*, vol. 57, no. 1, pp. 61–72, 2012.

[237] W. G. Fahrenholtz, "Thermodynamic analysis of ZrB_2-SiC oxidation: Formation of a SiC-depleted region," *J. Am. Ceram. Soc.*, vol. 90, no. 1, pp. 143–148, 2007.

[238] I. G. Talmy, J. A. Zaykoski, and C. A. Martin, "Flexural creep deformation of ZrB_2/SiC ceramics in oxidizing atmosphere," *J. Am. Ceram. Soc.*, vol. 91, no. 5, pp. 1441–1447, 2008.

[239] I. Spivak, R. Andrievskii, V. Klimenko, and V. Lazarenko, "Creep in the binary systems TiB_2–TiC and ZrB_2–ZrN," *Powder Metall. Met. Ceram.*, vol. 13, no. 8, pp. 617–620, 1974.

[240] L. Silvestroni, G. Meriggi, and D. Sciti, "Oxidation behavior of ZrB_2 composites doped with various transition metal silicides," *Corros. Sci.*, vol. 83, pp. 281–291, 2014.

[241] D. Sciti, M. Brach, and A. Bellosi, "Long-term oxidation behavior and mechanical strength degradation of a pressurelessly sintered ZrB_2-$MoSi_2$ ceramic," *Scr. Mater.*, vol. 53, no. 11, pp. 1297–1302, 2005.

[242] D. Sciti, A. Balbo, and A. Bellosi, "Oxidation behaviour of a pressureless sintered HfB_2-$MoSi_2$ composite," *J. Eur. Ceram. Soc.*, vol. 29, no. 9, pp. 1809–1815, 2009.

[243] S. Q. Guo, T. Mizuguchi, T. Aoyagi, T. Kimura, and Y. Kagawa, "Quantitative electron microprobe characterizations of oxidized ZrB_2 containing $MoSi_2$ additives," *Oxid. Met.*, vol. 72, no. 5–6, pp. 335–345, 2009.

[244] L. Silvestroni, K. Stricker, D. Sciti, and H. J. Kleebe, "Understanding the oxidation behavior of a ZrB_2–$MoSi_2$ composite at ultra-high temperatures," *Acta Mater.*, vol. 151, pp. 216–228, 2018.

[245] L. Silvestroni, S. Failla, I. Neshpor, and O. Grigoriev, "Method to improve the oxidation resistance of ZrB_2-based ceramics for reusable space systems," *J. Eur. Ceram. Soc.*, vol. 38, no. 6, pp. 2467–2476, 2018.

[246] J. Zou, G. -J. Zhang, C. -F. Hu, T. Nishimura, Y. Sakka, J. Vleugels, O. V. Biest , "Strong ZrB_2-SiC-WC ceramics at 1600°C," *J. Am. Ceram. Soc.*, vol. 95, no. 3, pp. 874–878, 2012.

[247] M. K. Dehdashti, W. G. Fahrenholtz, and G. E. Hilmas, "Effects of temperature and the incorporation of W on the oxidation of ZrB_2 ceramics," *Corros. Sci.*, vol. 80, pp. 221–228, 2014.

[248] Z. Wang, Y. Niu, C. Hu, H. Li, Y. Zeng, X. Zheng, M. Ren, J. Sun, "High temperature

oxidation resistance of metal silicide incorporated ZrB_2 composite coatings prepared by vacuum plasma spray," *Ceram. Int.*, vol. 41, no. 10, pp. 14868–14875, 2015.

[249] F. Peng, Y. Berta, and R. F. Speyer, "Effect of SiC, TaB_2 and $TaSi_2$ additives on the isothermal oxidation resistance of fully dense zirconium diboride," *J. Mater. Res.*, vol. 24, no. 5, pp. 1855–1867, 2009.

[250] F. Peng and R. F. Speyer, "Oxidation resistance of fully dense ZrB_2 with SiC, TaB_2, and $TaSi_2$ additives," *J. Am. Ceram. Soc.*, vol. 91, no. 5, pp. 1489–1494, 2008.

[251] L. Silvestroni and H. J. Kleebe, "Critical oxidation behavior of Ta-containing ZrB_2 composites in the 1500–1650 °C temperature range," *J. Eur. Ceram. Soc.*, vol. 37, no. 5, pp. 1899–1908, 2017.

[252] W. M. Guo and G. J. Zhang, "Oxidation resistance and strength retention of ZrB_2-SiC ceramics," *J. Eur. Ceram. Soc.*, vol. 30, no. 11, pp. 2387–2395, 2010.

[253] S. N. Karlsdottir and J. W. Halloran, "Rapid oxidation characterization of ultra-high temperature ceramics," *J. Am. Ceram. Soc.*, vol. 90, no. 10, pp. 3233–3238, 2007.

[254] Y. H. Seong and D. K. Kim, "Oxidation behavior of ZrB_2-xSiC composites at 1500°C under different oxygen partial pressures," *Ceram. Int.*, vol. 40, no. 9 PART B, pp. 15303–15311, 2014.

[255] V. Guérineau and A. Julian-Jankowiak, "Oxidation mechanisms under water vapour conditions of ZrB_2-SiC and HfB_2-SiC based materials up to 2400 °C," *J. Eur. Ceram. Soc.*, vol. 38, no. 2, pp. 421–432, 2018.

[256] M. Patel, J. J. Reddy, V. V. Bhanu Prasad, and V. Jayaram, "Strength of hot pressed ZrB_2-SiC composite after exposure to high temperatures (1000-1700°C)," *J. Eur. Ceram. Soc.*, vol. 32, no. 16, pp. 4455–4467, 2012.

[257] E. J. Opila, J. Smith, S. R. Levine, J. Lorincz, and M. Reigel, "Oxidation of $TaSi_2$-Containing ZrB_2-SiC Ultra-High Temperature Materials," *Open Aerosp. Eng. J.*, vol. 3, pp. 41–51, 2010.

[258] M. Kazemzadeh Dehdashti, W. G. Fahrenholtz, and G. E. Hilmas, "Oxidation of zirconium diboride with niobium additions," *J. Eur. Ceram. Soc.*, vol. 33, no. 10, pp. 1591–1598, 2013.

[259] W. Fischer, "Extended Potentials of UHTCMCs in Space Vehicle Extreme Environment Applications-Large System Intergrator View and Expectations," in *ULTRA-HIGH TEMPERATURE CERAMICS: MATERIALS FOR EXTREME ENVIRONMENT APPLICATIONS IV*, 2017.

[260] G. Saccone, R. Gardi, D. Alfano, A. Ferrigno, and A. Del Vecchio, "Laboratory, on-ground and in-flight investigation of ultra high temperature ceramic composite

materials," *Aerosp. Sci. Technol.*, vol. 58, pp. 490–497, 2016.

[261] L. Mercatelli, E. Sani, D. Jafrancesco, P. Sansoni, D. Fontani, M. Meucci, S. Coraggia, L. Marconi, J. -L. Sans, E. Beche, L. Silvestroni, D. Sciti, "Ultra-refractory diboride ceramics for solar plant receivers," in *Energy Procedia*, 2013, vol. 49, pp. 468–477.

[262] E. Sani, L. Mercatelli, J. L. Sans, L. Silvestroni, and D. Sciti, "Porous and dense hafnium and zirconium ultra-high temperature ceramics for solar receivers," *Opt. Mater. (Amst).*, vol. 36, no. 2, pp. 163–168, 2013.

[263] M. M. Nasseri, "Comparison of HfB_2 and ZrB_2 behaviors for using in nuclear industry," *Ann. Nucl. Energy*, vol. 114, pp. 603–606, 2018.

[264] F. Qi, S. Meng, and H. Guo, "Repeated thermal shock behavior of the ZrB_2-SiC-ZrC ultrahigh-temperature ceramic," *Mater. Des.*, vol. 35, pp. 133–137, 2012.

[265] D. D. Jayaseelan, Y. Xin, L. Vandeperre, P. Brown, and W. E. Lee, "Development of multi-layered thermal protection system (TPS) for aerospace applications," *Compos. Part B Eng.*, vol. 79, pp. 392–405, 2015.

[266] K. Wei, R. He, X. Cheng, R. Zhang, Y. Pei, and D. Fang, "A lightweight, high compression strength ultra high temperature ceramic corrugated panel with potential for thermal protection system applications," *Mater. Des.*, vol. 66, no. PB, pp. 552–556, 2015.

[267] P. Kolodziej, J. V Bowles, and C. Roberts, "Optimizing hypersonic sharp body concepts from a thermal protection system perspective," *Am. Inst. Aeronaut. Astronaut. Inc.*, pp. 556–571, 1998.

[268] D. Wang, Y. Zeng, X. Xiong, G. Li, Z. Chen, W. Sun, Y. Wang, "Ablation behavior of ZrB_2-SiC protective coating for carbon/carbon composites," *Ceram. Int.*, vol. 41, no. 6, pp. 7677–7686, 2015.

[269] W. Peng, Y. He, X. Wang, J. Zhu, and J. Han, "Thermal protection mechanism of heat pipe in leading edge under hypersonic conditions," *Chinese J. Aeronaut.*, vol. 28, no. 1, pp. 121–132, 2015.

[270] D. Sciti, R. Savino, and L. Silvestroni, "Aerothermal behaviour of a SiC fibre-reinforced ZrB_2 sharp component in supersonic regime," *J. Eur. Ceram. Soc.*, vol. 32, no. 8, pp. 1837–1845, 2012.

[271] F. Wang, L. Cheng, Y. Xie, J. Jian, and L. Zhang, "Effects of SiC shape and oxidation on the infrared emissivity properties of ZrB_2-SiC ceramics," *J. Alloys Compd.*, vol. 625, pp. 1–7, 2015.

[272] R. Savino, M. De Stefano Fumo, D. Paterna, and M. Serpico, "Aerothermodynamic study of UHTC-based thermal protection systems," *Aerosp. Sci. Technol.*, vol. 9, no. 2,

pp. 151–160, 2005.

[273] D. A. Kontinos, K. Gee, and D. K. Prabhu, “Temperature Constraints at the Sharp Leading Edge of a Crew Transfer Vehicle,” in *American Institute of Aeronautics & Astronautics*, 2001, no. June.

[274] F. Monteverde, R. Savino, M. D. S. Fumo, and A. Di Maso, “Plasma wind tunnel testing of ultra-high temperature ZrB_2-SiC composites under hypersonic re-entry conditions,” *J. Eur. Ceram. Soc.*, vol. 30, no. 11, pp. 2313–2321, 2010.

[275] L. Silvestroni, D. Sciti, L. Zoli, A. Balbo, F. Zanotto, R. Orru, R. Licheri, C. Musa, L. Mercatelli, E. Sani, “An overview of ultra-refractory ceramics for thermodynamic solar energy generation at high temperature,” *Renew. Energy*, vol. 133, pp. 1257–1267, Apr. 2019.

[276] E. Sani, M. Meucci, L. Mercatelli, A. Balbo, C. Musa, R. Licheri, R. Orru, G. Cao, “Titanium diboride ceramics for solar thermal absorbers,” *Sol. Energy Mater. Sol. Cells*, vol. 169, no. March, pp. 313–319, 2017.

[277] X.-H. Gao, X.-L. Qiu, X.-T. Li, W. Theiss, B.-H. Chen, H.-X. Guo, T.-H. Zhou, G. Liu, “Structure, thermal stability and optical simulation of ZrB_2 based spectrally selective solar absorber coatings,” *Sol. Energy Mater. Sol. Cells*, vol. 193, no. April 2018, pp. 178–183, 2019.

[278] A. K. Suri, C. Subramanian, J. K. Sonber, and T. S. R. C. Murthy, *Synthesis and consolidation of boron carbide: a review*, vol. 55, no. 1. 2010.

[279] W. C. Oliver and G. M. Pharr, “An improved technique for determining hardness and elastic modulus using load and displacement sensing indentation experiments,” *J. Mater. Res.*, vol. 7, no. 6, pp. 1564–1583, Jun. 1992.

[280] B. R. Golla, J. W. Ko, and H. D. Kim, “Processing and characterization of sintered reaction bonded Si_3N_4 ceramics,” *Int. J. Refract. Met. Hard Mater.*, vol. 68, no. July, pp. 75–83, 2017.

[281] A. Bellosi and F. Monteverde, “Ultra-Refractory Ceramics: The Use of Sintering Aids to Obtain Microstructure Control and Properties Improvement,” *Key Eng. Mater.*, vol. 264–268, pp. 787–792, 2004.

[282] Z. Hamidzadeh Mahaseni, M. Dashti Germi, Z. Ahmadi, and M. Shahedi Asl, “Microstructural investigation of spark plasma sintered TiB_2 ceramics with Si_3N_4 addition,” *Ceram. Int.*, vol. 44, no. 11, pp. 13367–13372, 2018.

[283] J.-H. Park, Y.-H. Koh, H.-E. Kim, C. S. Hwang, and E. S. Kang, “Densification and Mechanical Properties of Titanium Diboride with Silicon Nitride as a Sintering Aid,” *J. Am. Ceram. Soc.*, vol. 82, no. 11, pp. 3037–3042, 1999.

[284] M. D. Germi, Z. H. Mahaseni, Z. Ahmadi, and M. S. Asl, “Phase evolution during spark plasma sintering of novel Si_3N_4-doped TiB_2–SiC composite,” *Mater. Charact.*, vol. 145, pp. 225–232, 2018.

[285] J. Marschall *et al.*, “Oxidation of ZrB_2-SiC Ultrahigh-Temperature Ceramic Composites in Dissociated Air,” *J. Thermophys. Heat Transf.*, vol. 23, no. 2, pp. 267–278, 2009.

[286] Z. Wang, P. Zhou, and Z. Wu, “Effect of surface oxidation on thermal shock resistance of ZrB_2-SiC-ZrC ceramic at temperature difference from 800 to 1900 °C,” *Corros. Sci.*, vol. 98, pp. 233–239, 2015.

[287] L. Zhang and N. P. Padture, “Inhomogeneous oxidation of ZrB_2-SiC ultra-high-temperature ceramic particulate composites and its mitigation,” *Acta Mater.*, vol. 129, pp. 138–148, 2017.

[288] X. Liu, C. Wei, W. Ji, S. Li, P. Wang, and L. Zhou, “Oxidation behaviour of laminated BN/ZrB_2–SiC ceramics,” *Ceram. Int.*, vol. 44, no. 7, pp. 8374–8379, 2018.

[289] P. Hu, X. H. Zhang, J. C. Han, X. G. Luo, and S. Y. Du, “Effect of various additives on the oxidation behavior of ZrB_2-based ultra-high-temperature ceramics at 1800°C,” *J. Am. Ceram. Soc.*, vol. 93, no. 2, pp. 345–349, 2010.

[290] H. T. Liu, J. Zou, D. W. Ni, W. W. Wu, Y. M. Kan, and G. J. Zhang, “Textured and platelet-reinforced ZrB_2-based ultra-high- temperature ceramics,” *Scr. Mater.*, vol. 65, no. 1, pp. 37–40, 2011.

[291] H. T. Liu, J. Zou, D. W. Ni, J. X. Liu, and G. J. Zhang, “Anisotropy oxidation of textured ZrB_2-$MoSi_2$ ceramics,” *J. Eur. Ceram. Soc.*, vol. 32, no. 12, pp. 3469–3476, 2012.

[292] H. L. Liu, J. X. Liu, H. T. Liu, and G. J. Zhang, “Changed oxidation behavior of ZrB_2-SiC ceramics with the addition of ZrC,” *Ceram. Int.*, vol. 41, no. 6, pp. 8247–8251, 2015.

[293] Y. Zhang, D. Gao, C. Xu, Y. Song, and X. Shi, “Oxidation behavior of hot pressed ZrB_2-ZrC-SiC ceramic composites,” *Int. J. Appl. Ceram. Technol.*, vol. 11, no. 1, pp. 178–185, 2014.

[294] C. Hu, Y. Sakka, H. Tanaka, T. Nishimura, S. Guo, and S. Grasso, “Microstructure and properties of ZrB_2-SiC composites prepared by spark plasma sintering using $TaSi_2$ as sintering additive,” *J. Eur. Ceram. Soc.*, vol. 30, no. 12, pp. 2625–2631, 2010.

[295] F. Monteverde, “The addition of SiC particles into a $MoSi_2$-doped ZrB_2 matrix: Effects on densification, microstructure and thermo-physical properties,” *Mater. Chem. Phys.*, vol. 113, no. 2–3, pp. 626–633, 2009.

[296] D. L. McClane, W. G. Fahrenholtz, and G. E. Hilmas, “Thermal properties of (Zr,TM)B_2 solid solutions with TM = Hf, Nb, W, Ti, and y,” *J. Am. Ceram. Soc.*, vol. 97, no. 5, pp. 1552–1558, 2014.

[297] A. N. Dorner, K. Werbach, G. E. Hilmas, and W. G. Fahrenholtz, “Effect of Tantalum Solid Solution Additions on the Mechanical Behavior of ZrB_2,” *J. Eur. Ceram. Soc.*, no. December 2020, 2020.

[298] X. Yan, X. Jin, P. Li, C. Hou, X. Hao, Z. Li, X. Fan, “Microstructures and mechanical properties of ZrB_2–SiC–Ni ceramic composites prepared by spark plasma sintering,” *Ceram. Int.*, vol. 45, no. 13, pp. 16707–16712, 2019.

[299] N. S. Karthiselva, B. S. Murty, and S. R. Bakshi, “Low temperature synthesis of dense and ultrafine grained zirconium diboride compacts by reactive spark plasma sintering,” *Scr. Mater.*, vol. 110, pp. 78–81, 2016.

[300] Z. Zhang, S. Fu, F. Aversano, M. Bortolotti, H. Zhang, C. Hu, S. Grasso, “Arc melting: a novel method to prepare homogeneous solid solutions of transition metal carbides (Zr, Ta, Hf),” *Ceram. Int.*, vol. 45, no. 7, pp. 9316–9319, 2019.

[301] M. Shahedi Asl, B. Nayebi, A. Motallebzadeh, and M. Shokouhimehr, “Nanoindentation and nanostructural characterization of ZrB_2–SiC composite doped with graphite nano-flakes,” *Compos. Part B Eng.*, vol. 175, no. May, p. 107153, 2019.

[302] I. G. Talmy, J. A. Zaykoski, M. M. Opeka, and A. H. Smith, “Properties of ceramics in the system ZrB_2-Ta_5Si_3,” *J. Mater. Res.*, vol. 21, no. 10, pp. 2593–2599, 2006.

[303] L. Silvestroni, D. Sciti, M. Balat-Pichelin, and L. Charpentier, “Zirconium carbide doped with tantalum silicide: Microstructure, mechanical properties and high temperature oxidation,” *Mater. Chem. Phys.*, vol. 143, no. 1, pp. 407–415, 2013.

[304] L. Charpentier, M. Balat-Pichelin, D. Sciti, and L. Silvestroni, “High temperature oxidation of Zr- and Hf-carbides: Influence of matrix and sintering additive,” *J. Eur. Ceram. Soc.*, vol. 33, no. 15–16, pp. 2867–2878, 2013.

[305] S. R. Levine and E. J. Opila, “Tantalum addition to zirconium diboride for improved oxidation resistance,” *Nasa/Tm-2003-212483*, no. July, pp. 1–13, 2003.

[306] X. Feng, X. Wang, Y. Liu, W. Tian, M. Zhang, X. Jian, L. Yin, L. Zhang, J. Xie, L. Deng, “Pursuing enhanced oxidation resistance of ZrB_2 ceramics by SiC and WC co-doping,” *J. Eur. Ceram. Soc.*, vol. 38, no. 16, pp. 5311–5318, 2018.

[307] H. Bin Ma, J. Zou, J. T. Zhu, L. F. Liu, and G. J. Zhang, “Segregation of tungsten atoms at ZrB_2 grain boundaries in strong ZrB_2-SiC-WC ceramics,” *Scr. Mater.*, vol. 157, pp. 76–80, 2018.

[308] X. hong Zhang, P. Hu, J. cai Han, L. Xu, and S. he Meng, “The addition of lanthanum hexaboride to zirconium diboride for improved oxidation resistance,” *Scr. Mater.*, vol. 57, no. 11, pp. 1036–1039, 2007.

[309] M. Kazemzadeh Dehdashti, W. G. Fahrenholtz, and G. E. Hilmas, “Effects of transition

metals on the oxidation behavior of ZrB_2 ceramics," *Corros. Sci.*, vol. 91, pp. 224–231, 2015.

List of publications

1. **Sravan Kumar Thimmappa**, Brahma Raju Golla, VV Bhanu Prasad, Bhaskar Majumdar, Bikramjit Basu, Phase stability, hardness and oxidation behaviour of spark plasma sintered ZrB_2-SiC-Si_3N_4 composites, Ceramic International Int. 45 (2019) 9061-9073.
2. **Sravan Kumar Thimmappa**, Brahma Raju Golla, Effect of tantalum addition on microstructure and oxidation of spark plasma sintered ZrB_2-20vol% SiC composites, Ceramic International 45 (2019) 13799-13808.
3. Brahma Raju Golla, **Sravan Kumar Thimmappa**, Comparative study on microstructure and oxidation behaviour of ZrB_2-20vol% SiC ceramic reinforced with Si_3N_4/Ta additives, Journal of Alloys and Compounds 797 (2019) 92-100.
4. Brahma Raju Golla, Amartya Mukhopadhyay, Bikramjit Basu and **Sravan Kumar Thimmappa**, Review on Ultra High Temperature Boride Ceramics, Progress in Materials Science 111 (2020) 100651.
5. **Sravan Kumar Thimmappa**, Brahma Raju Golla, Suresh Babu Pitchuka, Bhanu Prasad VV, Nanoindentation and high temperature oxidation behavior of ZrB_2-20SiC-(0-10wt.%) Ta UHTCs, Ceramic International (in Press, 2021).

Research publications outside the thesis work (research collaborations)

1. Sivakumar S, **Sravan Kumar Thimmappa**, Brahma Raju Golla, Corrosion behavior of extremely hard Al-Cu/Mg-SiC light metal alloy composites, Journal of Alloys and Compounds 767 (2018) 703-711.

Conferences participated

1. **Sravan Kumar Thimmappa**, Brahma Raju Golla, Bhanu Prasad VV, Highly oxidation resistant ZrB_2-20SiC-2.5Si_3N_4 composites processed via multi-stage spark plasma sintering, The International Conference on Advances in Minerals, Metals, Materials, Manufacturing and Modelling (ICAM[5]). National Institute of Technology, Warangal, 25-27 Sep 2019 (Oral presentation).
2. **Sravan Kumar Thimmappa**, Brahma Raju Golla, Bhanu Prasad VV, Microstructure and high temperature oxidation behavior of ZrB_2-20vol.% SiC with Si_3N_4 and Tantalum additives, International Symposium on Advanced Materials for Industrial and Societal Applications (NMD-ATM), IIM Trivandrum, 13-16 Nov 2019 (Poster presentation).